Recovery and recrystallization of nanostructured metals – mechanisms and kinetics

Yu, Tianbo

Publication date:
2011

Document Version
Publisher's PDF, also known as Version of record

Recovery and recrystallization of nanostructured metals – mechanisms and kinetics

Risø-PhD-Report

Tianbo Yu
Risø-PhD-79(EN)
July 2011

Risø DTU
National Laboratory for Sustainable Energy

Author: Tianbo Yu
Title: Recovery and recrystallization of nanostructured metals – mechanisms and kinetics
Division: Materials Research Division

This thesis is submitted in partial fulfilment of the requirements for the Ph.D. degree at the Technical University of Denmark.

Abstract:

The objective of this study is to explore and analyze the effect of heat treatments on the structure and properties of nanostructured metals processed by plastic deformation to high strains. Commercial purity aluminium was plastically deformed either by cold rolling or by accumulative roll bonding (ARB) and then annealed at various temperatures. A number of techniques, including Vickers hardness tests, electron backscattered diffraction (EBSD), transmission electron microscopy (TEM), and positron annihilation lifetime spectroscopy (PALS), were used to characterize the structural changes on different length scales to identify possible recovery mechanisms.

In this study, triple junctions in a deformed lamellar nanostructure are classified into three categories (Y-junctions, H-junctions, and r-junctions) based on the structural morphology, and a series of relationships is formulated between the density of triple junctions and the boundary spacing. Based on TEM and EBSD observations, thermally-activated Y-junction motion is identified as the key process during recovery of highly-strained aluminium, leading to removal of thin lamellae and coarsening of microstructure. A mechanism for recovery by Y-junction motion is proposed, which can underpin the general observation that a lamellar structure formed by plastic deformation coarsens into a more equiaxed structure during recovery annealing.

Y-junction motion operates in a wide temperature range, even at room temperature, in highly-strained aluminium. However, during annealing below 100°C, Y-junction motion is limited. At such low temperatures, annihilation of zigzagged dislocations is found to be the dominating recovery mechanism whereas other mechanisms, such as subgrain coalescence and boundary migration, are of minor importance.

A model is proposed to analyze the recovery kinetics based on hardness measurements, a model which allows the activation energy of recovery to be estimated. During annealing of highly-strained commercial purity aluminium at 140°C and above, the apparent activation energy is found to increase as recovery proceeds and approach ~190 kJ/mol at the end of recovery, pointing at this stage to an effect of solute drag during recovery as in recrystallization.

Risø-PhD-79(EN)
July 2011

ISSN 0106-2840
ISBN 978-87-550-3922-3

Group's own reg. no.:
1605075-00

Sponsorship:
Danish National Research Foundation

Supervisors:
Xiaoxu Huang
Grethe Winther

Pages: 139
References: 117

Information Service Department
Risø National Laboratory for Sustainable Energy
Technical University of Denmark
P.O.Box 49
DK-4000 Roskilde
Denmark
Telephone +45 46774005
bibl@risoe.dtu.dk
Fax +45 46774013
www.risoe.dtu.dk

Recovery and recrystallization of nanostructured metals – mechanisms and kinetics

Tianbo Yu

Supervised by Xiaoxu Huang and Grethe Winther

Materials Research Division

Risø National Laboratory for Sustainable Energy

Technical University of Denmark

July 2011

Contents

Preface

This thesis is submitted in partial fulfilment of the requirements for the PhD degree at the Technical University of Denmark. The project was carried out within the Centre for Fundamental Research: Metal Structures in Four Dimensions (M4D), Materials Research Division, Risø DTU, under the supervision of senior scientists, Drs. Xiaoxu Huang and Grethe Winther. The study was conducted during the period from August 2008 to July 2011.

I am grateful to Head of Division Dorte Juul Jensen and Head of Centre Henning Friis Poulsen, who gave me the opportunity to work within the M4D centre. I am thankful to my supervisors Xiaoxu Huang and Grethe Winther, who have provided me with constant support and many useful discussions. I am deeply indebted to Dr. Niels Hansen, who is instructing, enlightening, and encouraging me all the time. I would like to thank Professors Brian Ralph, Roy Vandermeer, Johannes Weertman, Julia Weertman, and Andrew Godfrey for their help and discussions. I would also like to thank senior scientists, Drs. Wolfgang Pantleon, Oleg Mishin, Morten Eldrup, Drs. Yili Wei, Yubin Zhang, and many other people in the Materials Research Division who have helped me. Special thanks to the very skilful technicians, Gitte Christiansen, Preben Olesen, Lars Lorentzen and Steen Bang.

Finally, I would like to thank my wife, Shuangyang Chu, for supporting me throughout the years.

Publications

Paper I Yu, T., Hansen, N., Huang, X. and Winther, G. 2009 Recovery kinetics of commercial purity aluminium after large strain. In *30th Risø International Symposium on Material Science* (eds J. Grivel *et al.*), pp. 393–400. Roskilde, Denmark: Risø National Laboratory.

Paper II Yu, T. and Hansen, N. 2010 A model for recovery kinetics of aluminium after large strain. In *Proceedings of the 4th international conference on recrystallization and grain growth*, Sheffield, UK (in press).

Paper III Godfrey, A., Mishin O.V. and Yu, T. 2010 EBSD-based techniques for characterization of microstructural restoration processes during annealing of metals deformed to large plastic strains. In *Proceedings of the 4th international conference on recrystallization and grain growth*, Sheffield, UK (in press).

Paper IV Yu, T., Hansen, N. and Huang, X. 2011 Recovery by triple junction motion in aluminium deformed to ultrahigh strains. *Proceedings of the Royal Society A: Mathematical, Physical and Engineering Sciences*. **467**, 3039-3065.

Paper V Yu, T. *et al.* 2011 Thermally-activated low-temperature recovery in nanostructured aluminium (in preparation).

Paper VI Yu, T. *et al.* 2011 Recovery kinetics of commercial purity aluminium deformed to ultrahigh strains (in preparation).

Chapter 1

Introduction

Metals are irreplaceable in the modern civilization (Lu 2010). Without metals, cars cannot be produced; skyscrapers cannot be built; and electricity cannot be delivered. In the present global strive for the development of strong and light metals, a great effort has been put into producing nanostructured metals by plastic deformation to high strains (Humphreys *et al.* 1999; Hansen 2004; Huang 2009). Nanostructured metals have a high strength but a low ductility. Therefore proper annealing treatments are required in order to improve the ductility without losing too much strength. However, nanostructured metals are also characterized by a high stored energy (J/m^3), which serves as the driving pressure (N/m^2) for recovery and recrystallization (Driver 2004; Hansen *et al.* 2008). In other words, nanostructured metals have a poor thermal stability. Therefore, studies on the effect of heat treatments on the structure and properties of nanostructured metals are of great importance in order to optimize the properties for application.

Metals deformed to high strains have a high stored energy, and also a very different structure compared to that deformed to low strains (Hughes and Hansen 2000; Liu *et al.* 2002). Consequently, the restoration behaviour during annealing of heavily deformed nanostructured metals may be significantly different from that deformed to low strains. The restoration processes are conventionally classified into three categories: recovery, recrystallization and grain growth (Martin and Doherty 1976; Humphreys and Hatherly 2004). In order to retain the high strength of nanostructured metals,

the focus is on recovery, which is the first stage of restoration processes, and both mechanisms (recovery mechanisms and rate-controlling atomic mechanisms) and kinetics are important.

This project is to study the recovery mechanisms and kinetics of nanostructured aluminium produced by plastic deformation to high strains. The thesis is structured as following: Chapter 2 gives a short review of the background; Chapter 3 introduces the materials and methods used in this study; Chapter 4 reports a new recovery mechanism, namely triple junction motion; Chapter 5 reports the recovery behaviour at low temperatures (5~100°C); Chapter 6 reports the recovery kinetics at medium temperatures (140~220°C); and Chapter 7 gives conclusions and outlook.

Chapter 2

Background

This chapter provides the necessary theoretical and experimental background information for the current study, including deformation structures at different strains, general annealing behaviour of deformed metals, and some strain effects on recovery and recrystallization. Such background information is crucial since it is the basis for understanding the recovery and recrystallization behaviour of nanostructured metals produced by plastic deformation to high strains.

2.1 Deformation microstructure

The deformation microstructure is introduced in the following with an emphasis on metals with medium-to-high stacking fault energies (SFEs), e.g. aluminium (166 mJ/m^2), nickel (128 mJ/m^2) and copper (78 mJ/m^2) (Murr 1975), processed under conditions where plastic deformation takes place mainly by slip. Figure 2.1 shows a typical deformation structure after low strain revealed by transmission electron microscopy (TEM) (Liu *et al.* 1998). Such a structure is usually called a cell block structure, where regions of the same slip activity forming cell blocks, which are further divided into cells (Bay *et al.* 1992; Hansen 2001). The structural morphology changes as the strain increases. Figure 2.2 shows a typical deformation structure after high strain, characterized by extended lamellae evolved from cell blocks (Hughes

and Hansen 2000). The lamellar boundaries are finite, forming triple junctions where they meet. These triple junctions in a lamellar structure are important, and will be studied in detail in Chapter 4.

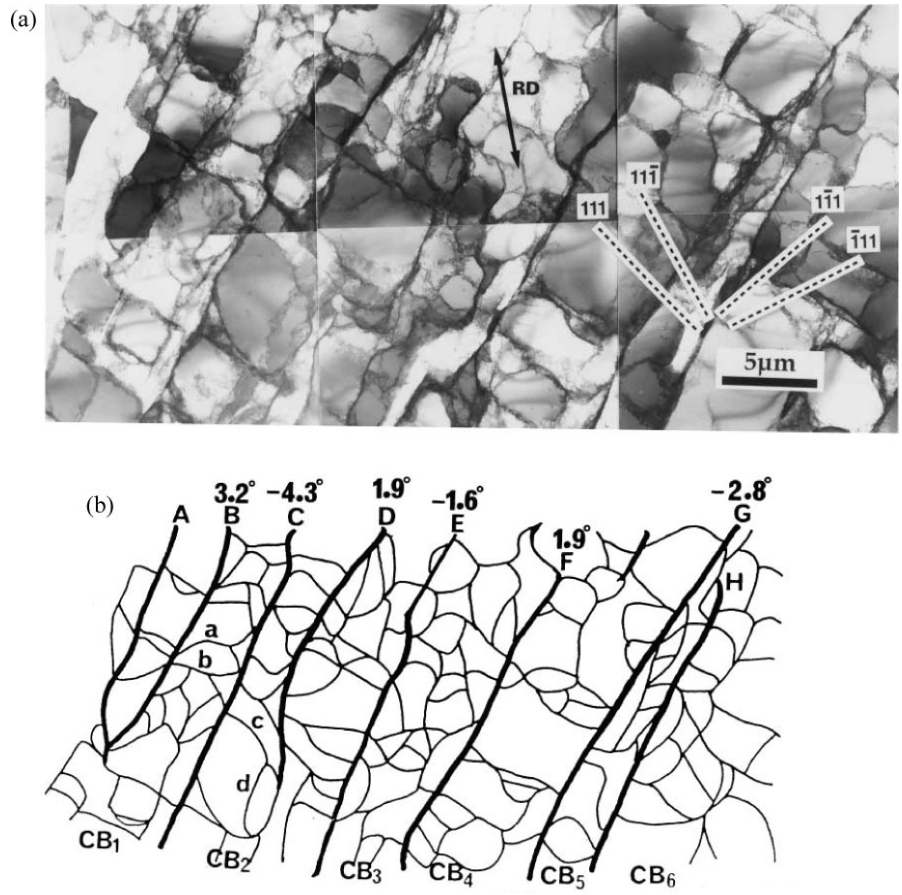

Figure 2.1: (a) A TEM image of a cell block structure in 10% cold-rolled (true strain 0.1) aluminium (99.996% purity) viewed in the longitudinal plane, where RD is the rolling direction. (b) A sketch of the same area showing the traces of boundaries and the misorientation angles between adjacent cell blocks (CBs). Cell block boundaries are marked as A, B, C, *etc.* and cell boundaries are marked as a, b, c, d. Reproduced from Liu *et al.* (1998).

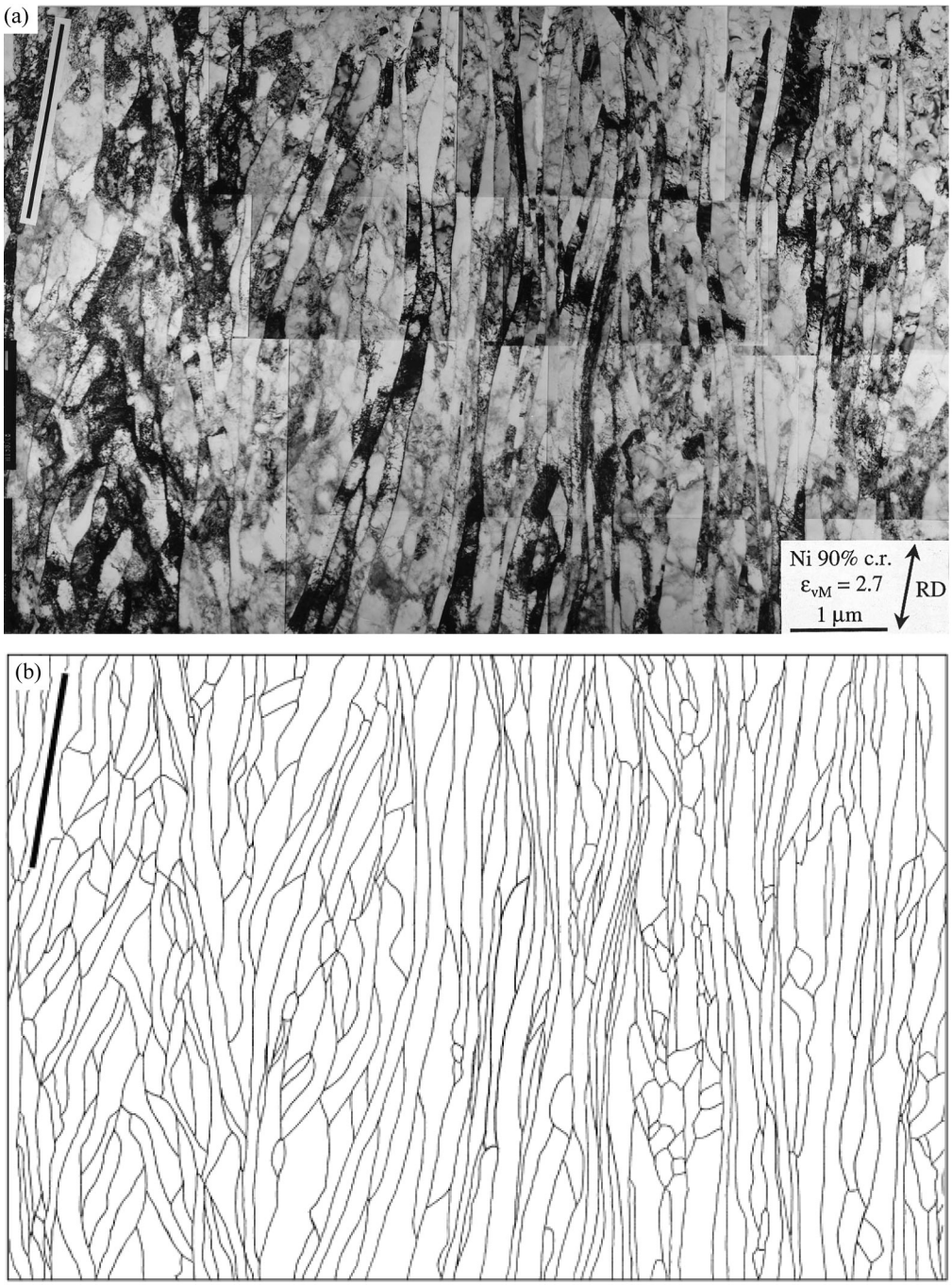

Figure 2.2: (a) A TEM image of a lamellar structure in 90% cold-rolled (true strain 2.3) nickel (99.99% purity) viewed in the longitudinal plane, where RD is the rolling direction. (b) A sketch of the same area showing the traces of lamellar boundaries. Reproduced from Hughes and Hansen (2000).

Cell block boundaries at low strains and lamellar boundaries at high strains are both geometrically necessary boundaries (GNBs) since they are assumed to delineate regions with different slip activities, whereas cell boundaries at

low strains and interconnecting boundaries at high strains are both incidental dislocation boundaries (IDBs) since they are assumed to form by mutual trapping of glide dislocations (Kuhlmann-Wilsdorf and Hansen 1991; Hansen 2001). For both GNBs and IDBs, the average boundary spacing decreases and the average misorientation angle across the boundary increases, when the strain is increased as shown in Figure 2.3 (Hughes and Hansen 2000). However, it can be also seen in Figure 2.3 that the rate of change is very different for the two types of boundaries, indicating different mechanisms controlling their evolution.

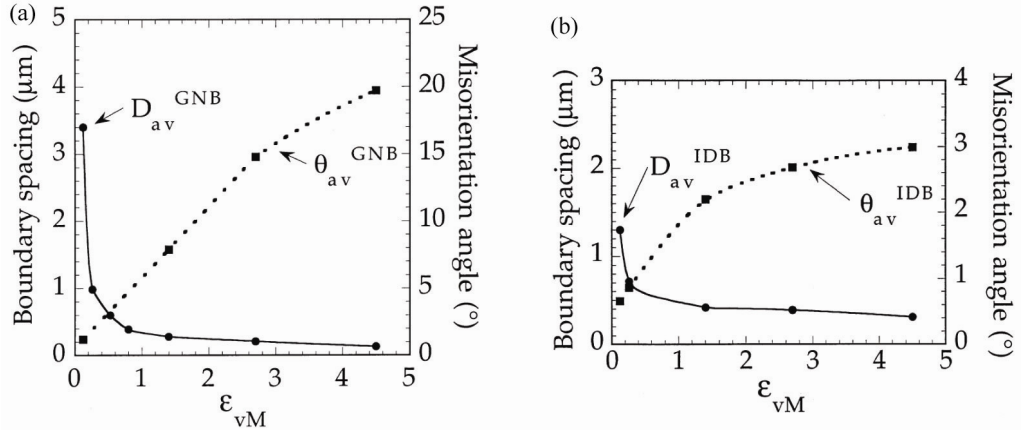

Figure 2.3: Evolution of the average boundary spacing and the average misorientation angle (measured by TEM) in nickel (99.99% purity) for (a) GNBs and (b) IDBs as the strain of rolling increases. The von Mises strain (ε_{vM}) is used in the plots, and it is proportional to the true strain (ε_t) as $\varepsilon_{vM}=2\varepsilon_t/\sqrt{3}$. Reproduced from Hughes and Hansen (2000).

In addition to the change in the structural morphology and structural parameters, the stored energy of deformation also changes when the strain is increased as shown in Figure 2.4 (Knudsen *et al.* 2008; Cao *et al.* 2009; Godfrey and Liu 2009). It can be seen that the estimated stored energy not only depends on the measuring technique but also on the deformation mode. However, the estimated stored energy increases monotonically with increasing strain over a large strain range independent of the measuring technique and the deformation mode.

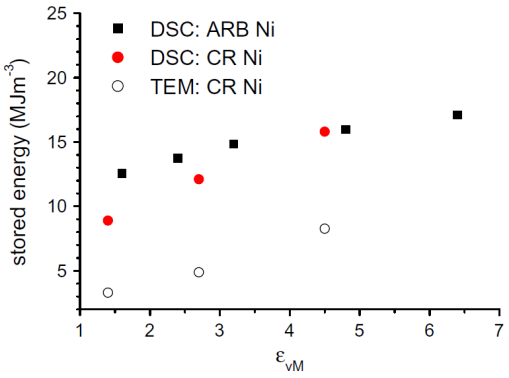

Figure 2.4: Stored energy measured by differential scanning calorimetry (DSC) and from TEM measurements for nickel (99.99% purity) deformed by cold rolling (CR) (Knudsen *et al.* 2008) and accumulative roll bonding (ARB) (Cao *et al.* 2009). Reproduced from Godfrey and Liu (2009).

Metals deformed to high strains typically have a finely-spaced lamellar structure and a high stored energy. In the present study, these metals are called nanostructured metals since they contain structural features which are on the nanometre scale.

2.2 Recovery

When a deformed metal is heated, restoration processes take place, releasing the deformation stored energy. Consequently, the physical and mechanical properties also return to that corresponding to an undeformed state. Two examples are shown in Figure 2.5, where copper and nickel deformed by torsion are heated (Clarebrough *et al.* 1955). The restoration processes are complex, and they depend on a number of factors, e.g. the material and its purity, the deformation strain, and the annealing temperature (Humphreys and Hatherly 2004). The restoration processes are generally classified into three categories: recovery, recrystallization, and grain growth. Recovery is conventionally defined as all annealing processes occurring in deformed materials that occur without the migration of a high angle grain boundary (Martin and Doherty 1976; Doherty *et al.* 1997). High angle boundaries are those with misorientation angles greater than 10~15° (Doherty

et al. 1997), and in the present study 15° is chosen as the cut-off angle. Recovery is supposed to be responsible for the change of the physical and mechanical properties and the release of the stored energy at the early stage of an annealing treatment as shown in Figure 2.5.

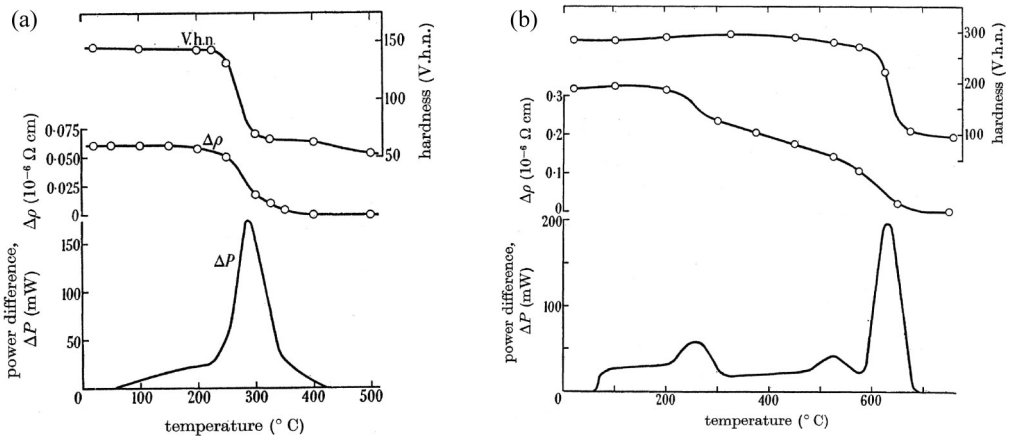

Figure 2.5: Release of stored energy (ΔP) and changes of electrical resistivity ($\Delta\rho$) and hardness for (a) copper (99.96% purity) and (b) nickel (99.6% purity) deformed by torsion to a shear strain of 5.87 and heated at 0.1 K/s. Reproduced from Clarebrough *et al.* (1955).

A number of different processes take place during recovery of a deformed metal, and a schematic sketch is shown in Figure 2.6 based on an ideal dislocation cell structure independent of strain (Humphreys and Hatherly 2004). In this ideal cell structure, dislocation cells evolve into subgrains, which are bounded by well-ordered low angle boundaries, whereas cell blocks at low strains (Figure 2.1) and lamellae at high strains (Figure 2.2) are not considered. Recovery processes may take place during annealing after deformation, and they may also take place in the course of deformation as dynamic recovery. It is shown in the previous section that a cell block structure or a lamellar structure is formed in metals with medium-to-high stacking fault energies, with relatively clean regions between boundaries, indicating that recovery processes take place during deformation and/or during storage after deformation. Therefore in such metals, especially deformed to high strains, subgrain growth is an important recovery process during subsequent annealing. The growth of subgrains can be either continuous (uniform coarsening, normal subgrain growth) or discontinuous

(non-uniform coarsening, abnormal subgrain growth) as illustrated in Figure 2.7 (Humphreys 1997a).

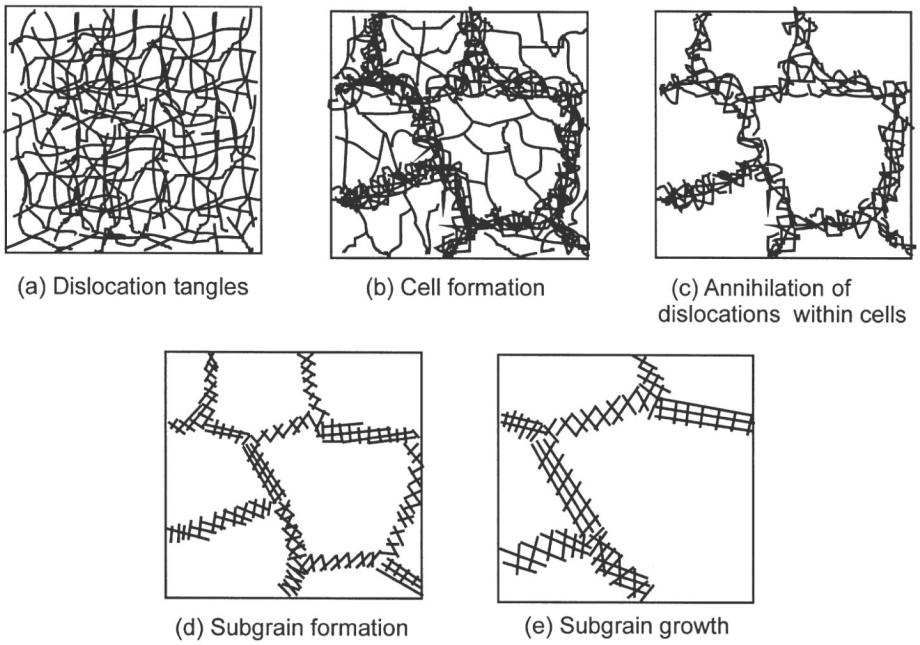

Figure 2.6: Various stages of recovery in an idealized dislocation cell structure. Reproduced from Humphreys and Hatherly (2004).

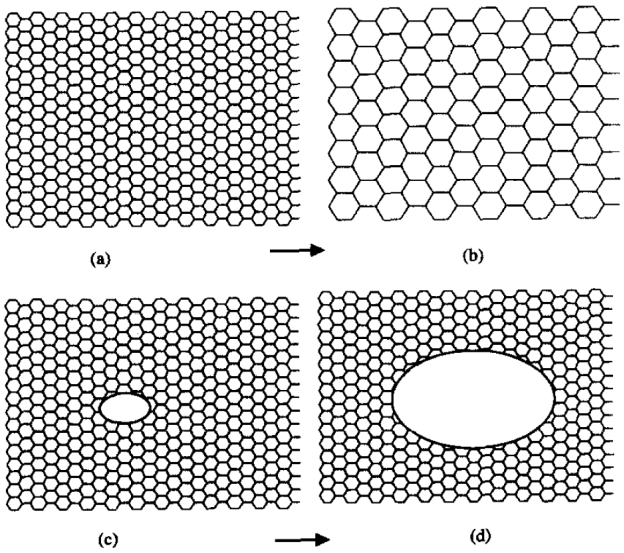

Figure 2.7: Schematic illustration of (a-b) continuous and (c-d) discontinuous annealing phenomena in an idealized cellular structure. Reproduced from Humphreys (1997a).

In addition to the recovery processes (mechanisms) sketched in Figure 2.6, the global recovery kinetics is also important. One example is shown in Figure 2.8, where cold-rolled commercial purity aluminium with 0.43 wt% Fe and 0.09 wt% Si is isothermally annealed at six different temperatures and the hardness shows a quasi-logarithmic decay in the recovery range (Furu *et al.* 1995). As shown in Figure 2.8, the recovery rate increases dramatically with increasing annealing temperature, indicating thermal activation of recovery processes.

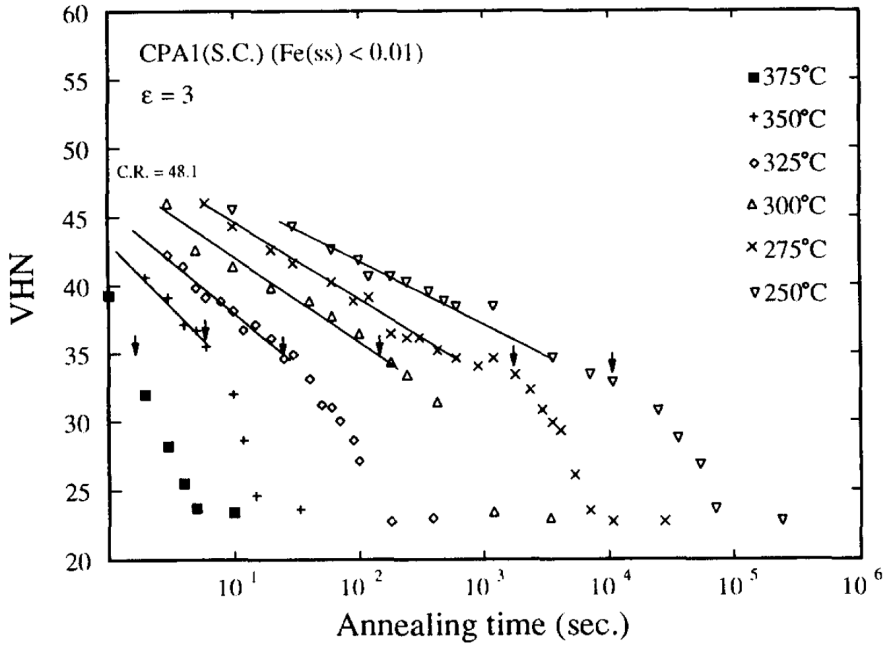

Figure 2.8: Hardness as a function of annealing time at the given temperatures for commercial purity aluminium with 0.43 wt% Fe and 0.09 wt% Si cold rolled to a true strain of 3. The arrows indicate initiation of recrystallization. Reproduced from Furu *et al.* (1995).

2.2.1 Previous studies of recovery mechanisms

The recovery of metals deformed to low-to-medium strains has been studied extensively half a century ago, as reviewed by Beck (1954), Bever (1957), and Perryman (1957). The early recovery studies were primarily focused on the release of the stored energy and the changes in the physical and mechanical properties (e.g. Clarebrough *et al.* 1955), and the main

interpretations of the recovery processes are mutual annihilation of dislocations with opposite Burgers vectors and rearrangement of dislocations into low angle subgrain boundaries (Bever 1957; Friedel 1964; Lytton *et al.* 1965). It was later found by TEM that subgrain growth is also an important recovery process, either by subgrain coalescence (Hu 1962; Li 1962) or by subgrain boundary migration (Gleiter 1969; Smith and Dillamore 1970). While dislocation annihilation and reconfiguration may be the dominating recovery mechanism in metals of low stacking fault energies, subgrain growth by subgrain boundary migration seems to be more important in metals of medium-to-high stacking fault energies, especially after a high strain (Nes 1995; Furu *et al.* 1995). Hence the recovery processes clearly depends on many parameters.

2.2.2 Empirical kinetic relationships

Various kinetic equations based on specific recovery mechanisms have been proposed in terms of dislocation density, subgrain size and flow stress (Li 1962; Sandstrom 1977a,b; Prinz *et al.* 1982; Doherty and Szpunar 1984; Furu *et al.* 1995). However, these equations are generally limited and are only valid in special cases since recovery consists of a number of complex processes, which depend on a number of parameters. In order to adequately describe the global recovery kinetics, various empirical rate equations proposed half a century ago (Bever 1957) are still valid.

If P is a material property, decreasing during annealing, then a logarithmic decay of the property corresponds to the following rate equation:

$$\frac{dP}{dt} = -\frac{c_1}{t}, \tag{2.1}$$

where c_1 is a constant and t is the annealing time. However, the relationship between the property and the time is indirect, and Equation (2.1) leads to an infinite rate at the beginning of recovery, which is certainly not valid. To overcome the above two problems, the following equation may be preferred:

$$\frac{dP}{dt} = -c_2 P^m \exp(-\frac{Q_0}{RT}), \tag{2.2}$$

where c_2 and m are constants, Q_0 is the activation energy independent of temperature, R is the gas constant, and T is the absolute temperature. Equation (2.2) is an m^{th}-order reaction rate equation with a constant activation energy. However, it has been shown that the apparent activation energy for recovery increases as recovery proceeds (e.g. Michalak and Paxton 1961; Furu *et al.* 1995; Vandermeer and Hansen 2008), and therefore the recovery rate equation first proposed by Kuhlmann (1948) may give a better description:

$$\frac{dP}{dt} = -c_3 \exp(-\frac{Q_0 - \beta P}{RT}), \tag{2.3}$$

where c_3 and β are constants. However, Equation (2.3) has a problem at the end of recovery, i.e. the rate never goes to zero. A more flexible equation has been proposed by Borelius *et al.* (1952):

$$\frac{dP}{dt} = -PK_0 \exp(-\frac{Q_0 - \beta P}{RT}), \tag{2.4}$$

where K_0 is a constant. Equation (2.4) may be recognized as a first-order reaction rate equation with an apparent activation energy depending on its extent of recovery already taken place. It may describe the whole range of recovery, and is therefore preferred by some authors (Vandermeer and Rath 1990; Vandermeer and Hansen 2008).

2.3 Recrystallization and grain growth

Recrystallization is conventionally defined as the formation of a new grain structure in a deformed material by the formation and migration of high angle boundaries driven by the stored energy of deformation, and grain growth is conventionally defined as processes involving the migration of grain boundaries when the driving force for migration is solely the reduction of the grain boundary area itself (Doherty *et al.* 1997). Both recrystallization

(Doherty *et al.* 1986; Driver 1995) and grain growth (Ralph 1990) are complex. Similar to subgrain growth during recovery, both recrystallization and grain growth can be either continuous or discontinuous, as illustrated in Figure 2.7. However, the categorization of continuous (homogeneous) and discontinuous (heterogeneous) is simply phenomenological, and it does not imply operation of any particular mechanisms.

Recovery and recrystallization are driven by the deformation stored energy, whereas grain growth is driven by the reduction of boundary area. However, all processes may lead to coarsening of the microstructure, and the deformation stored energy is mainly associated with all types of deformation-induced boundaries (Godfrey and Liu 2009). With increasing sophistication of the tools for microstructural characterization, the borderlines between different restoration phenomena (i.e. subgrain growth, recrystallization, and grain growth) are often blurred, especially for metals deformed to high strains (e.g. Jazaeri and Humphreys 2004; Ferry and Burhan 2007). Indeed, a unified theory of growth of cellular microstructures has also been proposed by Humphreys (1997a,b) based on an idealized cell structure, and it may be used to predict the growth stability of metals during annealing.

2.4 Strain effect on recovery and recrystallization

When the strain is increased, the average spacing between boundaries decreases and the average misorientation angle across boundaries increases. Meanwhile, the fraction of high angle boundaries, which have high energies and high mobility, increases and the global driving pressure for recovery and recrystallization also increases. Consequently, when the strain is increased, the recovery rate increases (Furu *et al.* 1995; Vandermeer and Hansen 2008), and the recrystallization behaviour may also vary significantly (Oscarsson *et al.* 1993; Jazaeri and Humphreys 2004). One example is shown in Figure 2.9, where significantly different restoration patterns can be found in samples deformed to different strains (Cao *et al.* 2009). It is shown that rapid recovery

takes place in samples deformed to a high strain, and a relatively low activation energy may be involved for the recovery at low temperatures.

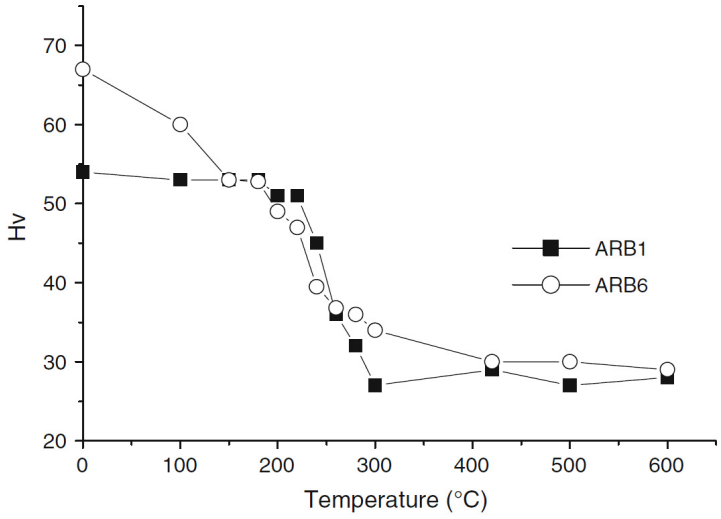

Figure 2.9: Change in hardness with annealing temperature (isochronal annealing for two hours) of commercial purity aluminium (99.2% purity) deformed by accumulative roll bonding to one pass (ARB1) and six passes (ARB6). Reproduced from Cao *et al.* (2009).

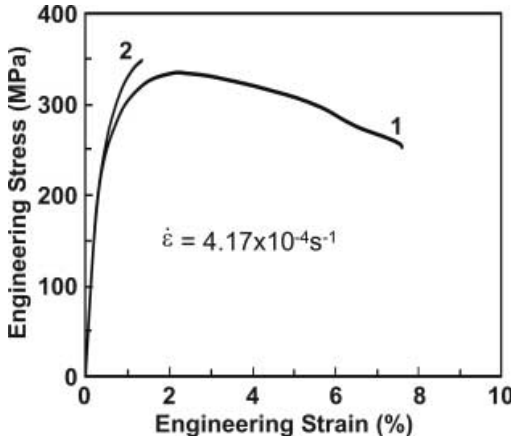

Figure 2.10: Engineering stress-strain curves for commercial purity aluminium (99.2% purity). Curve 1: processed by six ARB cycles. Curve 2: same material as 1, plus annealing at 150°C for 0.5 h. The strain rate is indicated. Reproduced from Huang *et al.* (2006a).

A number of processes may be involved during recovery of nanostructured metals produced by plastic deformation to high strains, and the consequence of annealing may also differ from the usual case. It is shown in Figure 2.10

that a short-time recovery annealing leads to hardening and decrease of ductility of the nanostructured aluminium produced by accumulative roll bonding (ARB) to six cycles (Huang *et al.* 2006a). A similar phenomenon was also observed in high purity aluminium, and it was therefore suggested by Huang *et al.* (2006a) that the hardening by annealing may be due to the shortage of dislocation sources.

2.5 Overview of the thesis

The objective of this study is to explore and analyze the effect of heat treatments on the structure and properties of nanostructured metals processed by plastic deformation to high strains.

Chapter 3 introduces the materials and techniques used in this study. Nanostructured aluminium of commercial purity is chosen in view of its possible application in the car industry. For the recovery annealing, 220°C is chosen as the highest annealing temperature since a previous study (Vandermeer and Hansen 2008) showed that annealing at this temperature for ~100 h led to the nucleation of recrystallization in commercial purity aluminium. As for the lowest annealing temperature, the refrigerator temperature (5°C) and room temperature (~20°C) are chosen in order to examine the thermal stability of nanostructured aluminium at low ambient temperatures. A number of techniques, including electron backscattered diffraction (EBSD), transmission electron microscopy (TEM), and positron annihilation lifetime spectroscopy (PALS), are used in order to characterize the structural changes on different length scales to identify possible recovery mechanisms. Moreover, hardness tests are used to follow the recovery kinetics and to estimate the activation energy of recovery.

Chapter 4 reports a new recovery mechanism in a heavily deformed lamellar structure. The new recovery mechanism, namely triple junction motion, explains the microstructural coarsening of a heavily deformed material and the evolution from a lamellar structure to a more equiaxed

structure. The new mechanism operates in a wide temperature range (from room temperature to 220°C), and its rate increases with increasing annealing temperature. To further characterize the recovery mechanisms and kinetics in nanostructured aluminium, further experimental work is carried out in two different temperature ranges. Chapter 5 reports the recovery at low temperatures (5~100°C), which is important for possible application of nanostructured metals. In this temperature range, the structure is rather stable, and annihilation and reconfiguration of zigzagged dislocations is found to be an important recovery mechanism, associated with a low activation energy. On the other hand, Chapter 6 reports the recovery at medium temperatures (140~220°C), which is important to tailor the structure and properties of nanostructured metals. Chapter 6 also presents a new recovery model, which is successfully applied to the present data, showing the activation energy of recovery increases as recovery proceeds and approaches ~190 kJ/mol at the end of recovery, pointing at this stage to an effect of solute drag during recovery as in recrystallization. Chapter 7 gives conclusions and outlook.

Chapter 3

Materials and techniques

This chapter introduces the materials and experimental techniques used in this study. Nanostructured aluminium is beginning to play an important role in terms of making cars even lighter, enabling them to stand collisions without fatal consequences for the passengers. However, recovery of the nanostructured aluminium at low temperatures may lead to softening of the material, and therefore determining and improving the thermal stability of nanostructured aluminium is crucial for their practical application. Commercial purity aluminium is chosen in this study, partly due to its broad application in the industry, and partly due to its moderate impurity level, which may allow recovery to take place at low annealing temperatures and meanwhile limit recovery during sample preparation at room temperature.

Commercial purity aluminium is plastically deformed to high strains and then annealed at various temperatures. A number of techniques are used to follow the structural changes on different length scales to identify possible recovery mechanisms. Vickers hardness tests are used to capture the global recovery behaviour and to analyze its recovery kinetics and the activation energy; electron backscattered diffraction (EBSD) is used to characterize the evolution of the microstructure and texture; transmission electron microscopy (TEM) is used to study the fine details of the recovery of dislocations and boundary structures; and positron annihilation lifetime spectroscopy (PALS) is used to study the vacancy-type defects.

3.1 Cold rolled AA1050 aluminium

Two batches of commercial purity aluminium AA1050 are used for the present study. The two batches have a similar initial grain size (~100 μm) and a similar chemical composition, mainly 99.5Al-0.25Fe-0.15Si (wt pct) as measured by optical emission spectroscopy (Table 3.1). Batch I comes from the GFF basic material (Knudsen 2006), and is cold rolled to true strains (logarithmic strains) 2 and 4, corresponding to 86.5% and 98.2% thickness reduction, respectively. The same material was also used in a previous recovery study by Vandermeer and Hansen (2008). Batch II is supplied by Dr. O. V. Mishin and cold rolled to a true strain of 5.5, corresponding to 99.6% thickness reduction, and the final thickness is 0.4 mm. More details on the rolling schedule of the strain 5.5 aluminium can be found in Mishin *et al.* (2010).

Table 3.1: Chemical composition (wt pct) of commercial purity aluminium cold rolled to true strains 2, 4 (CR2,4) and 5.5 (CR5), and deformed by ARB for 6 cycles (ARB6).

	Al	Si	Fe	Cu	Mn	Mg	V	Zn	Ti	B
CR2,4	99.5	0.16	0.24	0.004	0.005	0.003	0.007	0.013	0.023	0.004
CR5	99.5	0.15	0.25	0.006	0.007	<0.001	0.009	0.012	0.041	<0.001
ARB6	99	0.11	0.67	0.14	0.004	0.003	0.011	0.003	0.014	0.001

In the present study, true strains of 2 and higher are considered as high strains since the corresponding deformation structures show lamellar morphology. However, the focus is on the aluminium deformed to the highest strain. Due to the high stored energy in the heavily deformed state, recovery may take place at ambient temperatures. Therefore immediately after cold rolling, one piece of the strain 5.5 aluminium is stored in a freezer (about -20°C) to retard recovery, whereas all other samples of three strains are kept at room temperature (about 20°C).

3.2 ARB deformed AA1100 aluminium

Commercial purity aluminium AA1100, with a main chemical composition of 99Al-0.67Fe-0.14Cu-0.11Si (wt pct) as measured by optical emission spectroscopy (Table 3.1) is deformed by accumulative roll bonding (ARB). The principle of ARB is illustrated in Figure 3.1 (Tsuji *et al.* 2003). After degreasing and wire brushing, two sheets of the starting material are stacked and roll bonded to 50% thickness reduction in one pass at room temperature without using any lubricant. This procedure defines one cycle of ARB. The rolled sheet is then cut to half its length, stacked and roll bonded again. Without changing the rolling direction, the ARB process is repeated to six cycles, accumulating a total thickness reduction of 98.4%, corresponding to a true strain of 4.2 (von Mises strain 4.8). The ARB samples are supplied by Dr. N. Kamikawa.

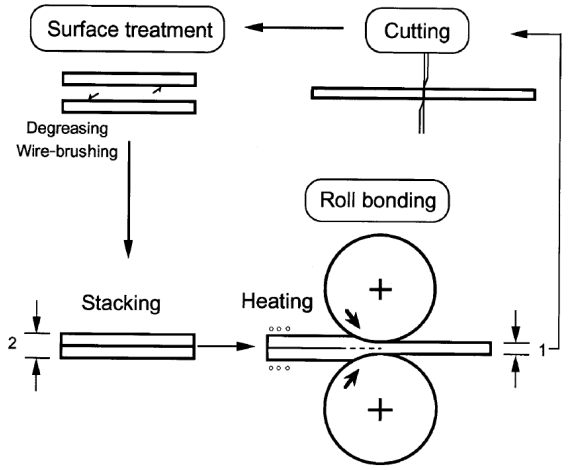

Figure 3.1: A sketch showing the principle of the ARB process. Reproduced from Tsuji *et al.* (2003).

3.3 Annealing

Most of the annealing treatments are carried out in air furnaces. These furnaces can be pre-heated to a desired temperature before insertion of a sample and held stable within ±2°C. The samples are placed in the middle of

furnace tubes, where the temperature is measured by thermocouples. A typical size of a sample is 5 mm × 6 mm × 0.4 mm, and therefore a short time is expected for the sample to reach the desired temperature in the furnace. Due to the same reason, a short cooling time is also expected when the sample is taken out from the furnace and cooled in the air.

When the annealing time is reduced, the requirement of annealing accuracy increases. For annealing at ≤220°C for time intervals less than one hour, a silicone oil bath is used. The oil bath has a similar accuracy as the air furnaces (±2°C) and can also be pre-heated to a desired temperature before insertion of a sample. However, the time required for the sample to reach the desired temperature is expected to be even shorter. In these cases, the sample is cooled in the water after being taken out from the oil bath, giving a shorter cooling time too.

For annealing at very low temperatures, special facilities are used. For annealing at 5°C, the samples are placed in a laboratory refrigerator; for annealing at 20°C, the samples are placed in a basement with a stable air-conditioning. In these cases, the temperature fluctuation is also within ±2°C.

3.4 Scanning electron microscopy

Scanning electron microscopy (SEM) images a sample by scanning with a high energy electron beam, which interacts with the sample and produces signals containing information of the interaction volume. As in visible-light microscopy, bulk samples are typically used for SEM observations; however, the spatial resolution of SEM is typically ~100 times better than visible-light microscopy due to the very fine electron beam. A number of signals are generated when the electron beam interacts with the sample, and two commonly used signals are the secondary electrons (SEs) and the backscattered electrons (BSEs). The contrast of SE imaging primarily depends on the sample topography, whereas the contrast of BSE imaging strongly depends on the atomic number and the crystallographic orientation

of the sample. The orientation contrast in BSE imaging comes from the electron channelling contrast (ECC), and it is very useful in studying the boundary structure and lattice defects in metals (Wilkinson and Hirsch 1997).

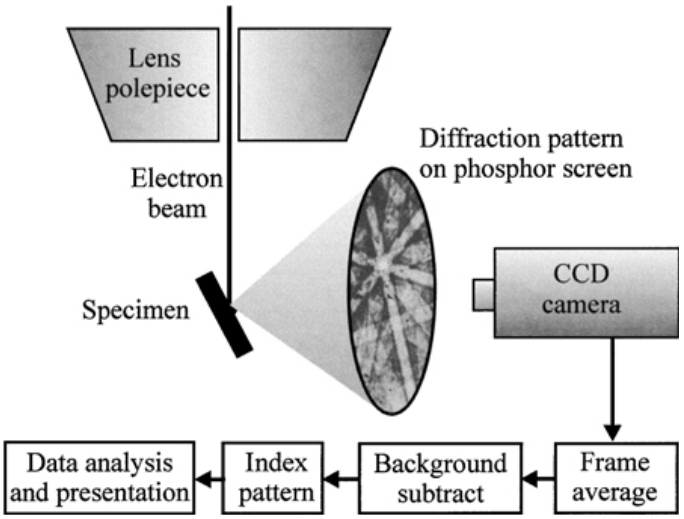

Figure 3.2: A schematic diagram of a typical EBSD installation, where the specimen is typically 70° tilted. Reproduced from Humphreys (2001).

A relatively new SEM technique, namely electron backscattered diffraction (EBSD), has reached the state of maturity in the past two decades. The principle of the EBSD technique is illustrated in Figure 3.2 (Humphreys 2001). The electron beam hits a titled crystalline specimen, generating a Kikuchi diffraction pattern, which is analyzed automatically by a computer to determine the crystallographic orientation of the scanned point. With a field emission gun (FEG), the spatial and angular resolution of EBSD is about 20 nm and 1°, respectively (Humphreys 2004). A number of different applications can be found in the literature, and the technique is very useful in studying crystalline materials.

In the present study, a Zeiss Supra-35 FEG scanning electron microscope, equipped with an HKL Channel 5 EBSD system, is used. The microscope is operated at 15 kV for both BSE imaging and EBSD observations. Samples for SEM analysis are mechanically polished followed by electropolishing in a solution of ethanol (70%), water (12%), 2-butoxy-ethanol (10%), and perchloric acid (8%) at about 2°C for 45 seconds with a potential difference

of 13 V. The SEM characterizations are primarily carried out in the longitudinal plane, the plane containing the rolling direction (RD) and the normal direction (ND). For EBSD analysis, a step size of 30 nm is typically used for the study of deformation structures, whereas larger step sizes are selected for texture studies and orientation mapping of annealed samples. EBSD data are post-processed using HKL Channel 5 software to remove bad data points and to mildly smooth the orientation noise to suit the critical angle of 1.5° in boundary detection. The lamellar boundary spacings in EBSD data sets are all determined automatically by the line interception method and the intercept length is determined along ND by defining a threshold misorientation angle of 1.5°. All EBSD maps used in determining the lamella boundary spacing are scanned along ND to minimize errors from image drift.

In addition to conventional post mortem observations, *ex situ* EBSD observations (observations at the same area between annealing steps) are also carried out in order to follow the evolution of the boundary structure during recovery annealing of bulk specimens. For the *ex situ* study, one selected area in a deformed specimen is first characterized by EBSD and then the specimen is removed from the microscope sample stage and annealed in an air furnace or simply exposed at room temperature for different time intervals. After annealing, the specimen is mounted back in the stage the same way according to macroscopic markers, and an EBSD orientation map is obtained of the original selected area according to the carbon contamination left after the first scan. In principle the EBSD step size should be selected to be as small as possible for the present highly-strained material. However, fine step sampling results in a strong electron beam induced carbon contamination of the scanned region. Therefore in most cases a step size of 30 nm is chosen. Besides, a partial tilt correction around ND (46.8° tilt correction in software instead of the physical tilt angle 70° as shown in Figure 3.2) is applied in the scanning geometry, resulting in a real step size of 60 nm in RD (since $\cos 46.8° = 2\cos 70°$) to further reduce carbon contamination. The maps are then expanded in RD to create an artificial step size of 30 nm to be consistent with the step size in ND.

3.5 Transmission electron microscopy

Compared to SEM, transmission electron microscopy (TEM) has an even higher resolution, below 0.1 nm for the best instruments (Williams and Carter 2009). The transmission electron microscope is extremely versatile, and a number of different signals can be utilized in various operation modes. For example, it can be operated in a diffraction mode and an imaging mode; it can produce a parallel beam and a convergent beam; it can form a bright field image and a dark field image; it can form amplitude contrast and phase contrast. However, the specimen for TEM observation must be very thin (typically 0.1~0.5 μm for aluminium) in order to be electron beam transparent.

In the present study, a JEM 2000FX transmission electron microscope, with a LaB_6 filament and a CCD (charge-coupled device) camera, is used. The microscope is operated at a relatively low accelerating voltage of 120 kV in order to minimize beam damage in aluminium, and all micrographs are taken at the same objective lens current to minimize errors in magnification. The TEM foils are prepared using a modified window technique (Christiansen *et al.* 2002), and large thin areas (~400 μm^2) are typically produced. Bright field imaging is used for general microstructural characterizations, and weak-beam dark field (WBDF) imaging is applied for observations of detailed dislocation structures and vacancy-type defects. In addition, convergent beam electron diffraction (CBED) is also extensively used in order to (i) adjust the tilt angle of the TEM holder for two-beam or multi-beam conditions, (ii) determine the foil thickness for dislocation density measurement, and (iii) use the Kikuchi pattern for orientation and misorientation measurement (Liu 1994, 1995).

The density of dislocations in the volume between boundaries is determined by TEM. For each specimen, the dislocations in a given cell are examined by aligning a <110> zone axis close to the electron beam direction, allowing all the dislocations within the given cell being visible. Test lines are then drawn randomly within the given cell in the micrograph taken under the

multi-beam condition. The dislocation density (ρ_d) is then calculated (Hirsch *et al.* 1977) as:

$$\rho_d = \frac{2N_L}{t^{foil}}, \tag{3.1}$$

where N_L is the number of interceptions at dislocations per unit test line and t^{foil} is the foil thickness. In order to reduce the standard error of measurement, typically ~30 cells in a rectangular region of thickness 0.2~0.3 μm are examined.

As in the EBSD analysis, *ex situ* observations are also carried out by TEM in order to follow the detailed microstructural evolution during recovery annealing. For selected areas in a TEM thin foil of the deformed state, the deformation structure is imaged, and the boundary misorientation angles are determined. The TEM foil is then removed from the TEM holder and annealed in an air furnace, or simply exposed at room temperature for different time intervals. After annealing, the sample is mounted back in the TEM holder according to predefined macroscopic markers, allowing the same area to be examined repeatedly after annealing. Despite careful alignment during mounting of the TEM foil, a misalignment angle (typically 1~5°) is always observed, and therefore a further alignment of TEM micrographs is also carried out using the imaged shape of the hole near the thin area as a reference.

3.6 Positron annihilation lifetime spectroscopy

Positron annihilation lifetime spectroscopy (PALS) is a well-established high-sensitivity technique for detecting vacancy-type defects (vacancies, open volumes at boundaries, voids, etc) in solids. Figure 3.3 illustrates the interaction between positrons and a solid specimen (Dupasquier *et al.* 2004), and the positron lives for a longer lifetime when trapped at a vacancy-type defect due to its relatively low electron density. Therefore, by measuring the spectrum of the positron lifetime when implanted to a specimen, information

regarding vacancy-type defects within the specimen can be obtained (Eldrup and Singh 1997).

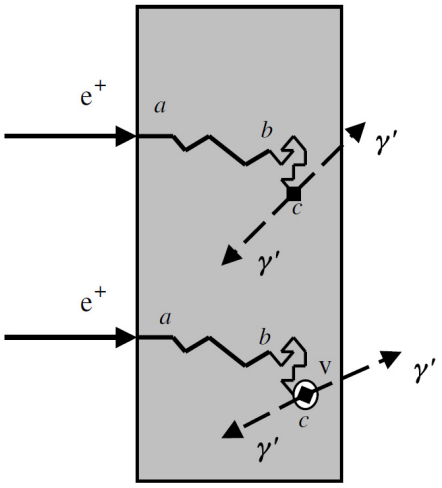

Figure 3.3: A sketch of possible fates of positrons (e^+) implanted in a solid specimen. Upper track: implantation at *a*, slowing-down from *a* to *b*, thermal diffusion from *b* to *c*, annihilation at *c* with a bulk electron and emission of two photons (*γ'*). Lower track: a similar fate but trapped at *c* in a vacancy-type defect (v) and lives a longer time before annihilation. Reproduced from Dupasquier *et al.* (2004).

In the present study, PALS measurements are carried out using a ^{22}Na positron source and a conventional fast-fast lifetime spectrometer. Typically two million or more counts are collected for each spectrum. PALS data are analyzed with the PALS*fit* programme (Olsen *et al.* 2007), using spectra of annealed high purity aluminium (99.996% purity) to determine the spectrometer time resolution and the source correction. All PALS experiments and analyses are carried out with the help of Dr. M. Eldrup.

3.7 Hardness tests

Hardness tests are used to determine the hardness of a material to deformation, and the tests can be performed on a macroscopic or microscopic scale. Hardness is not an intrinsic material property, but a result of a defined measurement procedure. However, in metals, the hardness generally

correlates linearly with the ultimate tensile strength. Therefore hardness tests in metals may be used as a quick measurement of the mechanical property of metallic samples since much less effort is required compared to tensile testing.

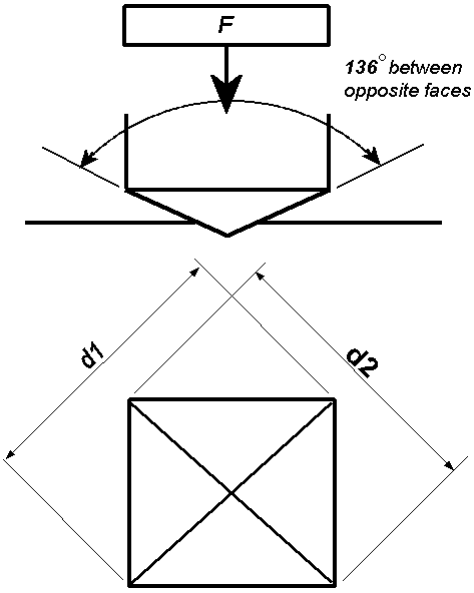

Figure 3.4: A sketch of the Vickers hardness test and the indentation formed.

In the present study, Vickers hardness tests are used. The Vickers hardness test consists of indenting the test material with a diamond indenter, in the form of a right pyramid with a square base and an angle of 136° between opposite faces subject to a load F (Figure 3.4). By measuring the two diameters (d_1 and d_2 in Figure 3.4) of the indentation formed, one can calculate the Vickers hardness (kgf/mm^2) according to the following equation:

$$\mathrm{HV} = 2F \sin\frac{136°}{2} \Big/ \left(\frac{d_1 + d_2}{2}\right)^2 . \tag{3.2}$$

In this study, samples for hardness tests are mechanically polished. Two hardness testers are used. For hardness measurement in the rolling plane, a Leitz Miniload Hardness Tester is used and a load of 200 g is applied for 10 seconds. For hardness measurement in the longitudinal plane, a Struers DuraScan 70 Hardness Tester is used and a load of 50 g is applied for 10

seconds. The small load applied in the latter case is to ensure that the distance between the indentations and the sample edge is always larger than three times the indentation size. The hardness value at each condition is taken as the average of at least eight random measurements, and the standard deviation, instead of the standard error, is calculated to show the local variation of hardness. Due to different hardness testers and different loads applied, the hardness values are only compared when they are measured in the same manner.

The hardness generally decreases during annealing of commercial purity aluminium. However, precipitation hardening and dislocation source limited hardening (Huang *et al.* 2006a) may also play a role in certain cases. In the present study, these hardening effects are negligible below 80°C and overshadowed by softening over 160°C. Therefore these hardening effects are only considered for annealing at 80~160°C, where part of the hardness data are excluded from the analysis of recovery kinetics.

Chapter 4

Recovery by triple junction motion

This chapter reports the identification and characterization of a phenomenologically new restoration mechanism in a heavily deformed lamellar structure. The new mechanism, namely triple junction motion, typically involves migration of high angle boundaries but largely retains the morphology of the deformation structure. Therefore the mechanism contradicts the conventional definition of recovery and recrystallization (see Sections 2.2 and 2.3) and blurs the difference between them. Nevertheless, triple junction motion is classified as a recovery mechanism in the present study since typical recrystallization is observed at lager stages of annealing (see Appendix).

The chapter starts with a short introduction of the background information, followed by a classification of three types of triple junctions in a lamellar structure and a stereological analysis of the triple junction densities. The experimental details and results are then presented, leading to the proposal of a new recovery mechanism.

This chapter is primarily based on Paper IV.

4.1 Introduction

The structural morphology at a large strain is represented by a rolled structure, composed of lamellae parallel to the rolling plane (Figure 4.1a,c).

The structure is very fine with a width of a few hundred nanometres for the individual lamellae. The lamellae have a finite length and they are subdivided by interconnecting boundaries (see sketch in Figure 4.1d). The lamellar structure illustrated in Figure 4.1 is a typical high strain structure in fcc (face centred cubic) and bcc (body centred cubic) metals deformed by a variety of modes such as rolling (Liu *et al.* 2002), high pressure torsion (Zhang *et al.* 2008), plane strain compression (Zahid *et al.* 2009) and equal channel angular extrusion (Valiev and Langdon 2006). The lamellar boundaries are typically medium and high angle boundaries and the interconnecting boundaries are predominantly low angle dislocation boundaries. Such a structure may also be found in transition or deformation bands, which can be observed both after medium and high strain deformation (Dillamore *et al.* 1972). This structure contains a high stored energy, primarily in different types of boundaries but also in the form of loose dislocations. Furthermore, triple junctions may possess extra energy beyond the energy of adjoining boundaries (Shekhar and King 2008; Godfrey and Liu 2009), and at a given strain, the dislocation density at or near triple junctions can also be significantly higher than at grain boundaries (Randle *et al.* 1996). The annealing behaviour of such a structure has been analyzed previously both theoretically and experimentally based on a general assumption that an initial step of recovery is the development of an equiaxed subgrain structure as forces from surface tension approach equilibrium (Dillamore *et al.* 1972; Jazaeri and Humphreys 2004). These analyses have been based on ideal structures where the lamellar boundaries are parallel and have infinite length and where the interconnecting boundaries are perpendicular to the lamellar boundaries. In such structures triple junctions (lines) connect lamellar boundaries and interconnecting boundaries with a dihedral angle, which is 90°, between the interfaces. However, real deformation structures have a different morphology, consisting of triple junctions with very different characteristics and therefore an expected different behaviour during annealing. This assumption is the basis for the following study encompassing a characterization of triple junctions in aluminium deformed to high strains and their behaviour during annealing.

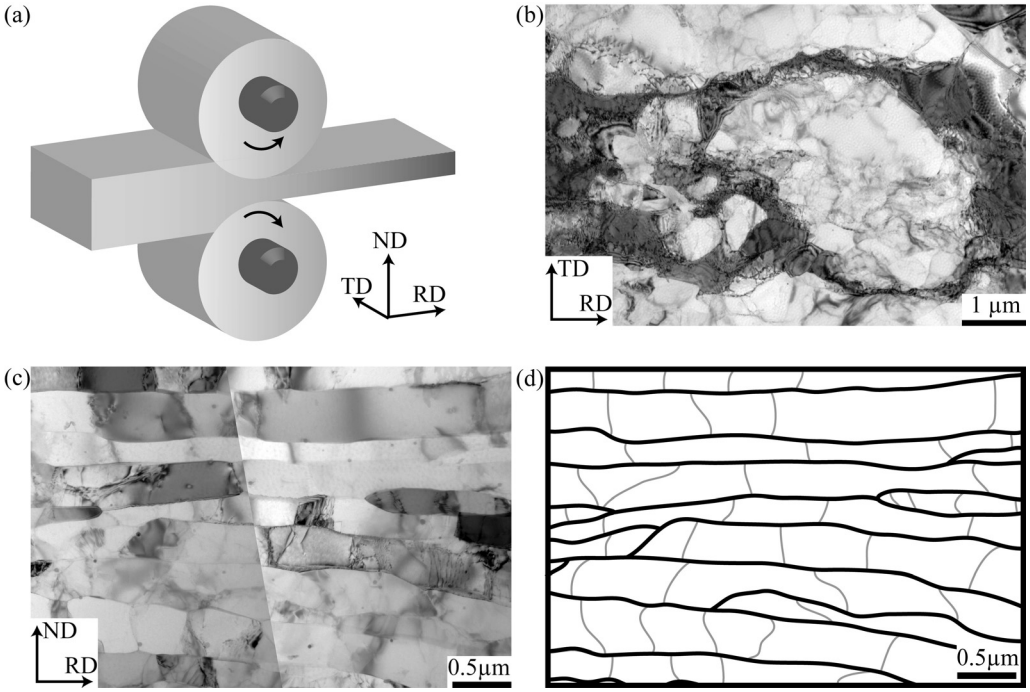

Figure 4.1: (a) A sketch of the rolling geometry, where RD is the rolling direction, ND is the normal direction, and TD is the transverse direction. (b) Subgrain boundary structure in the rolling plane (RD-TD plane) of the strain 5.5 AA1050 aluminium. (c) Lamellar boundary structure in the longitudinal plane (ND-RD plane) of the same sample. (d) A sketch of lamellar boundaries (bold black lines) and interconnecting boundaries (thin grey lines) in (c). Reproduced from Paper IV.

4.2 Triple junctions in a deformed lamellar structure

4.2.1 Classification of triple junctions

This experimental study concentrates on deformation by rolling, which introduces a lamellar microstructure. Figure 4.1a shows a sketch of the rolling geometry, where RD is the rolling direction, ND is the normal direction, and TD is the transverse direction. Figure 4.1b shows a typical equiaxed deformation microstructure in the rolling plane (RD-TD plane) of aluminium cold rolled to a high strain. For the same sample, a very different morphology can be observed in the longitudinal section (ND-RD plane), where a lamellar

structure has evolved (Figure 4.1c). The deformation-induced boundaries can be classified into two categories. One is the lamellar boundary, which is approximately perpendicular to ND; the other is the interconnecting boundary, which is approximately parallel to ND (Figure 4.1c). This classification is based on the morphology but also on the crystallography – lamellar boundaries can be either high angle boundaries (>15°, original grain boundaries and deformation-induced high angle boundaries) or medium-to-low angle dislocation boundaries (<15°), whereas interconnecting boundaries typically are low angle dislocation boundaries. In this material, ~60% of the lamellar boundaries are high angle boundaries, the average lamellar boundary spacing is ~0.24 μm, and the average interconnecting boundary spacing is ~0.78 μm. A similar lamellar boundary structure can be also found in the ND-TD plane. Thus in three dimensions, the lamellar boundaries are lying approximately parallel to the rolling plane, and the interconnecting boundaries are standing approximately perpendicular to the rolling plane. In an idealized lamellar structure the lamellar boundaries are parallel. However, in real structures the structural observations in the present study show that at least three types of junctions must be considered (Figure 4.2):

(a) Y-junctions, each formed by three lamellar boundaries;

(b) H-junction pairs, each formed by two lamellar boundaries and an interconnecting boundary between them; and

(c) r-junctions, each formed by three interconnecting boundaries.

Regarding the morphology of H-junctions, two types are found (Figure 4.3). For the first type, the lamellar boundary is not deflected by the interconnecting boundary (positions A), whereas for the second type (positions B) the lamellar boundary is deflected.

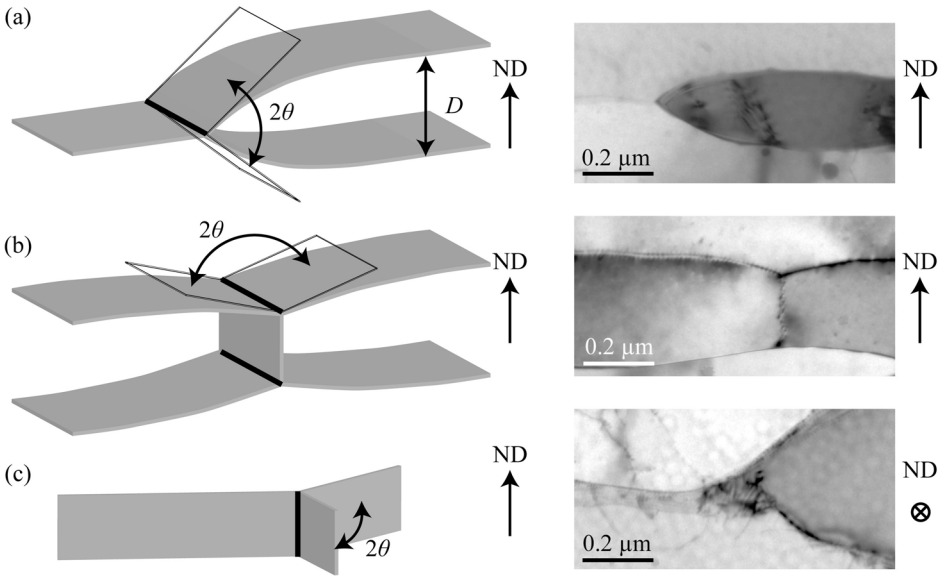

Figure 4.2: Illustrations and examples of three types of triple junctions in a lamellar structure. (a) A Y-junction formed by three lamellar boundaries; (b) two H-junctions (an H-junction pair) formed by two lamellar boundaries and an interconnecting boundary between them; and (c) a random r-junction formed by three interconnecting boundaries. Triple junctions are highlighted in bold lines with dihedral angles 2θ indicated. Both Y-junctions and H-junctions are lying close to the rolling plane, whereas r-junctions are oriented almost parallel to ND. Reproduced from Paper IV.

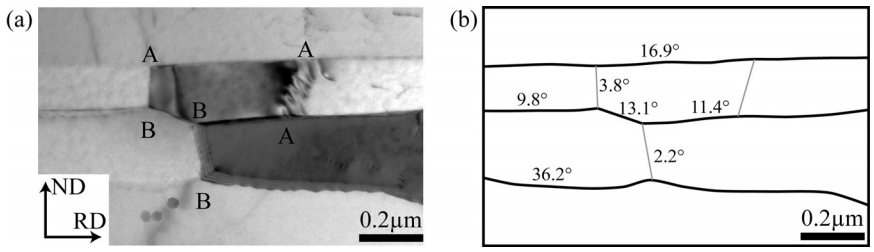

Figure 4.3: (a) A selected area in the longitudinal section of aluminium deformed to a strain of 5.5. Markers A and B indicate two types of H-junctions. (b) Sketch of lamellar boundaries (bold black lines) and interconnecting boundaries (thin grey lines) of the same area. Boundary misorientation angles are indicated above or to the right of each boundary segment. Reproduced from Paper IV.

4.2.2 Triple junction density

An illustration of a lamellar structure is shown in Figure 4.4, and it illustrates that the lamellar boundaries are lying in the rolling plane except where they meet at Y-junctions, forming round, flat volumes (pancake shapes); all the interconnecting boundaries are standing perpendicular to the rolling plane, forming pancake-shaped cells. The density of Y-junctions in a two-dimensional section (number per unit area) can be determined by direct counting and dividing by the area. If the Y-junction density in the longitudinal section is ρ_{Y}^{NDRD}, the Y-junction density expressed as length per unit volume is then:

$$\rho_{\mathrm{Y}} = \frac{\pi}{2}\rho_{\mathrm{Y}}^{NDRD}, \tag{4.1}$$

since Y-junctions are confined in the rolling plane but inclined randomly with respect to RD, e.g. $\rho_{\mathrm{Y}}^{NDRD} / \rho_{\mathrm{Y}} = (1/\pi)\int_0^{\pi} \sin\varphi d\varphi = 2/\pi$, where φ is the inclination angle. This ratio, $2/\pi$, is lower than 1 but higher than 1/2, where 1 corresponds to the case that all junctions are perpendicular to the observation plane and 1/2 corresponds to the case that all junctions orient completely randomly in three dimensions (Baddeley and Jensen 2005). Similarly, the H-junction density (length per unit volume) is:

$$\rho_{\mathrm{H}} = \frac{\pi}{2}\rho_{\mathrm{H}}^{NDRD}, \tag{4.2}$$

where ρ_{H}^{NDRD} is the number of H-junctions per unit area counted in the longitudinal plane. In the case of r-junctions, which are parallel to ND, the r-junction density (length per unit volume) is:

$$\rho_{\mathrm{r}} = \rho_{\mathrm{r}}^{RDTD}, \tag{4.3}$$

where ρ_{r}^{RDTD} is the number of r-junctions per unit area in the rolling plane.

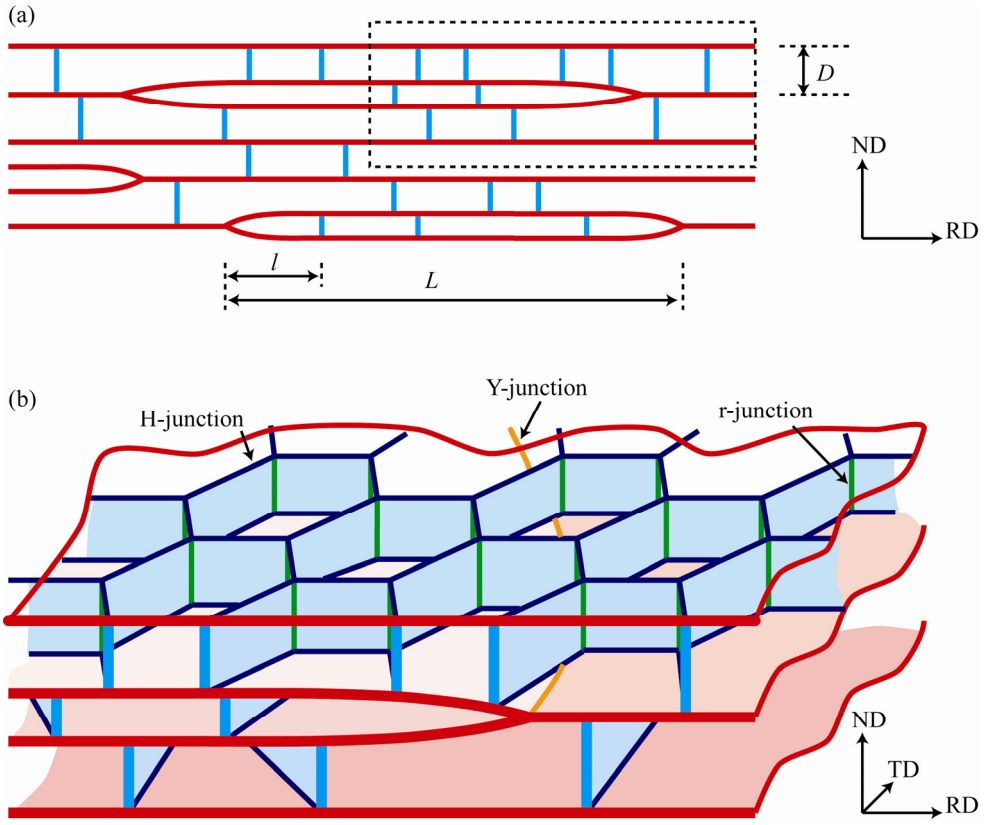

Figure 4.4: (a) An illustration of a lamellar boundary structure in the longitudinal section, where the lamellar boundary (red) spacing is D, the interconnecting boundary (cyan) spacing is l (the lamella ends are also included for this measurement), and the lamella length is L. (b) An illustration of the three-dimensional boundary structure of the marked region in (a). Lamellar boundaries are shown in different shades of red, with the top layer transparent, and interconnecting boundaries are shown in cyan. One Y-junction is shown in orange; all H-junctions are shown in blue; and all r-junctions are shown in green. Bold red and cyan lines represent boundaries intersecting the ND-RD plane. Reproduced from Paper IV.

Direct counting is a straightforward way to determine the triple junction density. However, the triple junction density can also be derived from the boundary spacings in a two dimensional section. In the case of Y-junctions since each lamella contributes two Y-junctions, it follows that $\rho_Y^{NDRD} = 2/(DL)$, where D is the lamella spacing and L is the lamella length measured in the longitudinal plane (a large map is required for measuring L). Therefore by incorporating Equation (4.1) the Y-junction density can be expressed as:

$$\rho_{\mathrm{Y}} = \frac{\pi}{DL}. \tag{4.4}$$

Similarly, if the cell length l (the interconnecting boundary spacing) in the longitudinal plane is measured, the density of H-junctions can be calculated as:

$$\rho_{\mathrm{H}} = \frac{\pi}{Dl}(1-\frac{l}{L}). \tag{4.5}$$

In the case of r-junctions, the density will depend on the detailed morphology of the interconnecting boundaries. If we assume in the rolling plane that all r-junctions are within the central region of each lamella with a diameter 2(R-r), where 2R is the diameter of the lamella and 2r is the diameter of the cell, and $R = 2L/\pi$ and $r = 2l/\pi$ due to their pancake shape, then the r-junction density is:

$$\rho_{\mathrm{r}} = \frac{\pi}{2l^2}(1-\frac{l}{L})^2. \tag{4.6}$$

It follows that the densities of triple junctions can be either determined by direct counting or estimated from by measuring the lamella spacing D, the lamella length L, and the interconnecting boundary spacing l, in the longitudinal section (Figure 4.4a). These equations also predict that the triple junction density increases with decreasing boundary spacing. However, for very short lamellae containing no interconnecting boundaries (l=L), there will be no H-junctions and r-junctions within the lamella. This method can easily be adopted and an example is chosen, where the boundary spacings of pure nickel at different rolling reductions have been measured by Hughes and Hansen (2000). The corresponding triple junction density is calculated according to Equations (2.4) to (4.6), and it is found that the density of all three types of triple junctions increases with increasing strain with the H-junction density being the highest (Figure 4.5).

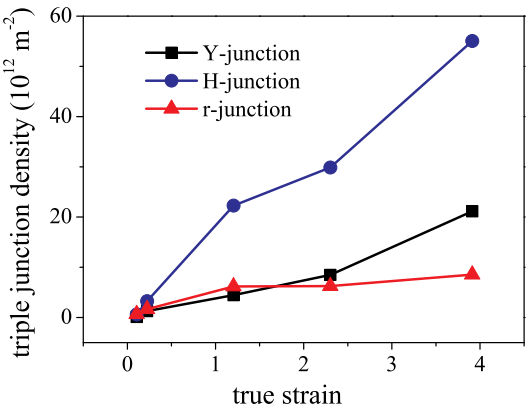

Figure 4.5: Triple junction density in pure nickel deformed by cold rolling to various strains. The calculation is based on boundary spacings reported by Hughes and Hansen (2000).

4.2.3 Structural parameters

Triple junctions are generally assumed not to drag the boundary motion during grain growth, and their role is reduced to preserve the thermodynamically described equilibrium angles at the lines where boundaries meet (von Neumann 1952; Mullins 1956). The underlying assumption is that the triple junction has a practically infinite mobility. However, triple junction drag was first considered by Galina *et al.* (1987) and then observed by Czubayko *et al.* (1998) in zinc and by Protasova *et al.* (2001) in aluminium during boundary migration in tricrystals above the recrystallization temperature. More recently, Gottstein *et al.* (2010) have derived a kinetic equation of grain growth taking both triple junction drag (finite mobility) and triple junction energy into consideration. An important parameter here is the dihedral angle, which together with the boundary energies, determines the grain boundary surface tension (N/m) on triple junctions. In these earlier studies ideal samples have been considered. However, deformed structures are complex as a high density of dislocations and a high stored energy are present. As to the choice of key parameters, the following are considered: the spacing between and the misorientation angle

across different types of boundaries, and the dihedral angle between the boundaries forming the triple junction.

4.3 Experimental details

Commercial purity aluminium AA1050 cold rolled to true strains 2, 4, and 5.5 is used (see Section 3.1), and focus is on aluminium deformed to the highest strain with the highest stored energy. In order to separate recovery from recrystallization and also to study the progression of recovery, low and medium isothermal annealing temperatures (from room temperature to 220°C) have been chosen. Both TEM and EBSD have been applied. Since both techniques are two-dimensional characterization techniques, an appropriate observation section has to be selected. Here all the characterizations have been carried out in the longitudinal section (ND-RD plane). Therefore all lamellar boundaries are viewed approximately edge-on, facilitating the characterization of Y-junctions and H-junctions.

Table 4.1: Choice of sample and annealing temperature for *ex situ* TEM and EBSD observations.

	TEM			EBSD		
True strain	RT*	120°C	220°C	RT*	120°C	220°C
2					√	
4					√	
5.5	√	√	√	√	√	√

*RT stands for room temperature, which is about 20°C, and samples used for RT annealing were stored in a freezer after cold rolling.

In order to follow the triple junction motion during recovery annealing, *ex situ* TEM observations were carried out, and the accumulated annealing time has been 62 days, 10 hours and 1 hour for annealing at room temperature, 120°C and 220°C, respectively (Table 4.1). Moreover, *ex situ* EBSD

observations were carried out for all three strains in order to follow the triple junction motion during annealing in bulk specimens (Table 4.1).

The microstructural evolution characterized by *ex situ* observations may be affected by the presence of the sample surface (one surface in EBSD samples and two surfaces in TEM foils). Although thermal grooving is not pronounced at these low temperatures (Ivanov *et al.* 2004), the presence of a surface may still relax the structure near the surface, reducing the driving pressure for annealing processes. Conventional post mortem EBSD examinations in the sample interior were therefore carried out for the strain 5.5 aluminium sample annealed at 220°C in order to compare the bulk and the surface annealing behaviour.

In the following, a direct method based on counting was adopted to determine the triple junction density. Most measurements of boundary spacing and triple junction density were carried out manually from TEM images (measurements for strains 2 and 4 were based on micrographs of AA1200 aluminium) or EBSD orientation maps, except for EBSD measurement of lamellar boundary spacings (see Section 3.4). Due to limited angular resolution of the EBSD technique, the interconnecting boundary spacing and the H-junction density were determined from TEM images.

4.4 Results

4.4.1 Microstructural parameters in the deformed state

Table 4.2 shows that the average boundary spacing both between lamellar boundaries and between interconnecting boundaries decreased with increasing strain, but the aspect ratio (l/D) was only slightly changed. The TEM data for strains 2 and 4 were measured from aluminium AA1200 (99.1% purity), i.e. with a slightly lower purity than AA1050 in the present study, but for both materials the parameters were comparable to previous

studies of rolled aluminium (e.g. Liu *et al.* 2002; Mishin *et al.* 2010). By direct counting and applying Equations (4.1) and (4.2), the Y-junction density and H-junction density were found to increase with decreasing boundary spacing. The H-junction density was much higher than the Y-junction density, which is consistent with Equations (4.4) and (4.5), since the lamella length L is much larger than the cell length l (the interconnecting boundary spacing). EBSD measurements generally agreed with TEM measurements. The density of r-junctions was not measured directly in the present study. However, by combining Equations (4.4) and (4.6), the r-junction density ρ_r can be calculated as D, l and ρ_Y were known. The calculated r-junction density also increased with increasing strain as with ρ_Y and ρ_H (Figure 4.6), showing similarities between aluminium and nickel (see Figure 4.5) when cold rolled. However a much coarser structure is present in aluminium due to more intrinsic dynamic recovery during rolling.

Table 4.2: The average values (with standard errors) of the lamellar boundary spacing (D), interconnecting boundary spacing (l), and triple junction density for commercial purity aluminium at different strains.

	TEM*				EBSD	
True strain	D (μm)	l (μm)	ρ_Y (10^{12} m^{-2})	ρ_H (10^{12} m^{-2})	D (μm)	ρ_Y (10^{12} m^{-2})
2	0.42±0.02	1.30±0.12	1.26±0.09	4.4±0.4	0.37±0.01	1.60±0.24
4	0.29±0.02	0.85±0.06	1.78±0.08	11.6±0.6	0.28±0.01	2.45±0.17
5.5	0.23±0.01	0.78±0.04	2.43±0.10	14.5±0.6	0.24±0.01	3.08±0.11

*TEM measurements for strains 2 and 4 were based on micrographs of AA1200 aluminium (99.1% purity) from a previous study (Huang *et al.* 2006b).

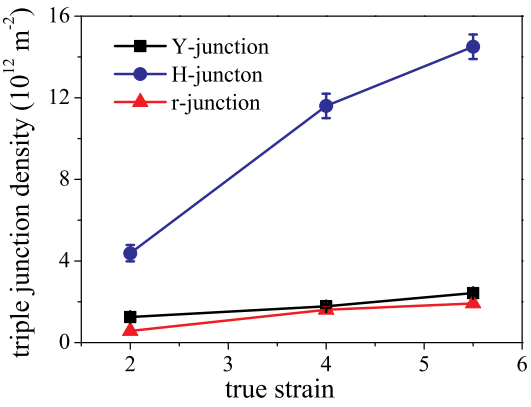

Figure 4.6: TEM measurements of triple junction density in AA1200 (strains 2 and 4) and AA1050 (strain 5.5) aluminium. Error bars for Y-junction densities are smaller than the symbols used.

4.4.2 TEM observations of triple junction motion

Ex situ TEM observations were carried out for samples deformed to a strain of 5.5 and annealed at 120°C. One selected area in the deformed state is shown in Figure 4.7a. After one hour at 120°C, most of the boundaries have not changed their positions since the TEM micrographs taken before and after annealing match very well. However, local changes near Y-junctions were found as illustrated in Figure 4.7b. This structural evolution can be described phenomenologically as a migration of Y-junctions. Following this Y-junction migration, the lamellar boundaries involved consequently migrated laterally. In this area, 14% of Y-junctions migrated different distances, causing either shortening or removal of lamellae and local widening of neighbouring lamellae. This Y-junction migration caused the average boundary spacing to increase about 1.5% after annealing at 120°C for one hour.

With longer annealing times, more Y-junctions migrated and they migrated over longer distances, indicating a time effect. Figure 4.8a shows an example of a migrating Y-junction. It migrated rapidly in the beginning (~0.72 µm in one hour) before it became pinned by an H-junction (Y-H

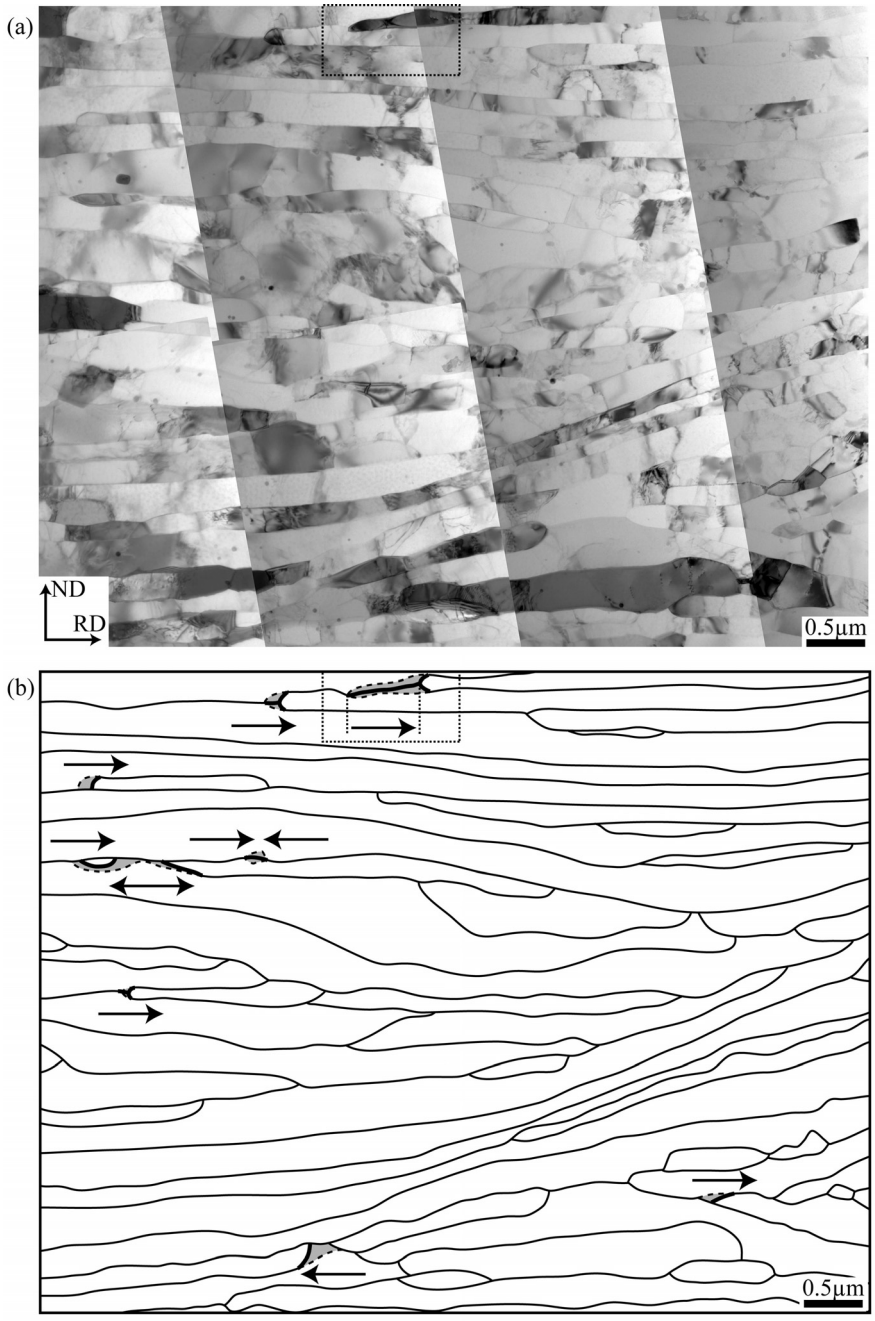

Figure 4.7: (a) A TEM micrograph montage of a selected area in the longitudinal section of aluminium deformed to a strain of 5.5. (b) A sketch of the same area combining the deformed state and the state after annealing at 120°C for one hour. Solid thin lines represent lamellar boundaries which are unchanged; dashed lines represent boundaries which have migrated with new positions represented by solid bold lines. The areas swept by migrating boundaries are shown in grey, and the directions of the Y-junction motion are indicated by arrows. An area is marked showing pronounced Y-junction motion. Reproduced from Paper IV.

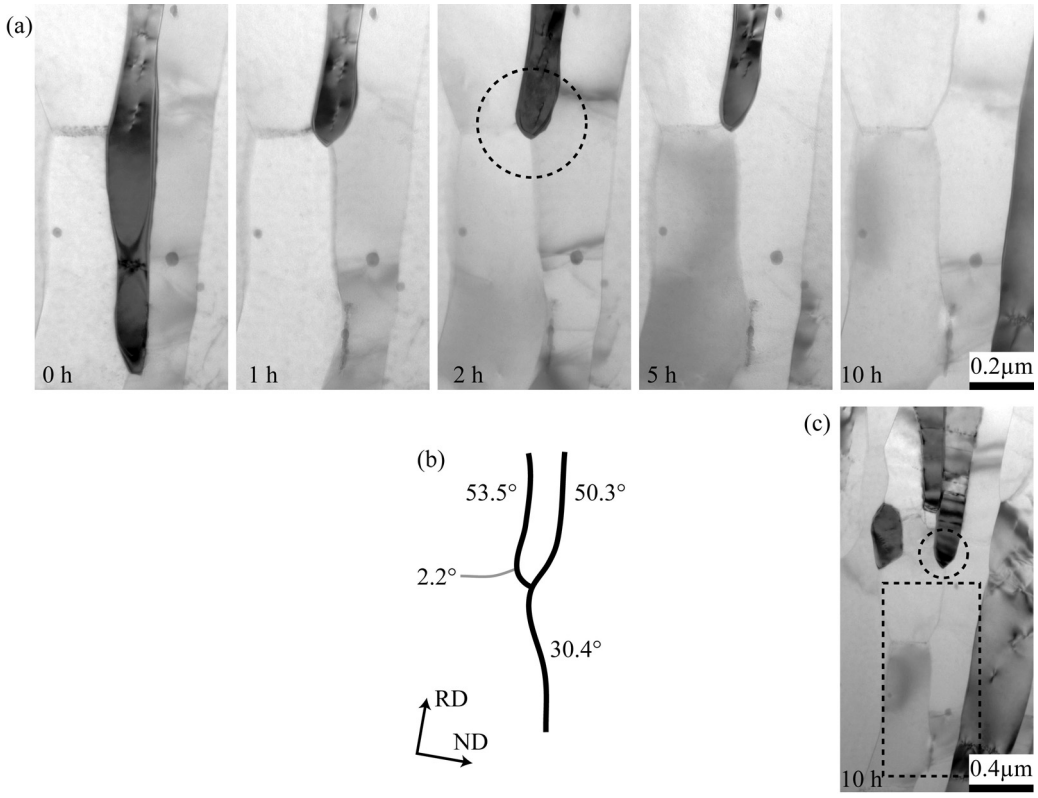

Figure 4.8: *Ex situ* TEM observations of Y-junction motion in the longitudinal section of aluminium deformed to a strain of 5.5 and annealed at 120°C. (a) Positions of the Y-junction before and after annealing for 1, 2, 5, and 10 hours. The marked region shows pinning by an H-junction and it is sketched in (b) with boundary misorientation angles indicated. (c) The final position of the Y-junction (marked by a circle) after 10 hours annealing, where the rectangular marked region corresponds to the region in (a). Reproduced from Paper IV.

pinning, Figure 4.8b). With further annealing for up to five hours, little change occurred in the position of the triple junction. After annealing for ten hours, the junction escaped from the pinning and arrived at the position shown in Figure 4.8c. Another example is shown in Figure 4.9a, where the shortening lamella has a bright contrast. In this case, the migrating Y-junction was initially pinned by an H-junction (Figure 4.9b), but it escaped after annealing for five hours. However, in the final position shown in Figure 4.9c, the Y-junction was pinned by a neighbouring Y-junction (Y-Y pinning, Figure 4.9d).

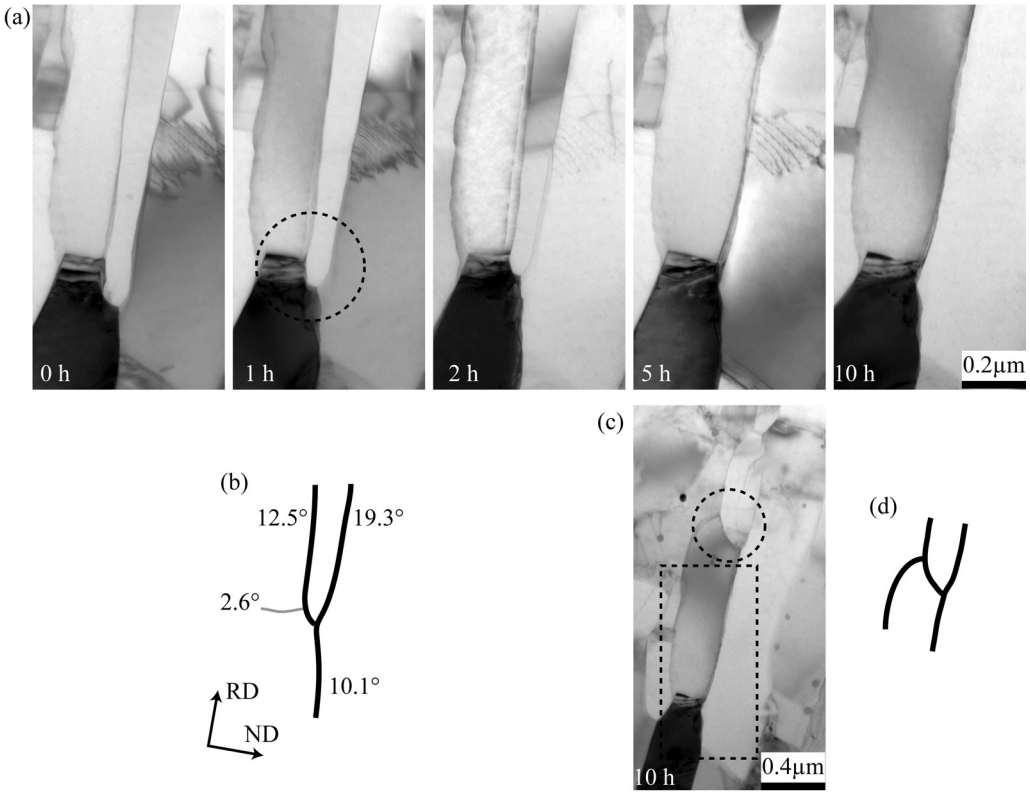

Figure 4.9: *Ex situ* TEM observations of Y-junction motion in the longitudinal section of aluminium deformed to a strain of 5.5 and annealed at 120°C. (a) Positions of the Y-junction before and after annealing for 1, 2, 5, and 10 hours. The marked region shows pinning by an H-junction, which is sketched in (b) with boundary misorientation angles indicated. (c) The final position of the Y-junction (marked by a circle) after 10 hours annealing. The rectangular marked region corresponds to the region in (a), and the circular marked region shows pinning by a neighbouring Y-junction, which is sketched in (d). Reproduced from Paper IV.

Y-junction migration was also studied by *ex situ* TEM observations of samples which were originally stored in the freezer and then kept at room temperature for different time intervals. An example is shown in Figure 4.10. The Y-junction migrated downwards until it was pinned by a particle. However, as expected Y-junction motion was much less frequently observed at room temperature than at 120°C.

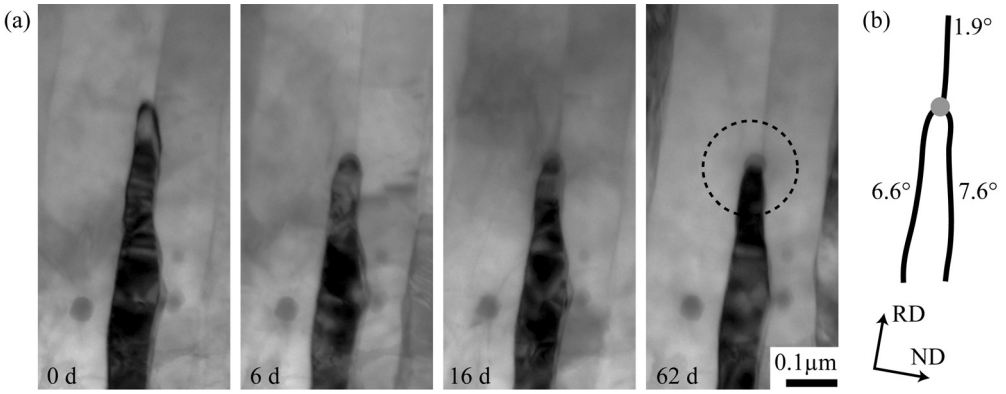

Figure 4.10: *Ex situ* TEM observations of Y-junction motion in the longitudinal section of aluminium deformed to a strain of 5.5 and kept at room temperature for 6, 16 and 62 days. (a) Positions of the Y-junction. The marked region shows pinning by a particle, and it is sketched in (b) with boundary misorientation angles indicated. Reproduced from Paper IV.

Y-junction motion at 220°C was found to be much more frequent than at 120°C, illustrating a strong temperature effect. An example is shown in Figure 4.11, where significant Y-junction motion took place in an initially finely-spaced region, leading to doubling of the lamella spacing locally after annealing for one hour. The microstructure during annealing evolved into being more equiaxed, but it kept a clear lamellar morphology.

Y-H pinning was found to be very common (e.g. Figure 4.8), whereas Y-Y pinning was less frequent. Misorientation angle measurements were used in some cases in order to distinguish between the two types. Figure 4.12a shows an area containing both types of pinning. Y-H pinning can be recognized when neighbouring H-junctions and Y-junctions were identified. Y-Y pinning at site "A" can be easily determined from its morphology; however at sites "B" it may be difficult to determine whether they are H-junction pairs or Y-junction pairs. However boundary misorientation measurements (Figure 4.12b) show that sites "B" are also examples of Y-Y pinning. In addition, particles of different sizes may also pin the Y-junction motion (Figure 4.10), although observations of such an effect were infrequent compared to pinning by neighbouring boundaries.

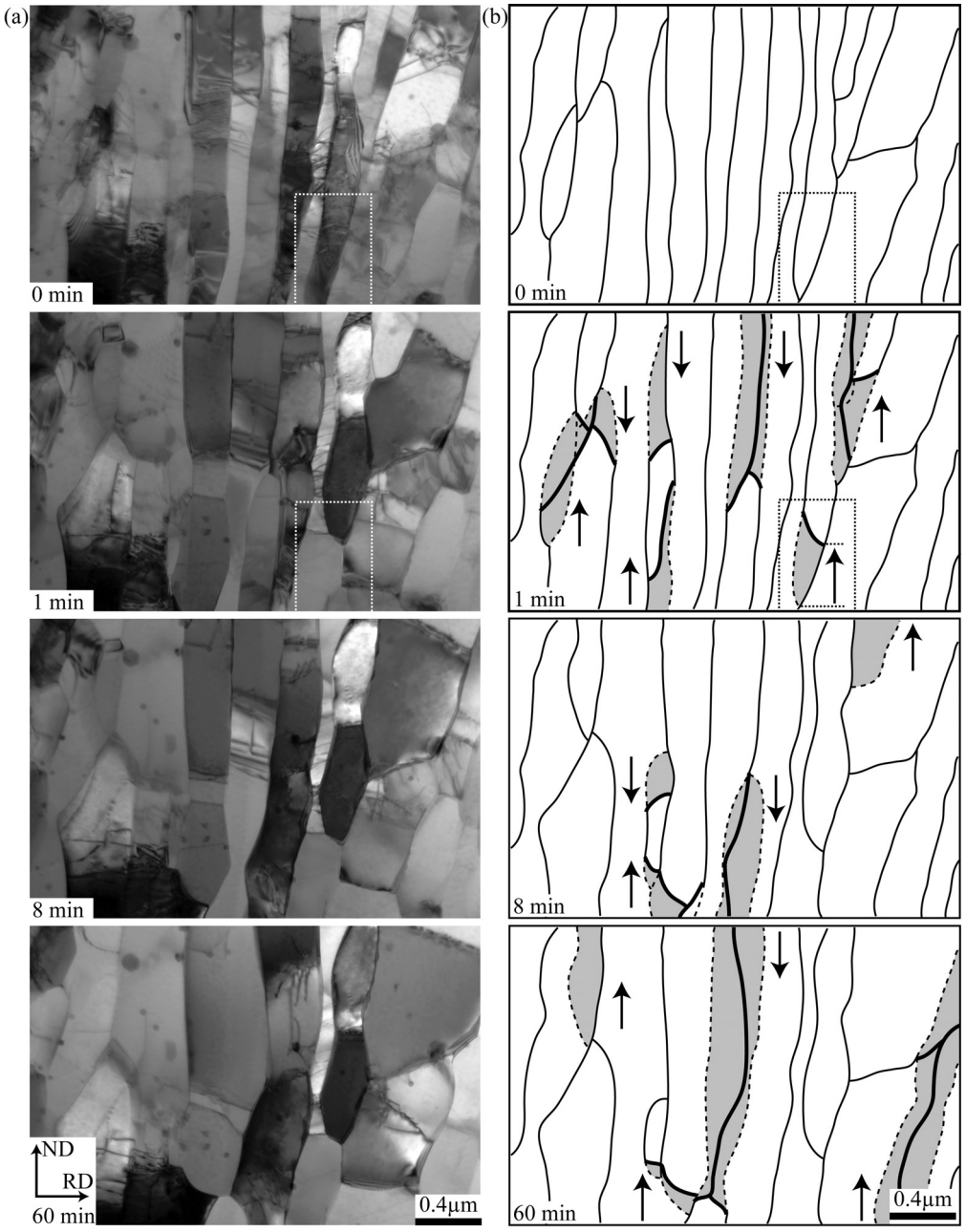

Figure 4.11: *Ex situ* TEM observations of Y-junction motion in the longitudinal section of aluminium deformed to a strain of 5.5 and annealed at 220°C. (a) Microstructure of the same area before and after annealing for 1, 8, and 60 minutes. (b) Sketches of the same area at different states corresponding to (a). For the states after annealing, each sketch combines the current state with the previous state to show the structural evolution, with the same markings as in Figure 4.7. The arrows indicate the directions of Y-junction motion and are further illustrated in the marked areas in (a) and (b). Reproduced from Paper IV.

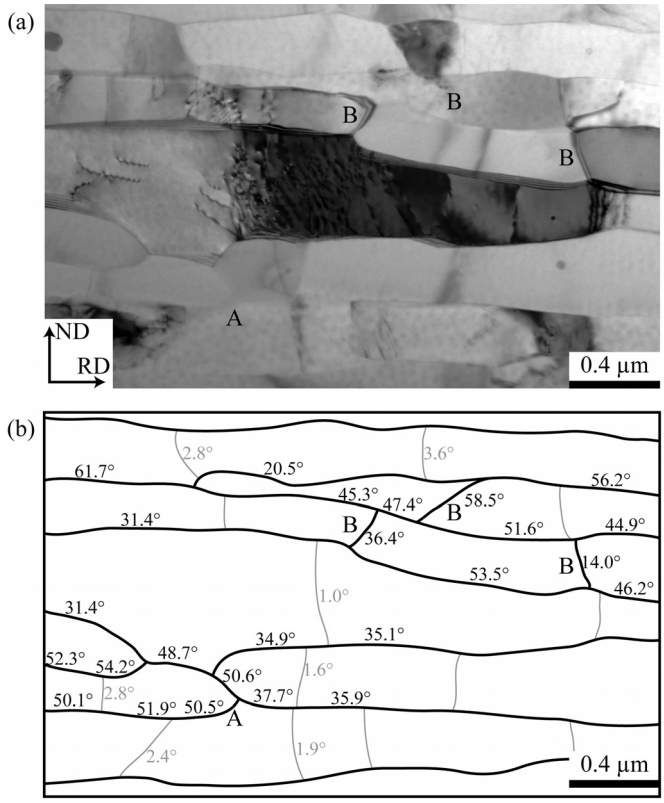

Figure 4.12: (a) A selected area in the longitudinal section of aluminium deformed to a strain of 5.5 and annealed at 120°C for 10 hours. (b) Sketch of lamellar boundaries (bold black lines) and interconnecting boundaries (thin grey lines) of the same area. Boundary misorientations are indicated above or to the right side of each boundary segment. The markers "A" and "B" indicate sites where two Y-junctions pin each other. Reproduced from Paper IV.

The Y-junction motion caused shortening and finally removal of a specific lamella, followed by widening of the neighbouring lamellae. This Y-junction motion reduced the area of lamellar boundaries per unit volume and increased the average lamellar boundary spacing. Furthermore, this Y-junction motion also removed interconnecting boundaries within the disappearing lamellae and extended the interconnecting boundaries within the neighbouring lamellae. An example is shown in Figure 4.8, where the interconnecting boundary on the left side was extended after removal of the dark lamella in the middle. It follows that H-junctions and r-junctions within disappearing lamellae also disappear. However, H-junctions within neighbouring lamellae

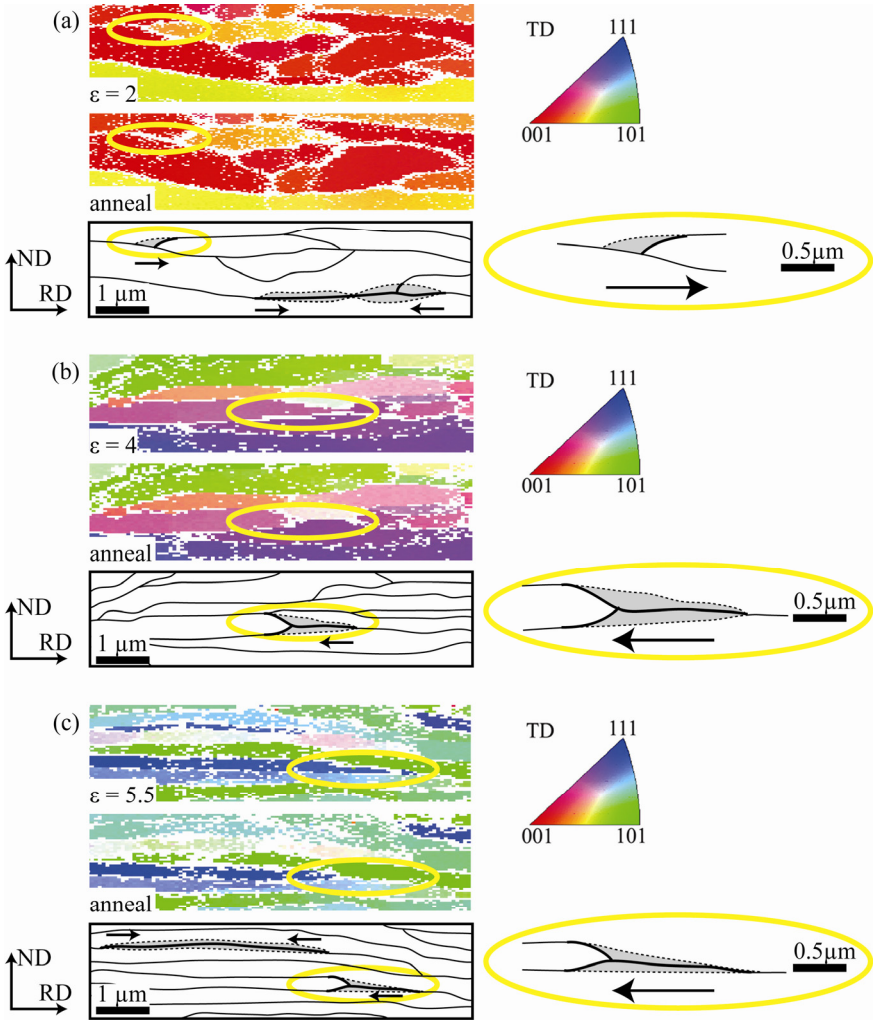

Figure 4.13: Examples of Y-junction motion in the longitudinal section (ND-RD plane) of aluminium deformed to strains (a) 2, (b) 4, and (c) 5.5 and annealed at 120°C for 5 hours. The maps, both for the deformed state and annealed state, are coloured according to the orientation of TD for each pixel (colour coding is shown by the triangle), and the white pixels correspond to not-indexed points in the raw EBSD data and are mainly distributed along boundaries. The sketches follow the same markings as in Figure 4.7 and marked areas are magnified in these sketches. Reproduced from Paper IV.

may change characteristics and an example is shown in Figure 4.8, where the pinning H-junction initially connected to a lamellar boundary with a misorientation angle of 53.5° was replaced by a lamellar boundary of misorientation angle 30.4° after disappearance of the middle dark lamella.

All the above observations were carried out in well-polished and relatively thick areas (~0.3 μm). However, in those over-etched regions, where

grooving is significant and thickness is not uniform, the boundary structure showed little change even after annealing at 220°C for one hour. These results are therefore considered as resulted from the special structure introduced by over-etching and not representative of the bulk material.

4.4.3 EBSD observations of triple junction motion

Y-junction motion observed during *ex situ* EBSD experiments at the three strain levels and at an annealing temperature of 120°C is shown in Figure 4.13. The motion of the Y-junctions gave rise to either shortening or removal of lamellae, resulting in widening of neighbouring lamellae. *Ex situ* EBSD maps showed that the Y-junction motion was always associated with finely-spaced lamellae and that the rate of Y-junction motion increased with increasing strain (the example shown in Figure 4.13a is rare whereas that in Figure 4.13c is frequent), indicating an effect of strain. The present deformation structures were subdivided into typical rolling texture components, and Y-junction motion was examined for each rolling texture component but no significant orientation preference was found.

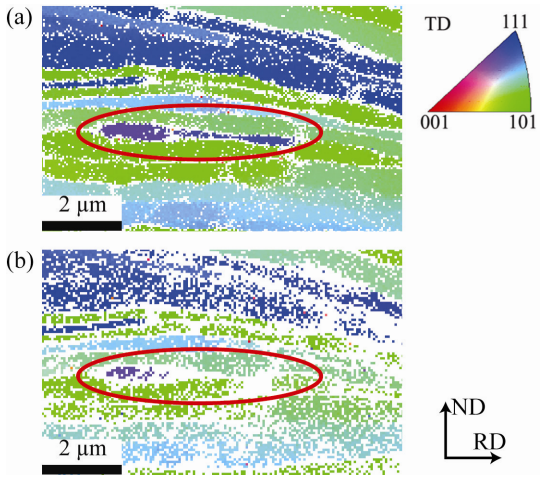

Figure 4.14: Examples of Y-junction motion (in the marked area) in the longitudinal section (ND-RD plane) of aluminium deformed to a strain of 5.5 and annealed at room temperature for one year. The colours are coded according to the orientation of each pixel for both images. (a) The deformed state; (b) the annealed state.

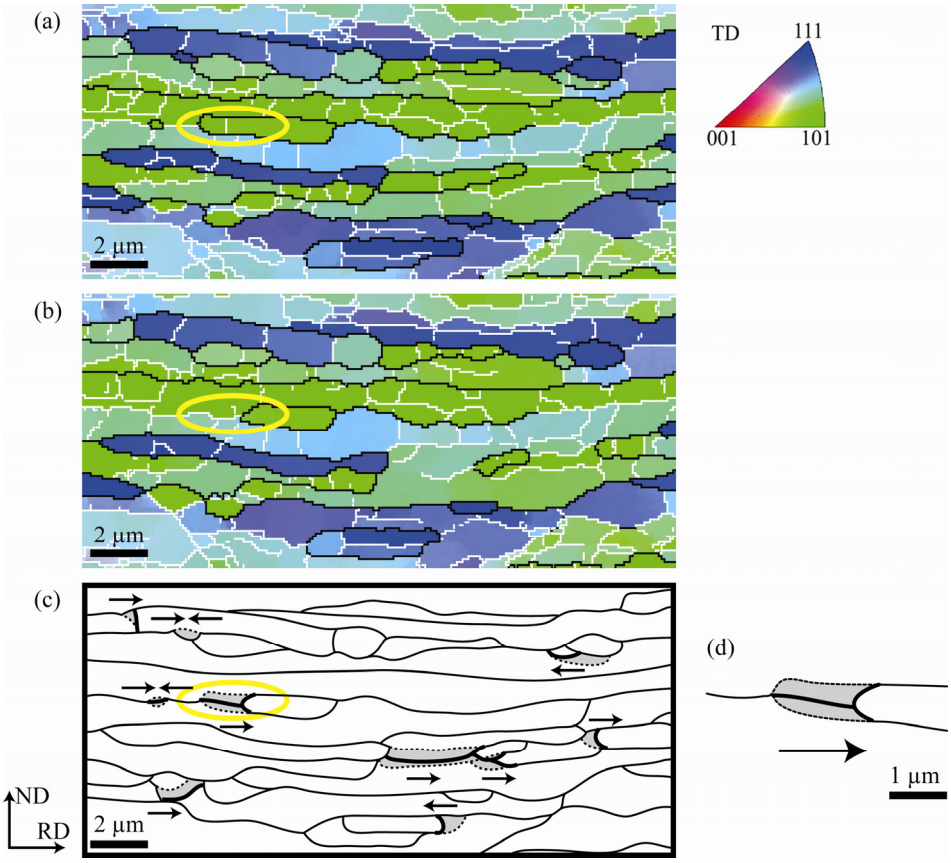

Figure 4.15: Examples of Y-junction motion in the longitudinal section (ND-RD plane) of aluminium deformed to a strain of 5.5 and annealed at 220°C. (a) Annealed for 2 hours; (b) annealed for 4 hours accumulatively. The colours are coded according to the orientation of each pixel after data cleaning. High angle boundaries (>15°) are shown in black and low angle boundaries (1.5~15°) in white. (c) A sketch of the lamellar boundaries combining the two states, following the same markings as in Figure 4.7. The marked region is magnified in (d).

Y-junction motion at room temperature was also observed by *ex situ* EBSD, and one example is shown in Figure 4.14. However, even after one year's exposure at room temperature, only limited Y-junction motion was found, in agreement with the TEM observations. Also consistent with the TEM observations, significant Y-junction motion was observed by *ex situ* EBSD in samples annealed at 220°C. One example is shown in Figure 4.15, where only the later stage (starting from a two-hour annealed state) is presented for clarity.

4.4.4 Microstructural parameters in the recovered state

Most of the migrating Y-junctions were composed of three high angle boundaries (e.g. Figure 4.8b) or a combination of high angle boundaries and medium-to-low angle boundaries (e.g. Figure 4.9b), but cases of migrating Y-junctions formed by three medium-to-low angle boundaries (e.g. Figure 4.10b) were also found although much less frequently. A similar trend in frequency was also found for the not-migrating Y-junctions; however it is still not clear whether an effect of boundary misorientation angle on the Y-junction motion is significant.

In addition to structural parameters such as spacing between and misorientation angles across lamellar and interconnecting boundaries, the triple junctions were characterized by their dihedral angles. The dihedral angles 2θ, as shown in Figure 4.2a, of Y-junctions were measured using TEM by aligning the Y-junction line parallel to the electron beam. Measurements showed that these angles were generally between ~40° and ~120° for aluminium deformed to a strain of 5.5. As an approximation, the dihedral angle of Y-junctions may also be estimated from TEM micrographs (e.g. Figure 4.7a), and the two methods give similar results. The dihedral angle and lamellar boundary spacing shown in Figure 4.16 were measured from TEM micrographs of deformed samples, and the categorization into two groups was based on the annealing results – circles for not-migrated Y-junctions and dots for migrated ones. The plot shows that: (i) the estimated dihedral angle appeared to increase with increasing lamella spacing although an exact value must depend on the local configuration (e.g. affected by neighbouring H-junctions); (ii) a migrating Y-junction generally had a small dihedral angle and the corresponding shortening lamella generally had a small spacing; and (iii) neither a lamella spacing below ~50 nm nor a dihedral angle below ~30° was observed. However, the large dispersion of data shown in Figure 4.16 indicates that other factors may also play a role in determining the stability of a Y-junction.

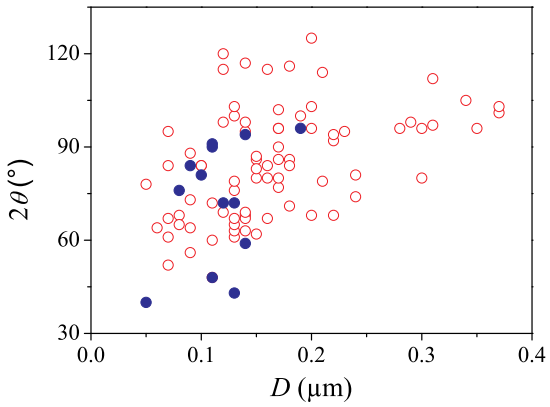

Figure 4.16: Dependence of the dihedral angle on the lamella spacing of Y-junctions in aluminium deformed to a strain of 5.5. The dihedral angles were estimated from TEM micrographs taken from the longitudinal section and the lamella spacing was measured near the same Y-junction. Open circles represent random measurements, whereas solid points represent measurements of Y-junctions observed to have migrated after annealing at 120°C for 5 hours.

Figure 4.17 shows the evolution of the lamellar boundary spacing (noted as "spacing in interior") and the Y-junction density after isothermal annealing at 220°C for the strain 5.5 aluminium. The lamellar boundary spacing increased with increasing annealing time, whereas the Y-junction density decreased during annealing. The same trend for the lamellar boundary spacing evolution was also found in the *ex situ* EBSD observations, i.e. changes of the spacing on a polished sample surface in the longitudinal plane (noted as "spacing at surface" in Figure 4.17). The coarsening at the surface was only slightly slower compared to that in the sample interior, and it is concluded that the *ex situ* EBSD observations, which are consistent with *ex situ* TEM observations, appear to be representative of the bulk behaviour.

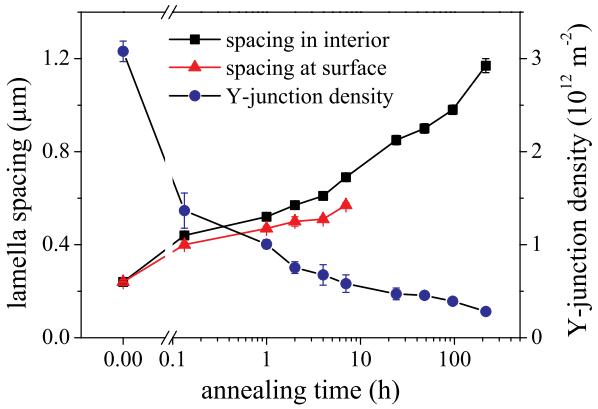

Figure 4.17: Evolution of the lamellar boundary spacing (both in the sample interior and at the surface) and the Y-junction density during isothermal annealing at 220°C for AA1050 aluminium deformed to a strain of 5.5.

4.5 Discussion

The recovery behaviour in aluminium deformed to large strains has been examined thoroughly by Furu *et al.* (1995) and Nes (1995), who analyzed mechanisms such as climb, glide, and annihilation of dislocations. Kinetic studies have also been carried out by Vandermeer and Hansen (2008). The general findings are:

(i) A lamellar structure coarsens during recovery and evolves towards a more equiaxed morphology.

(ii) The recovery rate is high and increases with increasing strain and annealing temperature.

(iii) The apparent activation energy increases as recovery proceeds.

Within this frame, recovery by triple junction motion is discussed based on the present findings, which show that: (i) the rate of triple junction motion increases with the strain; (ii) this mechanism operates in the temperature interval from room temperature to 220°C; and (iii) its dependency on

annealing time and temperature indicates that it is a thermally-activated process.

4.5.1 Triple junction motion

In well-annealed polycrystals, local equilibrium of grain boundaries at a triple junction is generally assumed and in the case of high angle boundaries a dihedral angle of 120° is expected if the energy of the connecting boundaries is independent of the boundary misorientation angle. However, dihedral angles of 120° are not representative of the deformed lamellar structure as illustrated above. Considering for example Y-junctions, most of the boundaries are medium-to-high angle boundaries and have boundary energies of the same order (Read and Shockley 1950). As equilibrium (neglecting torque terms) can be expressed as follows (Herring 1951; King 2010):

$$\frac{\gamma_1}{\sin(2\theta_1)} = \frac{\gamma_2}{\sin(2\theta_2)} = \frac{\gamma_3}{\sin(2\theta_3)}, \tag{4.7}$$

where $2\theta_i$ (i = 1, 2, 3) is the dihedral angle between two boundaries and γ_i (i = 1, 2, 3) is the energy (J/m^2) of the third boundary in the junction, it is apparent that the junctions in the deformed structure are not in equilibrium. It follows that there is a grain boundary surface tension (N/m) exerted on the triple junction. For the simplest case of a symmetric Y-junction (Figure 4.2a) assuming a constant boundary energy (γ), the grain boundary surface tension (σ) for the motion of the Y-junction can be expressed as:

$$\sigma = (2\cos\theta - 1)\bullet\gamma\,. \tag{4.8}$$

With dihedral angles varying in the range ~40° to 120° the grain boundary surface tension will decrease with increasing dihedral angle as shown in Figure 4.18.

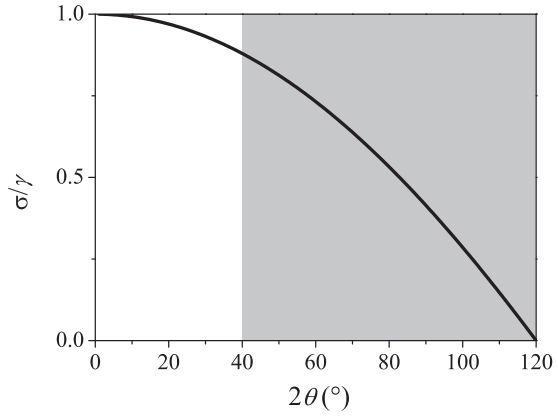

Figure 4.18: Normalized grain boundary surface tension as a function of the dihedral angle at a Y-junction. The shaded region corresponds to the experimentally observed range of dihedral angles.

Figure 4.16 shows that the dihedral angle generally decreases with decreasing lamella spacing in the deformed state, and it follows from Figure 4.18 that the grain boundary surface tension for Y-junction motion increases with decreasing lamella spacing. With increasing strain during plastic deformation, the lamellar boundary spacing decreases (Hughes and Hansen 2000; Liu *et al.* 2002), therefore increasing the grain boundary surface tension for Y-junction motion and decreasing the stability of the deformation microstructure. The present observations and analyses generally agree with the model suggested by Galina *et al.* (1987), where the triple junction velocity is assumed to be proportional to the grain boundary surface tension at a given temperature and the grain boundary surface tension increases as a function of dihedral angle and spacing. However, some observations here are not in direct support of the model. For example, the model cannot explain the absence of dihedral angles below 30° or lamellae thinner than 50 nm although the grain boundary surface tension is still the same order of magnitude (Figure 4.18). This leads to the tentative suggestions that not only the grain boundary surface tension but also the triple junction mobility may depend on its dihedral angle, being very large for a sharp triple junction; or an internal stress may build up at sharp triple junctions during deformation, leading to stress-induced triple junction motion and removal of very thin lamellae.

Besides a reduction of the boundary energy, there may be other causes for the Y-junction motion. Strain energy from dislocations may contribute to the driving pressure since there may be a difference in dislocation density within different lamellae, although this contribution may not be so significant since the stored energy from these loose dislocations is estimated to be much lower than the contribution from the boundary energy (Godfrey and Liu 2009). Moreover in the bulk interior, Y-junction lines form loops (connected by quadruple points). Since Y-junctions are one-dimensional defects similar to dislocations, they have a line energy (J/m) (Zhao *et al.* 2010). In order to minimize this energy, a Y-junction loop is inclined to shrink, consequently removing the confined lamella. However, if the triple junction line energy in a deformed sample equals that in a fully-annealed sample, then its contribution to the total stored energy may be not significant (Gottstein *et al.* 2010) in the present structure.

For the H-junctions between lamellar and interconnecting boundaries, they combine boundaries with misorientation angles (and energies) which are significantly different. Due to the low energy and low mobility of interconnecting boundaries, H-junctions should be more stable than Y-junctions, which is observed. The stability of r-junctions has not been examined but their behaviour may be close to H-junctions as r-junctions connect only low angle boundaries. Therefore in the following only the motion of Y-junctions will be considered.

4.5.2 A recovery mechanism based on Y-junction motion

An important structural change during recovery is that the deformation structure coarsens and evolves from a lamellar structure to a more equiaxed configuration (Prangnell *et al.* 2004; Xing *et al.* 2006). It follows that removal of lamellar and interconnecting boundaries is a key issue when modelling the microstructural evolution. Rotation and coalescence (Li 1962; Jones *et al.* 1979) may be a possibility for removal of interconnecting boundaries but may not be operative for lamellar boundaries which have medium-to-high angles.

For these boundaries a possibility is coarsening by strain induced grain boundary migration (SIBM), which is a common process when recrystallizing samples deformed to low and medium strains (Beck and Sperry 1950). However, this process is not likely to operate easily at low temperatures in highly-strained samples where the structure is extremely fine, and it has not been observed in the present study. A third mechanism is based on a lamellar structure with exactly parallel lamellar boundaries and interconnecting boundaries along a direction perpendicular to the lamellar boundaries, i.e. a structure without Y-junctions. This idealized structure has been taken to represent deformation bands observed at a medium strain (Dillamore *et al.* 1972) and rolling structures observed at a large strain (Jazaeri and Humphreys 2004). During annealing of such a structure it is suggested that a reduction in boundary energy can be established by a shortening of the interconnecting boundaries and thereby locally pulling the lamellar boundaries together. A further step is a collapse of lamellar boundaries (Jazaeri and Humphreys 2004), annihilating two H-junctions and forming two nodes, which are Y-junctions. The resulting structure is a diamond-shaped structure and it is suggested that further spheroidization and growth will occur homogeneously due to boundary tensions, leading to a more equiaxed grain structure.

The present observations suggest a new mechanism for structural coarsening during the initial stage of recovery in a lamellar structure, namely motion of Y-junctions. In TEM foils migration of a Y-junction shortens confined lamellae and finally removes them by annihilation of Y-junctions. In the bulk, migration of a Y-junction shortens the Y-junction line and finally removes the confined lamella together with H- and r-junctions within the lamella. As a result, the motion of the Y-junction can lead to removal of both lamellar and interconnecting boundaries and cause a structural coarsening as observed (e.g. Figure 4.11). Analysis of the details of structural coarsening shows a decrease in the triple junction density, an increase in the average lamellae spacing, and decreases in the aspect ratios (L/D and l/D), towards a more equiaxed morphology. Besides recovery by triple junction motion, other

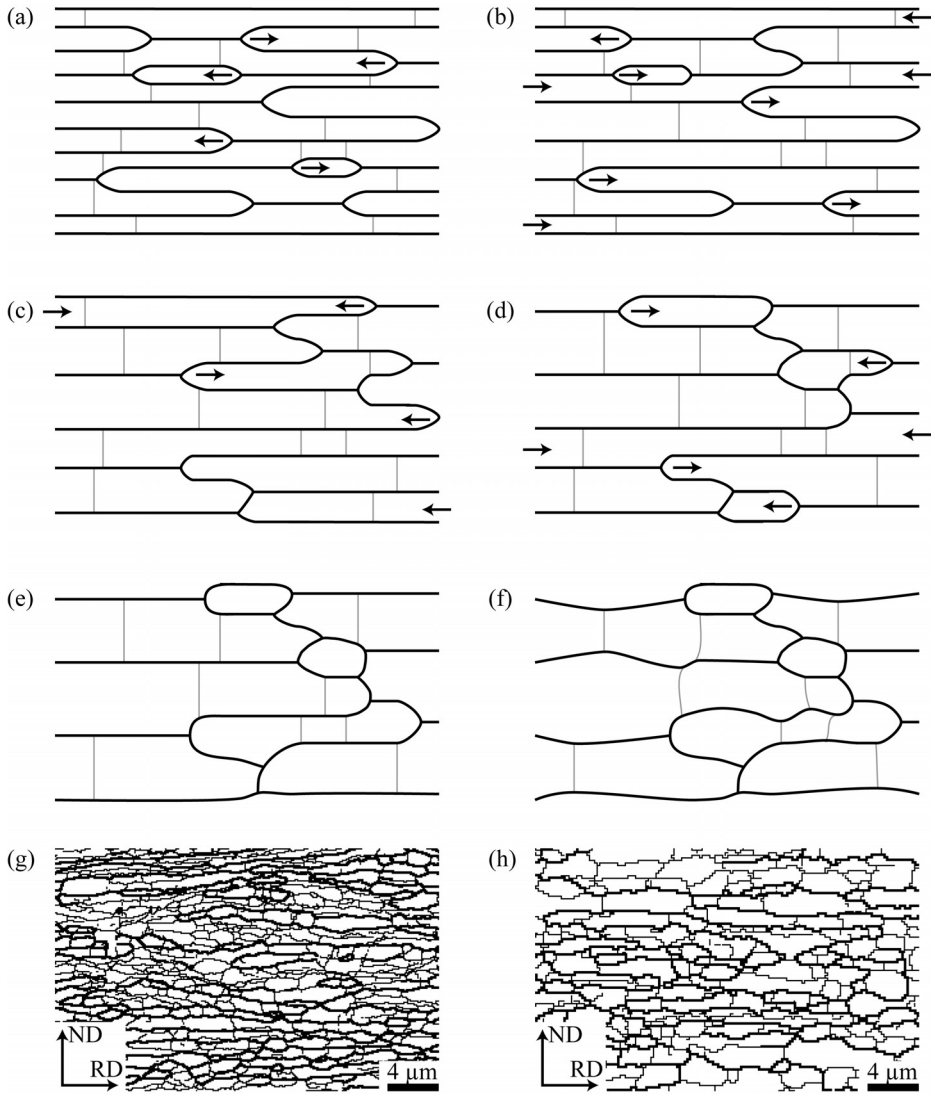

Figure 4.19: Schematic diagrams illustrating structural coarsening via Y-junction motion. (a) The original deformation structure with typical lamellar boundaries (bold black lines) and interconnecting boundaries (thin grey lines). This lamellar structure coarsens via Y-junction motion where arrows show the direction of the motions. (b)~(d) Intermediate coarsening steps. (e) A more equiaxed structure has evolved after coarsening via Y-junction motion. (f) A modified equiaxed structure considering also the drag of interconnecting boundaries at H-junctions (i.e. interconnecting boundaries resist widening). (g) and (h) Examples of such coarsening structures in AA1050 aluminium deformed to a strain of 5.5 and annealed at 220°C for 1 h and 48 h, respectively.

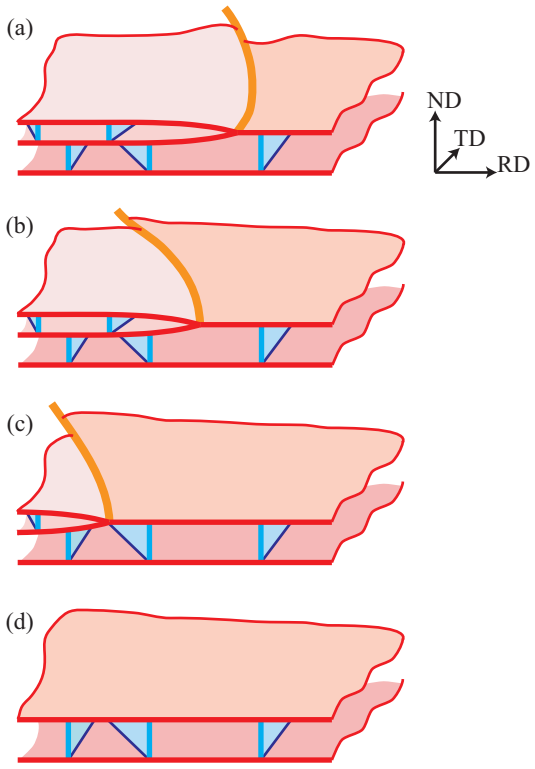

Figure 4.20: Schematic illustration of Y-junction motion in a three-dimensional lamellar structure with the same markings as in Figure 4.4.

processes may take place simultaneously, for example annihilation of mobile and redundant dislocations, leading to a decrease in the dislocation density in the lamellae and a sharpening of the dislocation boundaries (Humphreys and Hatherly 2004). However, these may not have a significant effect on the structural coarsening since these processes do not lead to removal of lamellar boundaries. The observation and analysis suggests that recovery of a lamellar structure by motion of Y-junctions is a critical process and Figure 4.19 gives a schematic drawing illustrating how this mechanism can lead to structural coarsening and a transition towards an equiaxed morphology. In Figure 4.20, triple junction motion in a three-dimensional lamellar structure is illustrated.

4.5.3 Recovery mechanisms and structural observations

The recovery mechanism illustrated in Figure 4.19 leads to a significant increase in the average lamellar boundary spacing, whereas the average lamella length and the average interconnecting boundary spacing may only

change marginally. Such a microstructural change leads to a more equiaxed morphology, which is consistent with experimental observations since equiaxed structures are typical observations after recovery annealing of deformed metals (e.g. Prangnell *et al.* 2004; Xing *et al.* 2006). However, it must be noted that this equiaxed structure with l/D~1 after coarsening still retains lamellar features since L/D>1, and a more perfect equiaxed structure requires further Y-junction motion and subgrain growth, also leading to a larger subgrain or grain size.

The mechanism suggests that interconnecting boundaries are stable and resist widening, leading to deflection of lamellar boundaries during coarsening (see e.g. Figure 4.8). Also, interconnecting boundaries appear to be stable and are generally not observed to pull lamellar boundaries together as suggested by Prangnell *et al.* (2004) and Jazaeri and Humphreys (2004). Also extensive breakdown of lamellae after they are pulled together will lead to a rapid decrease of the lamella length. However, according to Equation (4.4), the average lamellar length $L = \pi/(\rho_Y D)$, and with the data in Figure 4.17 it follows that the average lamella length increases slowly during annealing, in favour of the present mechanism. Moreover, extensive breakdown of lamellae will lead to a rapid evolution of an equiaxed structure with a minor increase in boundary spacing, in contradiction to experimental observations that the lamellar morphology is retained after doubling the lamellar boundary spacing (Figure 4.11).

According to the proposed mechanism, thick lamellae are more stable than thin lamellae, which are terminated by small dihedral angles at Y-junctions and provide large grain boundary surface tensions for Y-junction motion, and coarsening takes place uniformly by continuous removal of the thin lamellae. Such a uniform coarsening may result in a rough scaling behaviour of the distribution of the lamellar boundary spacings as in the case of a structural refinement by rolling (Godfrey and Hughes 2000). However, slight changes in the shape of the scaled distribution may also be expected during uniform coarsening due to a particular initial distribution of spacings in the deformed state (i.e. the shape of the scaled distribution may approach a stable one,

which may be different from that characterizing the deformed state). Since observations (Hughes and Hansen 2000; Godfrey and Hughes 2000) show that the initial distribution is always positively skewed (the tail on the right side is longer than the left side), the skewness of the distribution will decrease slightly due to uniform coarsening by removal of thin lamellae (e.g. those thinner than the average) and the distribution will become more symmetric. This is confirmed by the present EBSD data on the strain 5.5 aluminium as shown in Figure 4.21, where the skewness decreases at the beginning of recovery. This figure also shows that the skewness increases at longer annealing times, indicating the initiation of non-uniform coarsening, which is not governed by triple junction motion.

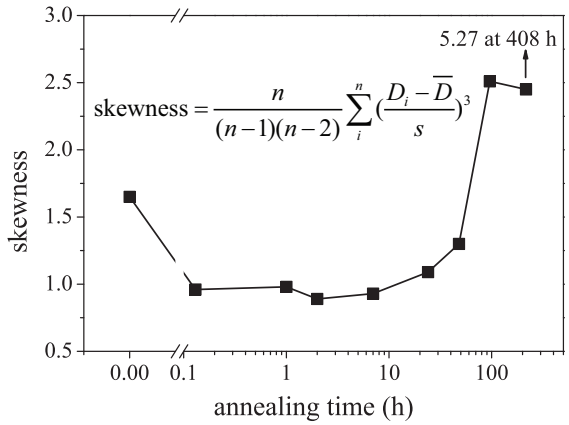

Figure 4.21: Evolution of the skewness of the lamellar boundary spacing distribution in the strain 5.5 aluminium during isothermal annealing at 220°C. In the definition of skewness, n is the size of the distribution, D_i is the i^{th} element in the distribution, $\overline{D}$ is the mean, and s is the standard deviation.

An analysis of the kinetics of recovery based on motion of Y-junctions is not part of the analysis. However, the observation that Y-junction motion is thermally activated agrees with previous models for recovery kinetics (Humphreys and Hatherly 2004). The finding in one new model (Vandermeer and Hansen 2008) that the apparent activation energy increases from the beginning of recovery to the beginning of recrystallization may relate to the observation that thin lamellae appear to be more unstable than thick ones,

which have a lower grain boundary surface tension. As a result, it is to be expected that it will be increasingly difficult to remove lamellae in the course of recovery, leading to an increase in the apparent activation energy as observed.

Y-junctions are stabilized to some extent by H-junction pinning (see Figure 4.8). This Y-H pinning, as well as Y-Y pinning and particle pinning, is related to an increase in the dihedral angle of Y-junctions and thus reduces the grain boundary surface tension on Y-junctions. The fact that enhanced Y-junction motion takes place at a high strain indicates that an increase in Y-H pinning has a limited effect when the strain is increased. Stabilization by particle pinning is a possibility and a reduction in the density of Y-junctions is another, for example by changing the deformation process in such a way that the morphology of the deformed microstructure can be changed from lamellar to equiaxed.

4.6 Summary

The study of triple junction motion is the key part of the PhD work, and the following conclusions can be drawn.

(1) Based on boundary morphology, triple junctions in a lamellar structure have been classified into three categories (Y-junctions, H-junctions, and r-junctions). The relationship between the density (length per unit volume) of each type of triple junctions and the boundary spacing has been formulated. The triple junction density increases with increasing degree of strain, and decreases during annealing.

(2) Thermally activated Y-junction motion is identified as a key process during coarsening of highly-strained aluminium (ε = 2~5.5) over a wide temperature range (from room temperature to 220°C) both at the sample surface and in the sample interior. The motion of Y-junctions, accompanied

by lateral movement of lamellar boundaries, causes shortening and removal of lamellae and local widening of neighbouring lamellae.

(3) The stability of a Y-junction is found to be more dependent on its morphology than the misorientation angles of adjoining lamellar boundaries. The dihedral angle of Y-junctions roughly decreases with decreasing lamellar boundary spacing, and the decrease in the dihedral angle increases the grain boundary surface tension for Y-junction motion. The stability of lamellae consequently decreases as the lamella spacing decreases although it is also affected by neighbouring Y-junctions, H-junctions and pinning particles.

(4) A recovery mechanism based on triple junction motion is proposed, and it explains how a lamellar structure evolves into a more equiaxed structure by continuously removing the thin lamellae, which have small dihedral angles at the ends and provide large grain boundary surface tensions for Y-junction motion. This mechanism underpins the observation that the apparent activation energy for recovery increases during recovery.

Chapter 5

Recovery at low temperatures

This chapter reports the recovery at low temperatures (5~100°C) in heavily deformed AA1050 aluminium. It includes data collected from a number of techniques, i.e. hardness tests, positron annihilation lifetime spectroscopy (PALS), electron backscattered diffraction (EBSD), and transmission electron microscopy (TEM). The recovery at low temperatures is found to be rather limited and is associated with a low activation energy.

The chapter starts with a short introduction of the background information. The experimental details and results are then described, followed by a thorough discussion of recovery mechanisms which may operate in heavily deformed aluminium at low temperatures.

This chapter is primarily based on Paper V.

5.1 Introduction

For metals with a medium-to-high stacking fault energy, e.g. Cu, Ni, Al, and Fe (iron), a cell block structure is typically formed after plastic deformation, following the principle of low energy dislocation structure (LEDS) (Kuhlmann-Wilsdorf 1989; Bay *et al.* 1992; Hansen 2001). The cell block structure contains high angle boundaries, dislocation boundaries and lattice dislocations between boundaries. A typical structure after low strain is shown in Figure 2.1. After deformation to high strains, the cell block structure

evolves into a lamellar morphology, with finely-spaced lamellar boundaries being typically medium-to-high angle boundaries and interconnecting boundaries being typically low angle dislocation boundaries (Hughes and Hansen 2000; Liu *et al.* 2002). A typical structure after high strain is shown in Figure 2.2. Early recovery studies were focused on samples deformed to relatively low strains (e.g. Hu 1962; Smith and Dillamore 1970; Prinz *et al.* 1982). However, the significant difference in the morphology and structural parameters between samples deformed to low and high strains may lead to significant difference in the recovery behaviour. Therefore the focus here will be on recovery in metals deformed to high strains.

After deformation to high strains, recovery and recrystallization may take place at room temperature or below in metals of high purity. For example, ≥99.99% pure aluminium deformed by torsion to various strains in liquid nitrogen was reported to recover and recrystallize below room temperature (Schmidt and Haessner 1990; Haessner and Schmidt 1993); and 99.96% pure copper heavily deformed by equal channel angular extrusion (ECAE) was reported to recrystallize during long-term room temperature storage (Mishin and Godfrey 2008). Metals of low purity are relatively stable even after deformation to high strains. In the case of aluminium, only a slight decrease in the hardness was observed when commercial purity aluminium (Cao *et al.* 2009) and Al-0.13%Mg alloy (Zahid *et al.* 2009) were annealed at 100°C after deformation to high strains. However, detailed recovery processes in metals deformed to high strains are rather unexplored except for subgrain growth (Humphreys 1997a,b; Xing *et al.* 2006; Ferry and Burhan 2007). During annealing of highly-strained low purity aluminium at 100°C and below, a number of processes may take place, altering and removing interior dislocations, interconnecting boundaries and lamellar boundaries. These recovery processes are examined in the following during annealing at low temperatures.

5.2 Experimental details

The AA1050 aluminium cold rolled to a true strain of 5.5 and subsequently stored in a freezer was chosen as the starting material for annealing, and the same cold rolled aluminium kept at room temperature was also investigated. All measurements were carried out one and a half years later after cold rolling, and in the following the freezer stored state is referred to as the FZ state and the room temperature stored state is referred to as the RM state.

After storage, a number of small specimens of the FZ state were cut and subjected to an isothermal heat treatment at temperatures of 5, 20, 40, 60, 80 and 100°C over time intervals ranging from 8 minutes to 112 days (Table 5.1). After each treatment, the sample was mechanically polished immediately, and the Vickers hardness was measured on the sample surface (rolling plane) within one hour. The hardness of the fully recrystallized state (ReX) was also measured.

Table 5.1: Choice of samples for characterization (FZ: freezer stored state; RM: room temperature stored state; ReX: fully recrystallized state).

State	Hardness	EBSD	TEM	*Ex situ* TEM	PALS
FZ	√	√	√	√*	√
FZ + 5°C	√				
FZ + 20°C	√				
FZ + 40°C	√				
FZ + 60°C	√	√	√		
FZ + 80°C	√				
FZ + 100°C	√				
RM	√	√	√		√
ReX	√				√

*The annealing experiments were carried out at room temperature and 60°C.

Three states, i.e. the FZ state, the RM state, and one selected annealed state (60°C for 7 days), were examined using the EBSD technique (Table 5.1). The microstructures were determined in the thickness centre in the longitudinal section. A scanning step size of 30 nm was chosen for all maps.

The EBSD technique can provide good statistics in boundary detection by covering a large area; however it cannot resolve individual dislocations in boundaries and between boundaries. Therefore TEM observations were also carried out for the three states, i.e. the FZ state, the RM state, and the annealed state (60°C for 7 days), in the longitudinal section (Table 5.1). The boundary spacings were measured and the densities of interior dislocations were determined. In order to view the evolution of dislocation structures directly, *ex situ* TEM observations were carried out in the longitudinal section of the FZ state samples during subsequent annealing at room temperature and 60°C, where the accumulated annealing time was 62 days and 7 days, respectively.

To compare the FZ state and the RM state on an even finer scale, PALS measurements were carried out for the two states, as well as the fully recrystallized state (500°C for 4 hours). All positron lifetime spectra could be resolved into two components. However in all cases, the dominating long-lived component had an intensity of 95% or more, whereas the lifetimes of the short-lived components showed large scatter among the various spectra. All spectra could also be well described by a single component, which was very close to the long-lived component in the case of resolving into two components. Therefore in the following all spectra were analyzed with a single component.

5.3 Results

5.3.1 Hardness and SEM data

The hardness data for different annealing conditions are shown in Figure 5.1, together with the hardness of the FZ state (H_{FZ}) and of the RM state (H_{RM}). The decrease of hardness over the annealing time, as well as an 8% decrease from H_{FZ} to H_{RM}, clearly indicates that recovery has taken place and softened the rolled aluminium. However, EBSD investigations showed that there was no significant difference in the boundary structure among the FZ state, the RM state, and the annealed state (60°C for 7 days). The average lamellar boundary spacing D^{EBSD} was almost the same (Table 5.2).

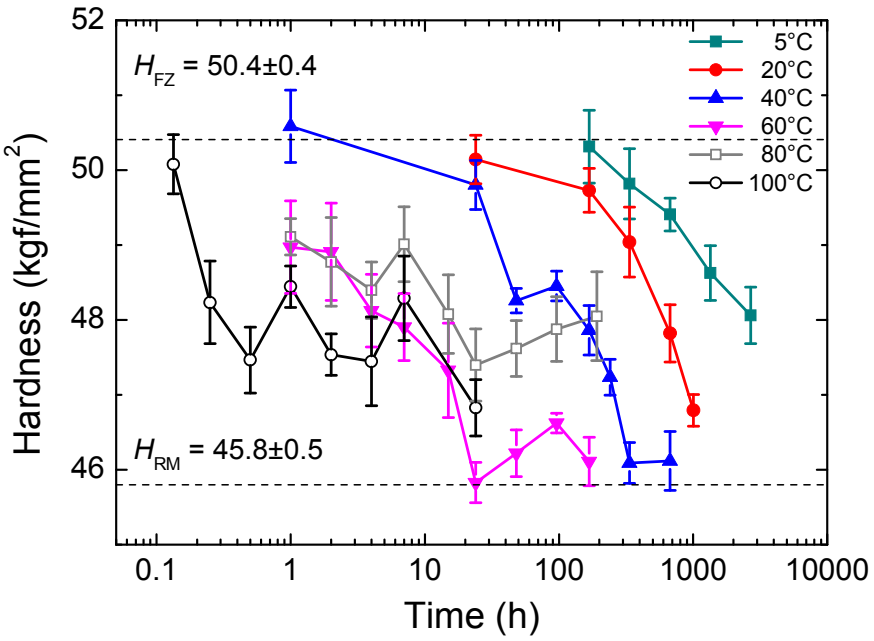

Figure 5.1: Hardness variation of AA1050 aluminium cold rolled to a strain of 5.5 with different annealing times and temperatures. Two dashed lines indicate the hardness before annealing (H_{FZ}) and the hardness of room temperature recovered state (H_{RM}), respectively. Error bars show the standard deviations.

Table 5.2: Experimental parameters of the AA1050 aluminium at different states (standard deviations are indicated for the hardness data whereas standard errors are used for other parameters).

State	H (kgf/mm^2)	D^{EBSD} (μm)	D^{TEM} (μm)	l (μm)	ρ_d (10^{13} m^{-2})	τ (ps)
FZ	50.4±0.4	0.24±0.01	0.23±0.01	0.81±0.05	7.5±0.8	242±1
RM	45.8±0.5	0.24±0.01	0.23±0.01	0.78±0.04	5.6±0.7	242±1
60°C 7 d	46.1±0.3	0.25±0.01	0.24±0.01	0.82±0.05	5.9±0.6	/
ReX	20.9±0.4	/	/	/	/	161±1

After prolonged annealing at 40°C and 60°C, the hardness approached a constant value, which is close to the hardness of the RM state H_{RM} (Figure 5.1). Annealing at 80°C and 100°C, however, led to hardness higher than H_{RM} as shown in Figure 5.1. It is therefore suggested that a hardening mechanism, probably precipitation hardening, also operated during annealing, which was also observed during annealing of AA1050 aluminium at higher temperatures (Bowen 2008; Vandermeer and Hansen 2008). The precipitation at 60°C was observed to be not significant as shown in Figure 5.2, where almost the same morphology as the FZ state can be seen, in contrast to that annealed at a higher temperature. Detailed analysis of the hardening behaviour is beyond the scope of the present study; however it may be assumed that the hardening effect is not significant in the present experimental work at annealing temperatures between 5°C to 60°C. The hardness of the initial cold rolled state (H_{CR}) is unknown, and therefore the present recovery kinetics analysis will focus on a small window as marked in Figure 5.3.

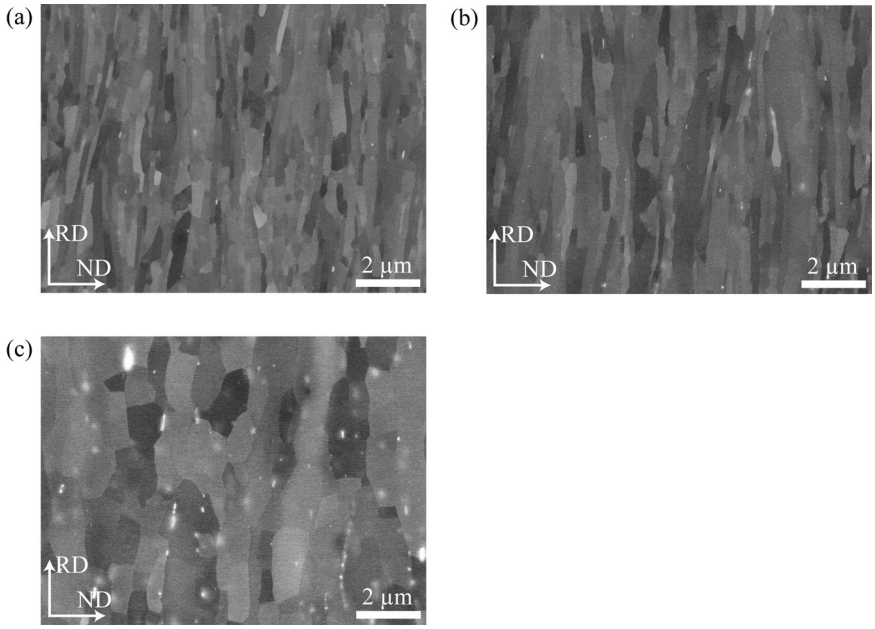

Figure 5.2: BSE images of AA1050 aluminium at different states: (a) the FZ state; (b) annealed at 60°C for 7 days; and (c) annealed at 220°C for 7 hours. Significant precipitation can be only observed after annealing at high temperatures.

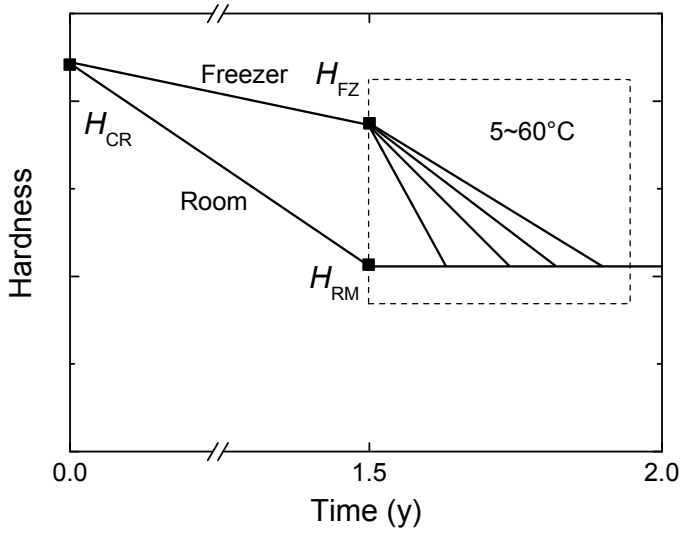

Figure 5.3: Schematic sketch of hardness variation of the samples after cold rolling, and the marked window corresponds to Figure 5.1.

For this recovery window, the fraction of recovery f can be expressed as:

$$f = \frac{H - H_{RM}}{H_{FZ} - H_{RM}}, \tag{5.1}$$

where H is the instantaneous hardness. Therefore the fraction f is supposed to decrease from one to zero during isothermal annealing at 5~60°C, and it represents to some extent the decrease of stored energy due to annealing out of defects. The parameter f will be used in the following as an attempt to analyze the kinetics of recovery at low temperatures. For such a small recovery window, it is reasonable to assume a constant activation energy and therefore Equation (2.2) may be used for this analysis. Assuming a first-order reaction rate, i.e. taking m=1 in Equation (2.2), and replacing the parameter P with f, one arrives at:

$$\frac{df}{dt} = -c_2 f \exp(-\frac{Q_0}{RT}). \tag{5.2}$$

The integration of the differential equation, together with the initial condition, results in:

$$\ln f = -c_2 \exp(-\frac{Q_0}{RT})t. \tag{5.3}$$

Performing further logarithmic transformation at both sides leads to:

$$\ln(-\frac{\ln f}{t}) = \ln c_2 - \frac{Q_0}{RT}. \tag{5.4}$$

At each annealing temperature, an average value of ln(-ln$f$/t) can be calculated. In Figure 5.4, ln(-ln$f$/t) is plotted versus 1000/T (the first data point at 40°C is ignored in averaging due to f>1), and by least square linear fitting the apparent activation energy is calculated to be 78±8 kJ/mol. It can be seen in Figure 5.4 that the standard error for the data point at 60°C is larger than others and this data point also shows more deviation than others. If we exclude this highest temperature, where the recovery mechanism may be different and the hardening effect may be not negligible, then the apparent activation energy calculated from linear fitting is 64±4 kJ/mol.

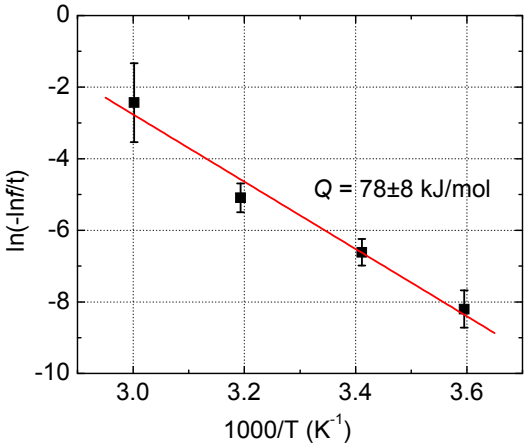

Figure 5.4: Temperature dependence of recovery kinetics in highly-strained aluminium from 5 to 60°C. Error bars show the standard errors.

Compared to the recovery study by Vandermeer and Hansen (2008), differences in the present analysis are that: (i) the RM state H_{RM} instead of the fully recrystallized state H_r = 20.9 kgf/mm^2 is taken as the ground state; (ii) the fraction f instead of f^2 is used (this will only affect the pre-exponential constant but not the activation energy); and (iii) a constant apparent activation energy is assumed. However, all combinations in choosing these parameters, including include/exclude 60°C, lead to similar apparent activation energies, 60~86 kJ/mol, for the small recovery window.

5.3.2 TEM results

TEM foils with large thin areas were produced for all three states examined, and an example is shown in Figure 5.5 for the FZ state. The lamellar boundary spacing D^{TEM} and interconnecting boundary spacing l measured by TEM is shown in Table 5.2, indicating no significant difference among the three states investigated, in a good agreement with EBSD measurements.

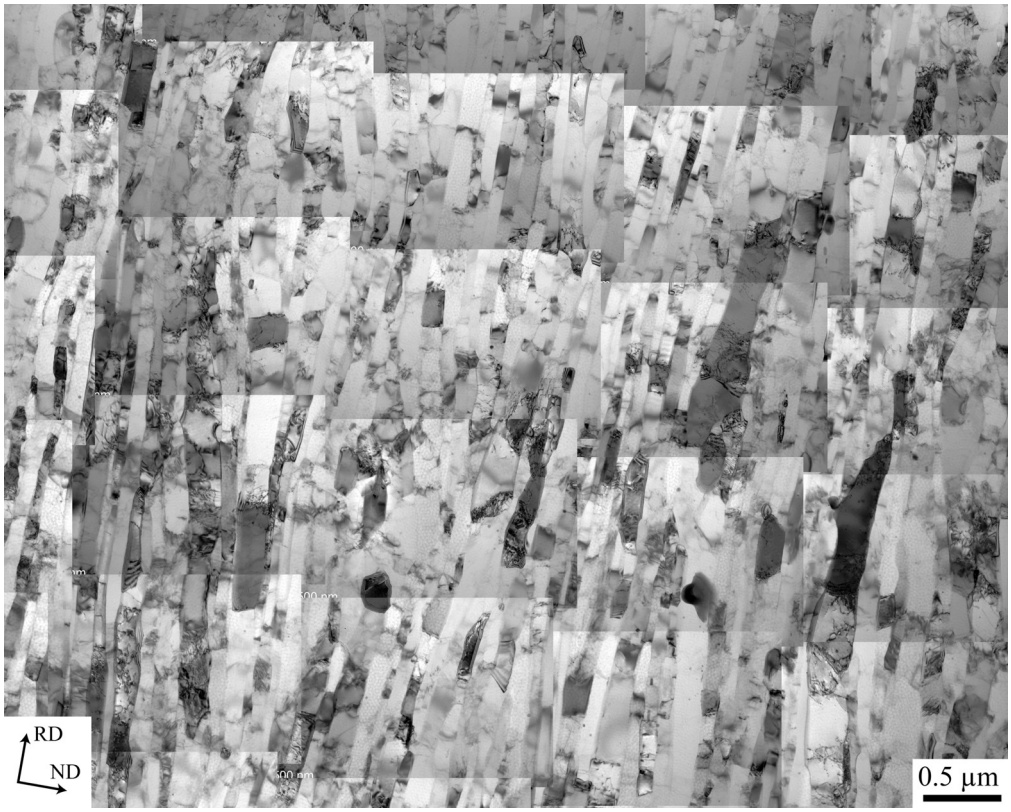

Figure 5.5: A TEM micrograph montage shows the microstructure in the longitudinal section of AA1050 aluminium in the FZ state.

Compared to the EBSD maps, TEM micrographs revealed more detailed microstructural features in the highly-strained aluminium. A part of a typical lamella at the FZ state is shown in Figure 5.6. It can be seen that lamellar boundaries are sharp boundaries. Between lamellar boundaries there are interconnecting boundaries and interior dislocations. Dislocations are typically connected to lamellar boundaries (see position A in Figure 5.6b) or interconnecting boundaries (see position B), although in the thin foils they may also being pinned at the surface. Dislocation lines are typically zigzagged (see position C), indicating these interior dislocations are generally pinned, e.g. by jogs, solutes, and small particles. For all three states, the dislocation densities were estimated to be quite similar (Table 5.2). However, the density for the FZ state is slightly higher than the other two, representing a more freshly deformed state. For all states, no vacancy clusters were observed.

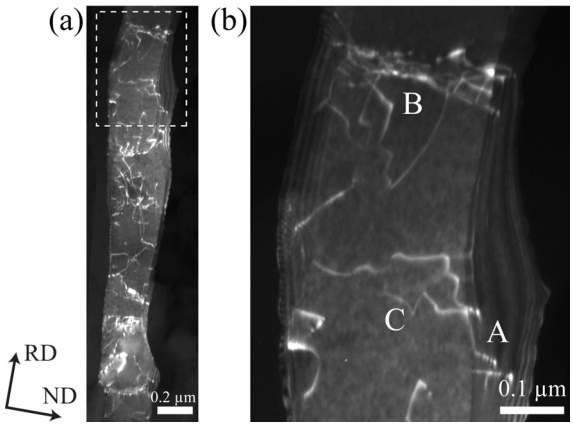

Figure 5.6: (a) A TEM micrograph shows a part of a typical lamella in the FZ state and the marked region is magnified in (b).

5.3.3 *Ex situ* TEM observations

During annealing of the FZ state aluminium foils at room temperature and 60°C, the microstructures were rather stable. Triple junction motion was only observed for the most closely spaced lamellae, and the extent of motion was strictly limited at both temperatures (Figure 5.7). Triple junction motion can remove lamellar boundaries and cause widening of the lamellar structure as shown in the previous chapter; however at room temperature and 60°C, such limited motion only had a marginal effect on the average lamellar boundary spacing, in agreement with the statistical lamellar boundary spacing measurements by EBSD and TEM as shown in Table 5.2.

Interconnecting boundaries were also found to be rather stable during annealing of the thin foils. No migration or dissolution (e.g. absorbed by neighbouring high angle lamellar boundaries leading to coalescence of adjacent cells) of interconnecting boundaries was observed, and the misorientation angles across interconnecting boundaries were found to be unchanged. In some cases, however, sharpening of interconnecting boundaries was observed, absorbing dislocations partially situated at the boundary. One example is shown in Figure 5.8 when annealed at 60°C.

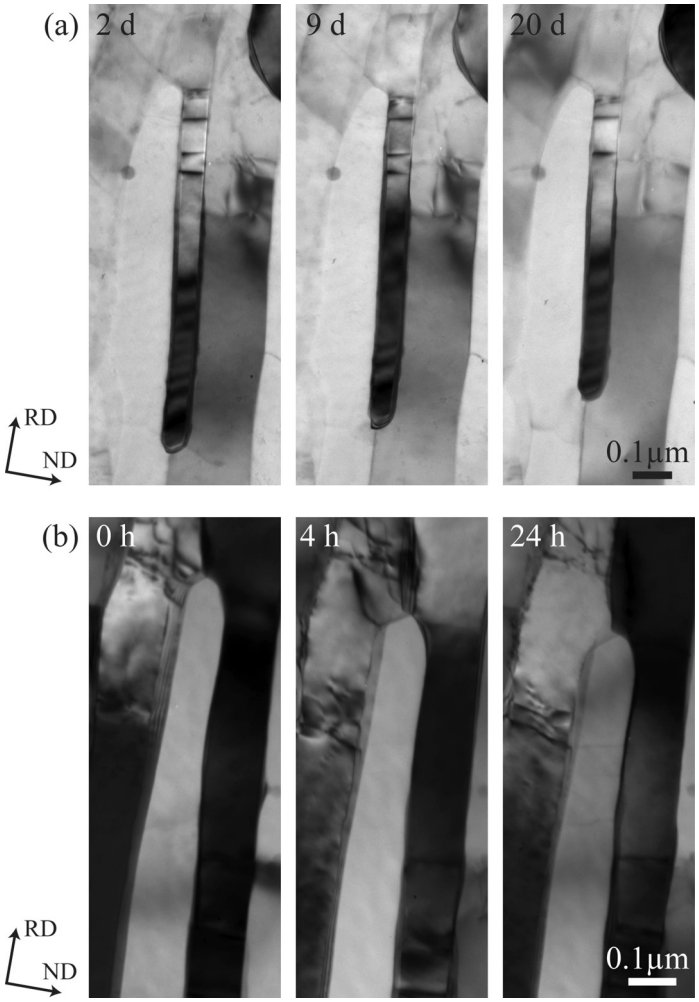

Figure 5.7: TEM micrographs show triple junction motion during annealing of the FZ state aluminium foil at (a) room temperature and (b) 60°C.

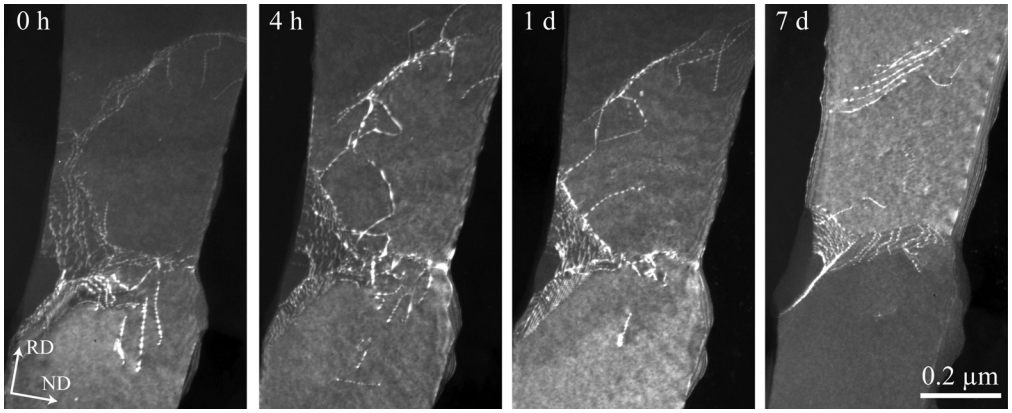

Figure 5.8: *Ex situ* TEM observations show sharpening of interconnecting boundaries during annealing at 60°C.

In regions between boundaries, a high density of zigzagged dislocations was present in the FZ state TEM foils. During annealing of the foils, dislocation annihilation and reconfiguration was frequently observed, and an example is shown in Figure 5.9 when annealed at room temperature. The pinning effect from particle can be also seen in Figure 5.9, where dislocation recovery in the upper part was retarded due to the presence of a particle. It should be also noted that a large fraction of zigzagged dislocations retained after annealing of the TEM foil at room temperature and 60°C, in agreement with dislocation density measurements of the RM state and the selected annealed state (Table 5.2).

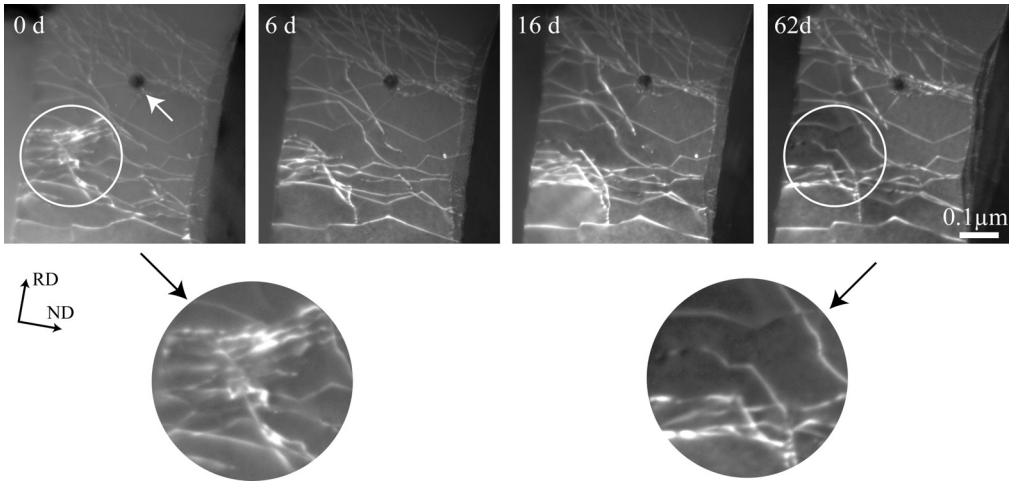

Figure 5.9: TEM micrographs show recovery of dislocation networks during annealing of the FZ state aluminium foil at room temperature. The marked areas are magnified showing annihilation of dislocations, and the white arrow indicates pinning of dislocations by a particle.

The surface effect in the statistical measurement of structural parameters (Table 5.2) may be ignored. However, this is not the case for the *ex situ* observations during annealing of the thin foils. Care was taken to distinguish the surface effect from general recovery mechanisms. Interconnecting boundaries were observed to be generally perpendicular to the lamellar boundaries, but randomly aligned with the longitudinal observation plane. During annealing of the TEM foils, it was also generally observed that these interconnecting boundaries always adjusted themselves to orient more perpendicular to the foil surface. An example is shown in Figure 5.10, where

the projected areas of the interconnecting boundaries decreased during annealing. This particular alignment must be induced by the surface of TEM foils. However, such a reduction in boundary area is believed to be a general phenomenon as interconnecting boundaries are generally perpendicular to the lamellar boundaries. As an extreme case, it was also found that dislocations in interconnecting boundaries in the vicinity of the surface may escape to the surface as shown in Figure 5.11.

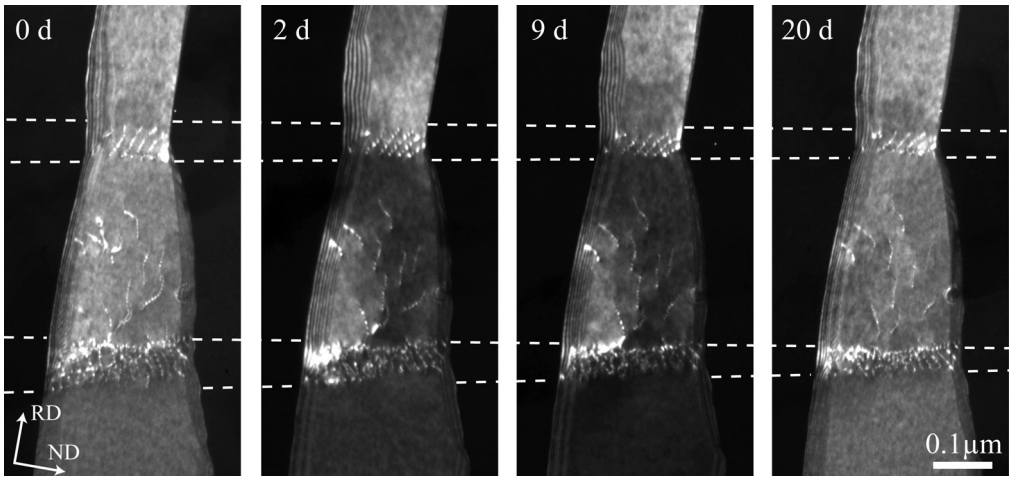

Figure 5.10: TEM micrographs show reorientation of interconnecting boundaries during annealing of the FZ state aluminium foil at room temperature.

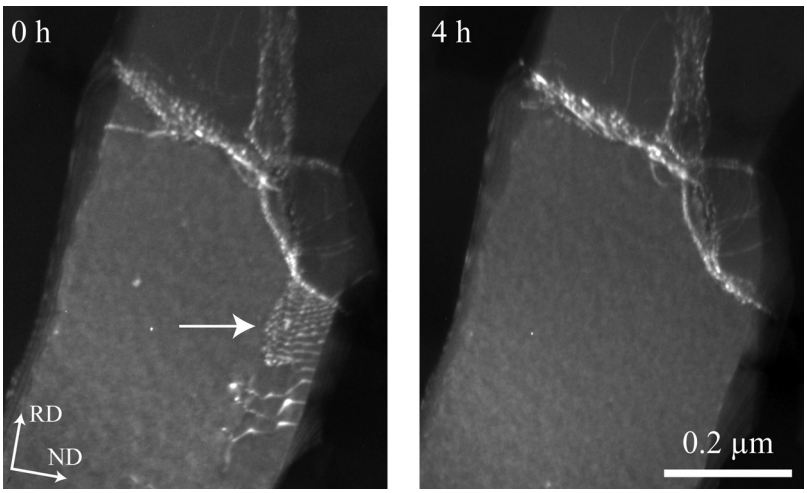

Figure 5.11: TEM micrographs show escape of interconnecting boundaries at surface during annealing of the FZ state aluminium foil at 60°C.

The interior dislocations were also affected by the surface since annihilation of dislocations may take place at the foil surface and stress may be relaxed at the surface. Detailed identification of the effect on each dislocation is not possible in a tangled dislocation structure. However, the marked stability of the FZ state TEM foils during annealing at room temperature as found through *ex situ* observations gives confidence to the statistical measurements of structural parameters.

5.3.4 PALS results

PALS data collected at room temperature from the FZ state and the RM state aluminium showed no discernible difference, with the lifetime of 242 ps being the same for two states (Table 5.2). This value is within a few picoseconds the same as found for the lifetime of positrons trapped in vacancies, not only at room temperature but observed over a wide temperature range of several hundred degrees Kelvin (Cotterill *et al.* 1972, Fluss *et al.* 1978, Jackman *et al.* 1987), and it is much larger than the lifetime of positrons in a perfect lattice of aluminium as in the fully recrystallized state (Table 5.2).

To further probe the detected trapping sites, more data were collected at different temperatures for the FZ state aluminium. Figure 5.12 shows that the positron lifetime decreases with decreasing temperature, reaching a value of 231 ps at 86 K. This is equivalent to a temperature coefficient of the relative lifetime change of $\sim 2.1 \times 10^{-4}$ K^{-1}, which is about three times the volumetric coefficient of thermal expansion of aluminium. Such large variation of the lifetime, much larger than literature values for vacancies (Jackman *et al.* 1987), suggests that other defects, with open volumes less than that of vacancies, also act as trapping sites for the positrons. High angle boundaries and triple junctions may be the type of defects which provide traps of vacancy sized volume, whereas all types of boundaries and their junctions, as well as dislocations, may contribute smaller sized traps. These traps give rise to positron lifetimes rather close to each other, and thus cannot be resolved

independently. Small traps contribute to a shorter lifetime than the mean, whereas large traps with a longer lifetime. The binding energy of positrons to small-volume traps is normally smaller than to, for example, vacancy sized traps. Therefore, at higher temperatures positrons may undergo thermally activated detrapping from small-volume traps that will only act as stable traps at low temperatures. This phenomenon probably explains why we observe a strongly temperature dependent lifetime (Figure 5.12), since at the lower temperatures the detected defects comprise both smaller and larger volumes, while at room temperature primarily larger volumes are detected.

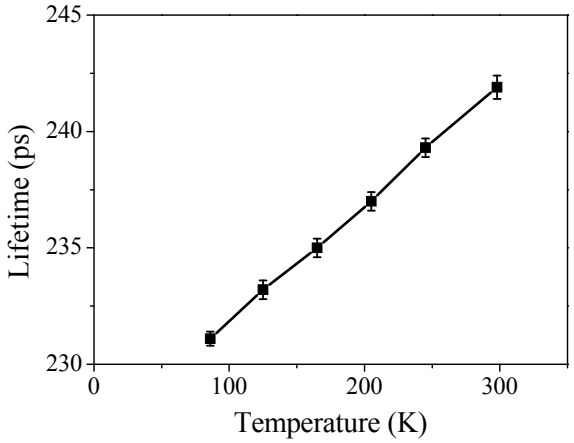

Figure 5.12: Temperature dependence of positron lifetime in the FZ state aluminium.

5.4 Discussion

Aluminium deformed to high strains, e.g. by rolling, is characterized by a lamellar structure, with interconnecting boundaries and interior dislocations between finely-spaced lamellar boundaries (Liu *et al.* 2002). A number of mechanisms with different activation energies may operate concurrently or consecutively during annealing, leading to an increase in the apparent activation energy as recovery proceeds (Furu *et al.* 1995; Vandermeer and Hansen 2008). The recovery behaviour in aluminium deformed to high strains may differ from that of low strains due to significant differences in the

morphology and structural parameters. For example in the previous chapter, a new recovery mechanism, triple junction motion, is found to be the key mechanism of structural coarsening of heavily deformed materials. However, triple junction motion is not likely to have a significant effect in the structural coarsening of lightly deformed materials due to the absence of a lamellar structure. A number of possible recovery mechanisms have been proposed primarily based on studies on metals deformed to low and medium strains (Li 1962; Sandstrom 1977a,b; Prinz *et al.* 1982; Doherty and Szpunar 1984). In the following, possible recovery mechanisms before significant structural coarsening takes place in heavily deformed aluminium are discussed when the deformed material is annealed at low temperatures.

5.4.1 Boundary migration

Migration of subgrain boundaries is generally considered as an important part of the recovery processes (Sandstrom 1977b; Furu *et al.* 1995). However, in a lamellar structure produced by plastic deformation to high strains, both lamellar boundaries and interconnecting boundaries are difficult to migrate at low temperatures. Lamellar boundaries are generally flat, with the curvature maximum at triple junctions (Figure 5.7). The boundary velocity v is usually assumed to be proportional to the driving pressure P and mobility M as

$$v = P \cdot M \,. \tag{5.5}$$

If the migration is thermally activated and the driving pressure is given by the boundary curvature with $P \sim 2\gamma/r$, the boundary velocity will be

$$v = \frac{2\gamma}{r} M_0 \exp(-\frac{Q_b}{RT}) \,, \tag{5.6}$$

where γ is the boundary energy, r is the radius of curvature, M_0 is a pre-exponential constant, and Q_b is the activation energy for boundary migration. For a dilute aluminium alloy during grain growth (Jazaeri *et al.* 2006), the factor M_0 was determined to be 0.125 $m^4/J/s$ and Q_b =130 kJ/mol. Therefore at room temperature for a high angle boundary with energy γ = 0.324 J/m^2

and minimum radius of curvature r = 50 nm, the velocity will be 1.2×10^{-17} m/s. In other words, high angle boundaries will not migrate at room temperature. This analysis is in general agreement with experimental observations, with the only exception of lateral movement of boundaries following triple junction motion, which should be considered as a different mechanism. Due to the low energy and low mobility (Huang and Humphreys 2000) of low angle interconnecting boundaries, a similar analysis also shows that they will not migrate at room temperature, in agreement with experimental observations.

It was suggested by some authors (Prangnell *et al.* 2004; Jazaeri and Humphreys 2004) that due to the surface tension of interconnecting boundaries, interconnecting boundaries might pull lamellar boundaries together, leading to the collapse of lamellar boundaries at H-junctions. However, H-junctions are found to be remarkably stable at low temperatures, not deflecting the lamellar boundaries, in agreement with our theoretical analysis. It may also be worth to mention that the deflection of lamellar boundaries at H-junctions after annealing at medium temperatures (e.g. 120~220°C) is a result of Y-junction motion, since Y-junction motion causes widening of neighbouring lamellae but interconnecting boundaries within neighbouring lamellae resist widening.

5.4.2 Coalescence and rotation

Subgrain coalescence and rotation is also assumed to be a possible recovery mechanism (Hu 1962; Li 1962; Sandstrom 1977a), especially in the early stage of recovery for boundaries of very small misorientation angles (Gleiter 1969; Sandstrom *et al.* 1978). Such a mechanism may remove interconnecting boundaries, which have low misorientation angles, and lead to nucleation of recrystallization (Faivre and Doherty 1979; Jones *et al.* 1979). The mechanism may involve collective movement of dislocations in the boundary plane, with adjacent high angle boundaries absorbing these boundary dislocations (Li 1962; Jones *et al.* 1979; Doherty and Szpunar

1984); it may also involve extraction or emission of dislocations from the boundary to the grain interior (Sandstrom 1977a; Sandstrom *et al.* 1978). However, the contribution of subgrain coalescence to recovery may be not significant (Furu *et al.* 1995; Humphreys and Hatherly 2004). It should also be noted that previous *in situ* observations of coalescence were typically carried out above recrystallization temperatures in TEM thin foils, where boundary migration was retarded (Hu 1962; Sandstrom *et al.* 1978). In the present lamellar structure, no clear evidence of coalescence was observed during *ex situ* observation, and the average interconnecting boundary spacing was also very similar among different states. It follows that interconnecting boundaries in a lamellar structure are stable at low temperatures, accommodating misorientation changes across the boundaries, and a high activation energy is required to dissolve them.

5.4.3 Triple junction motion

During thermal annealing of metals deformed to high strains, lamellar boundaries may be removed by the motion of a triple junction formed by three lamellar boundaries (Y-junction), and this motion also removes interconnecting boundaries and interior dislocations within the disappearing lamella. In the previous chapter, Y-junction motion was found to be the key mechanism for the widening of a lamellar structure, and a significant increase in the lamellar boundary spacing was observed when heavily deformed AA1050 aluminium was annealed at 220°C (Figure 4.17). However, at low annealing temperatures, Y-junction motion was observed here to be very limited and only had a marginal effect on the average lamellar boundary spacing (see Table 5.2).

During migration of a Y-junction in a lamellar structure, one boundary is left behind, in contrast to boundary migration, where nearly perfect crystals are left behind the migrating boundaries. The special geometry of Y-junction motion in a finely-spaced lamellar structure may have a significant effect. For example, solutes may diffuse along two leading boundaries to the Y-junction

and deposit at the boundary left behind, lowering the activation energy associated with solute drag. It should be also noted that Y-junction motion in a lamellar structure during recovery is very different from that in tricrystals examined at high temperatures (Protasova *et al.* 2001). At the high temperature regime, high activation energies (~300 kJ/mol) for triple junction motion were reported (Protasova *et al.* 2001). If we make an extrapolation, then there should be no triple junction motion at room temperature, in contradiction to experimental observations (e.g. Figure 5.7a).

5.4.4 Dislocation annihilation and reconfiguration

After deformation to high strains, most of the dislocations are stored in the form of dislocation boundaries, reducing the energy per unit dislocation line (Kuhlmann-Wilsdorf 1989; Bay *et al.* 1992; Hansen 2001). Dislocation boundaries contribute to a fraction of lamellar boundaries and all interconnecting boundaries. In aluminium, due to the high stacking fault energy and low melting point (T_m), dislocation boundaries are generally sharp after deformation at room temperature ($T_m/3$) although some interconnecting boundaries are less sharp than others. Dislocations within those less developed interconnecting boundaries may interact with each other, annihilating redundant dislocations (i.e. dislocations unnecessary for the accommodation of the misorientation angle across the boundary) and rearranging the other dislocations. Such a sharpening of interconnecting boundaries may take place at low annealing temperatures if it has not completed during deformation (e.g. Figure 5.8).

After deformation to high strains, however, there are still some dislocations present between boundaries. These interior dislocations may annihilate in pairs, annihilating two opposite Burgers vectors; they may interact with interconnecting boundaries, altering the misorientation angle across the boundary; and they may also be absorbed by lamellar boundaries. The evolution of interior dislocations has been analyzed by Nes (1995), who considered four rate-controlling mechanisms: thermally activated glide, cross

slip, climb, and solute drag; and he concluded that either thermally activated glide or solute drag may be account for the characteristic logarithmic time dependence of recovery.

In the present study, dislocation annihilation was observed during annealing at room temperature and 60°C through *ex situ* TEM observations, and a reduction in the dislocation density from the FZ state to the RM state and the selected annealed state (60°C for 7 days) was also confirmed (Table 5.2). Therefore the anneal-out of dislocations is suggested to be an important recovery mechanism of nanostructured aluminium at low temperatures where structural coarsening is retarded. An estimate of the decrease in dislocation strengthening from the FZ state to the RM state also appears to be consistent with the decrease of hardness observed (Table 5.2).

An important observation here is that the interior dislocations presented after heavy deformation are generally zigzagged, indicating pinning by jogs, solutes, or small particles (or jogs contaminated by solutes or small particles), in agreement with the analysis by Nes (1995). Before significant precipitation takes place, the effect of particles may be assumed to be minor, and therefore either thermally activated glide of jogged screw dislocations or solute drag may be the rate-controlling mechanism. The former involves vacancy diffusion from vacancy-producing jogs to vacancy-absorbing jogs (Nes 1995), whereas the latter involves diffusion of solutes away from the dislocation or along the dislocation line. The activation energy for vacancy diffusion was reported to be 62.6 ± 5.8 kJ/mol (Desorbo and Turnbull 1959), in agreement with the present apparent activation energy determined from hardness data. The activation energies for diffusion of Fe and Si in aluminium lattice were reported to be 214 kJ/mol and 117.6 kJ/mol (Du *et al.* 2003), respectively; however the activation energies for solutes diffusion along dislocation lines should be expected to be much lower. Therefore, the low activation energy found may be either due to pinning by jogs (lattice diffusion of vacancies) or pinning by solutes (pipe diffusion of solutes).

5.4.5 Vacancies and open volumes at boundaries

Excess vacancies are produced during plastic deformation (Friedel 1964). According to Schmidt and Haessner (1990), the recovery of vacancies in aluminium is weakly dependent on its purity and strain. These authors found that vacancy annihilation took place below -40°C in high purity aluminium. In the present AA1050 aluminium deformed at room temperature, the lattice vacancy concentration at the RM state must have approached its equilibrium concentration after long-term room temperature recovery, as excess vacancies produced by plastic deformation must have been annealed out although new vacancies may be continuously produced, e.g. by the glide of jogged screw dislocations during recovery. For the FZ state, the lattice vacancy concentration should be similar to that of the RM state, since its positron lifetime is the same as the RM state. Here the positron annihilation data are interpreted as trapping by finely-spaced boundaries, where the maximum open volume is close to a monovacancy, in agreement with the interpretation in a previous study (Aina *et al.* 1997).

The open volumes associated with boundaries are often considered as due to storage of vacancies at the boundaries after deformation (Ungar *et al.* 2007), and thus boundaries in a heavily deformed structure are thought to be different from those in a recrystallized structure and the non-equilibrium of boundaries are thought to be the cause of rapid coarsening of metals after large strains, e.g. coarsening of a heavily deformed Al-3%Mg alloy at temperatures 170~275°C as reported by Wang *et al.* (1996). However, it is known that in pure metals, boundary diffusion, boundary migration, and lattice diffusion of vacancies have similar low activation energies (Humphreys and Hatherly 2004). If there is such a non-equilibrium boundary, the transition to a normal boundary is then likely to require a similar low activation energy since only some diffusion in the boundary region is required. In alloys, the activation energy for boundary migration may rise due to solute drag (Lucke and Stuwe 1971; Furu *et al.* 1995; Vandermeer and Juul Jensen 2001); other processes should still be associated with a low activation

energy. Therefore the transition to a normal boundary, as well as anneal-out of excess vacancies, should be completed before any significant boundary migration and this is consistent with the present results, as boundaries in the FZ state and in the RM state produced the same positron lifetime.

An alternative explanation for the special properties of a heavily deformed structure lies in the large boundary area per unit volume and the high fraction of high angle boundaries, which are generally more open and mobile than low angle boundaries (Humphreys and Hatherly 2004). The finely-spaced boundaries are all connected, and thus boundary diffusion, including solutes diffusing along boundaries, may play an important role in the rapid coarsening of the microstructure observed (e.g. Lian *et al.* 1995; Wang *et al.* 1996). Such an explanation is also consistent with more detailed structural observations, e.g. bands containing boundaries of higher misorientation angles coarsen more rapidly than bands containing boundaries of lower misorientation angles (Xing *et al.* 2006).

5.5 Summary

The recovery of commercial purity aluminium AA1050 cold rolled to a true strain of 5.5 has been followed at low temperatures (5~100°C) using various techniques, and the following conclusions can be drawn.

(1) Excess vacancies produced by cold rolling anneal out rapidly at room temperature, and grain boundaries also reach their normal condition before any significant migration.

(2) After deformation to a high strain, dislocations presented in the region between boundaries are generally zigzagged, indicating pinning by jogs, solutes, or small particles. The annihilation and reconfiguration of interior dislocations is an important recovery mechanism at low temperatures, associated with an activation energy 60~84 kJ/mol.

(3) Triple junction motion can operate at both low and high temperatures in a finely-spaced lamellar structure. However, at low temperatures, it is strictly limited and has a marginal effect on the structural evolution.

(4) Both subgrain coalescence and boundary migration may require a high activation energy, and thus both mechanisms are less important during annealing at low temperatures.

Chapter 6
Recovery kinetics

In this chapter, a new recovery model is developed based on the one proposed by Vandermeer and Hansen (2008). The new recovery model is built on hardness measurements, consistent with the old one, and it is applied to the annealing results (140~220°C) of aluminium deformed by cold rolling and accumulative roll bonding to high strains. Based on the model results, the activation energy of recovery is discussed and compared with that estimated from boundary spacing measurements. Moreover, the recovery kinetics is also discussed based on a number of structural parameters and possible recovery mechanisms.

The chapter starts with a short introduction of the background information, and then the recovery model is presented. The experimental details and results are then described, followed by a discussion of the model, the activation energy and the influence of structural parameters.

This chapter is primarily based on Paper VI.

6.1 Introduction

The significant difference in the morphology and structural parameters between samples deformed to low and high strains may lead to significant difference in the recovery behaviour. For example, Y-junction motion has been demonstrated in Chapter 4 as the key recovery mechanism before

nucleation of recrystallization in aluminium deformed to high strains, and this mechanism is not likely to operate in samples deformed to low strains due to the absence of the lamellar structure. Different recovery mechanisms may result in different recovery kinetics since each mechanism may have its own kinetics (Bever 1957). Due to limited knowledge on the mobility of triple junctions in a deformed structure, a kinetic equation based on triple junction motion is not formulized. Therefore in the following, the recovery kinetics of aluminium deformed to high stains will be analyzed based on appropriate empirical equations.

6.2 The recovery model

The model developed by Vandermeer and Hansen (2008) was established based on the flow stress, but the hardness was used instead in the evaluation since it is relatively easy to measure. For the same reason the hardness is used in the present analysis although the relationship between the hardness and the deformation stored energy is complex and cannot be easily quantified. However, as a first approximation, the hardness of a sample can be taken to be proportional to the square root of the stored energy, thereby representing the state of deformation and partial annealing in a sample. To eliminate proportionality constants involved in the relationship, the recovery will be discussed in terms of f^2, which is defined as

$$f^2 = \left(\frac{H - H_r}{H_d - H_r} \right)^2, \tag{6.1}$$

where H_d is the hardness of the deformed aluminium, H_r is the hardness of the completely recrystallized aluminium, and H is the measured instantaneous hardness after partial annealing. Therefore the parameter f^2 is supposed to be related to the stored energy after partial annealing.

Four recovery rate equations are described in Section 2.2.2, and the most flexible one, i.e. Equation (2.4), is adopted for the present model. When P in

Equation (2.4) is taken to be proportional to f^2 and with the aid of exponential integrals, the following recovery equation can be obtained (Vandermeer and Rath 1990; Vandermeer and Hansen 2008):

$$E_1\{\frac{\beta P_0 f^2}{RT}\} = E_1\{\frac{\beta P_0}{RT}\} + tt_0^{-1}, \tag{6.2}$$

where E_1 is the exponential integral of the quantity inside the bracket, i.e. $E_1(x) = \int_1^\infty [\exp(-tx)/t]dt$, P_0 is the deformation stored energy before annealing, and t_0^{-1} can be expressed as:

$$t_0^{-1} = K_0 \exp(-\frac{Q_0}{RT}). \tag{6.3}$$

The apparent activation energy Q_{app} and the internal state variable f^2 are related as:

$$Q_{app} = Q_0 - \beta P_0 f^2. \tag{6.4}$$

This analysis is similar to the one proposed by Vandermeer and Hansen (2008) with the exception that a calculated hardness of the recovered state is replaced by the measured hardness of samples in the annealed state. This hardness H (and f^2) may therefore include contributions from both recovery and recrystallization. A microstructural analysis is therefore included in order to identify annealing conditions at which the first recrystallization nuclei can be observed. These conditions are determined by microstructural examinations using EBSD and samples with nuclei are not included in the analysis. To estimate the model parameters t_0^{-1} and $\beta P_0/R$ for each annealing temperature, the values of (t, f^2) pairs are inserted into Equation (6.2) and a curve of t_0^{-1} vs $\beta P_0/R$ is calculated by computer for each (t, f^2) pair. Then at each temperature, a maximum convergence point ($\beta P_0/R$, t_0^{-1}) is determined by superimposing t_0^{-1} vs $\beta P_0/R$ curves of all annealing times where only recovery has taken place, and one example is shown in Figure 6.1. The model thus gives a fitting of the recovery curve, and by extrapolating to longer annealing times, the contribution of discontinuous recrystallization may be

factored out from samples where recovery and recrystallization take place simultaneously.

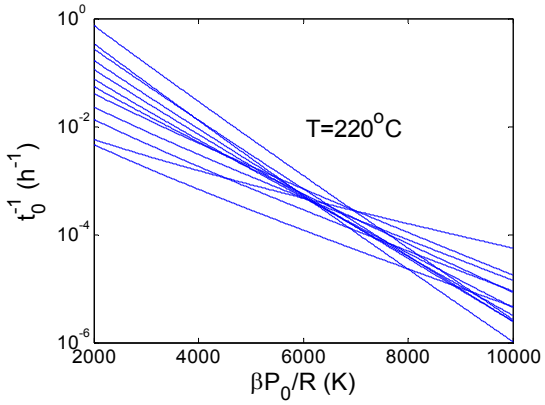

Figure 6.1: An example of the determination of recovery parameters $\beta P_0/R$ and t_0^{-1} (at the convergence point) by plotting at one temperature.

It should be pointed out that in the above fitting, the values of t_0^{-1} and $\beta P_0/R$ are assumed to be temperature dependent, and thus they may give some indications of different recovery mechanisms operating at different temperatures. However, in order to calculate the activation energy at the end of recovery Q_0, which is assumed to be temperature independent, one has to assume the same recovery mechanisms at a specific value of f^2 irrespective of the temperature, i.e. the values of K_0 and β (and thus also $\beta P_0/R$) have to be fixed. In the previous study (Vandermeer and Hansen 2008) the value of $\beta P_0/R$ was not fixed for the estimation of the activation energy, and the consequence will be discussed later.

6.3 Experimental details

As an extension to the previous study (Vandermeer and Hansen 2008), where AA1050 aluminium (Batch I) cold rolled to true strains 2 and 4 was analyzed, a similar AA1050 aluminium (Batch II) cold rolled to a true strain of 5.5 is studied here. As shown in the Appendix, the recrystallization behaviour between the thickness centre and the subsurface region is

significantly different in the strain 5.5 aluminium, and therefore the recovery kinetics is followed here in both the thickness centre and the subsurface region. From the material kept at room temperature, a number of smaller samples were cut and subjected to an isothermal heat treatment at temperatures of 140, 160, 180, 200 and 220°C over time intervals ranging from 1 minute to 51 days. After annealing, Vickers hardness tests were carried out both at the thickness centre and in the subsurface region (Table 6.1). The small load applied at the thickness centre in the longitudinal section was to ensure that the distance between the indentations to the sample edge was always larger than three times the indent size. The hardness of the deformed state and of the fully recrystallized state (500°C for 4 hours) was also measured, using different loads for different sections as in the case for recovered samples. For the deformed state, both samples stored in the freezer and kept at room temperature were measured.

Table 6.1: Choice on hardness measurement for aluminium deformed by cold rolling to a true strain of 5.5 (CR5) and deformed by ARB for 6 cycles (ARB6).

Material	Section	Region	Load
AA1050 CR5	Longitudinal plane	Centre	50 g
AA1050 CR5	Rolling plane	Subsurface	200 g
AA1100 ARB6	Rolling plane	Subsurface	200 g

To study the effect of deformation mode, AA1100 aluminium was deformed by ARB for 6 cycles without lubrication between each cycle. Annealing was then carried out in the same manner as for the cold rolled AA1050 aluminium. The recrystallization behaviour in the ARB deformed samples was found to be uniform through the sample thickness, and therefore the hardness was only measured in the subsurface region in the rolling plane (Table 6.1).

The microstructures of the deformed and annealed samples were determined in the longitudinal section by backscattered electron (BSE) imaging and EBSD as described in Chapter 3.

In the present model, the parameter f^2 is used to analyze the recovery kinetics. However, it is also quite common to use the fraction f directly, i.e. the recovery of the flow stress (Nes 1995). In this context, the present data were also analyzed using the parameter f. It turns out that the model fitted the experimental data slightly less satisfactory but the general conclusion was unchanged, and therefore only results using parameter f^2 will be given in the following.

6.4 Results

6.4.1 Thickness centre of cold rolled aluminium

The hardness of the strain 5.5 aluminium at the thickness centre was measured to be 51.2±0.8 kgf/mm^2 and 47.3±0.7 kgf/mm^2 for samples stored in the freezer and kept at room temperature, respectively. The decrease in hardness indicates that recovery had taken place at room temperature during long-term exposure, in agreement with the hardness measurements in the subsurface region (Table 5.2) although the exact value is slightly different. The slight difference may result from the different testers, different loads, different sections and different regions, and thus the two sets of data will be analyzed separately. This initial stage of recovery is studied in Chapter 5 and is found to be associated with a low activation energy. Here this part of recovery is assumed to be exhausted during the first minute of annealing at 140°C and higher temperatures. Therefore 51.2 kgf/mm^2 is taken as the hardness of the deformed state (H_d) in the kinetics analysis in order to include the initial stage of recovery.

The hardness variation at the thickness centre during isothermal annealing is shown in Figure 6.2. These curves indicate that hardening may be superimposed on recovery during the early stages of annealing, where the initial hardness was only 47.3 kgf/mm^2. The hardening may be due to dislocation source limited hardening (Huang *et al.* 2006a) or precipitation hardening as precipitates can be observed at longer annealing times (Figure 6.3). However, detailed analysis of hardening effects is beyond the scope of the present work. In order to minimize these hardening effects on the analysis of recovery kinetics, samples annealed at 140°C and 160° for less than one hour are excluded from kinetics analysis.

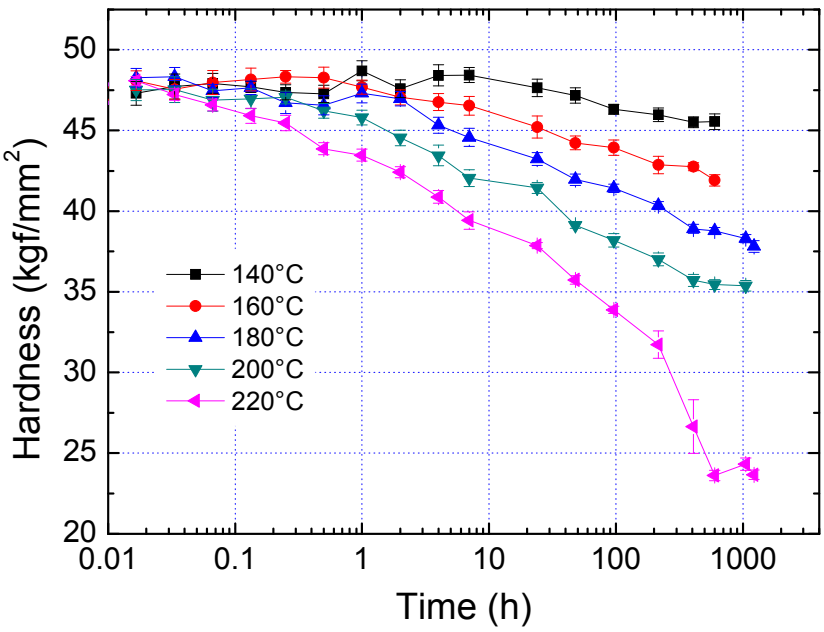

Figure 6.2: Hardness variation at the thickness centre of cold rolled aluminium upon thermal annealing. Error bars show the standard deviations.

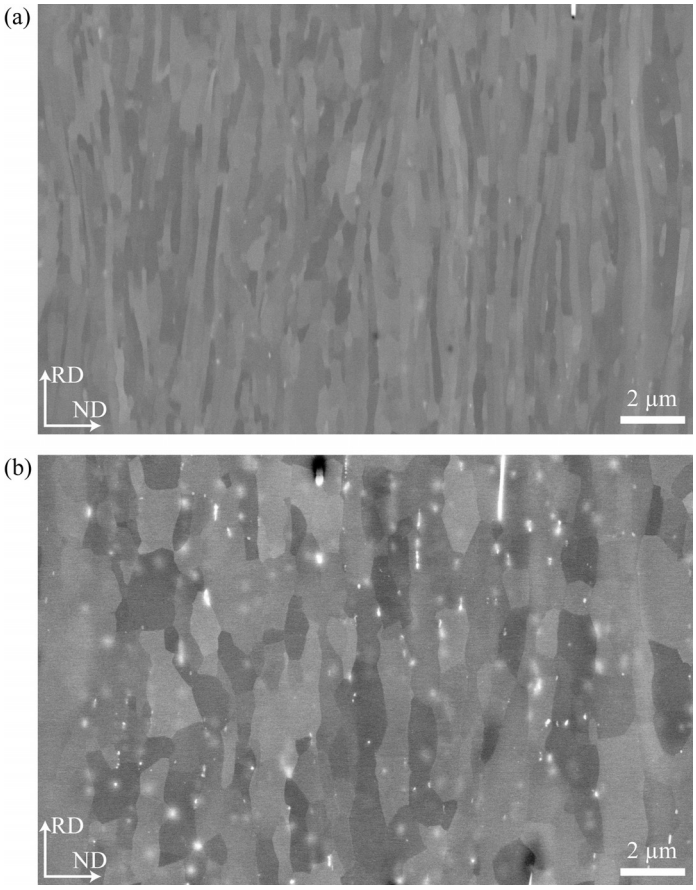

Figure 6.3: BSE images in the longitudinal plane of AA1050 aluminium (a) deformed to a true strain of 5.5 and (b) subsequently annealed at 200°C for 48 hours.

EBSD analysis of selected samples showed that there was no discontinuous recrystallization in samples annealed at 200°C and below. Characteristic nuclei started to form at the thickness centre of the sample after annealing at 220°C for 96 hours (Figure 6.4), in agreement with the hardness curve, where large standard deviations and a rapid decrease at longer annealing times indicating a mixture of recovered structures and recrystallized ones. Therefore samples annealed at 220°C for 96 hours and longer were excluded in the analysis of recovery kinetics. The hardness of the fully recrystallized state at the thickness centre (H_r) was measured to be 24.6±0.4 kgf/mm^2, also in agreement with the hardness of samples annealed at 220°C for the three longest times as shown in Figure 6.2.

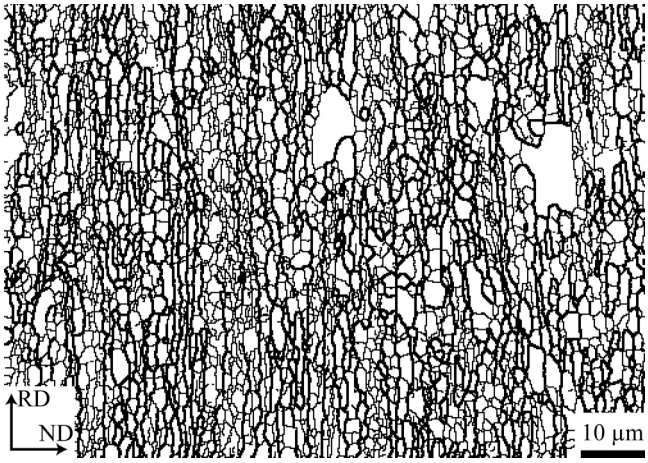

Figure 6.4: Boundary structures revealed by EBSD in the longitudinal plane (thickness centre) of AA1050 aluminium deformed to a true strain of 5.5 and annealed at 220°C for 96 hours. High angle boundaries (>15°) are shown in bold lines and low angle boundaries (1.5~15°) are shown in thin lines.

Based on the above proviso, the experimental recovery parameters (i.e. the convergence points) determined for individual temperatures are shown in Table 6.2. It can be seen that the parameter $\beta P_0/R$ decreases with increasing temperature, and therefore the apparent activation energy Q_{app} (see Equation (6.4)) increases with increasing temperature at a specific value of f^2. It indicates that several recovery mechanisms with different activation energies were operative during annealing, and those involving high activation energies contributed more at high temperatures than at low temperatures. Based on the parameters shown in Table 6.2, the corresponding recovery kinetics curves at different temperatures are drawn in Figure 6.5.

Table 6.2: Experimental recovery parameters for the thickness centre of AA1050 aluminium.

Temperature (°C)	t_0^{-1} (h^{-1})	$\beta P_0/R$ (K)
140	3.1×10^{-9}	7.8×10^{3}
160	1.8×10^{-7}	7.3×10^{3}
180	5.9×10^{-6}	6.6×10^{3}
200	9.2×10^{-5}	5.8×10^{3}
220	9.1×10^{-4}	5.4×10^{3}

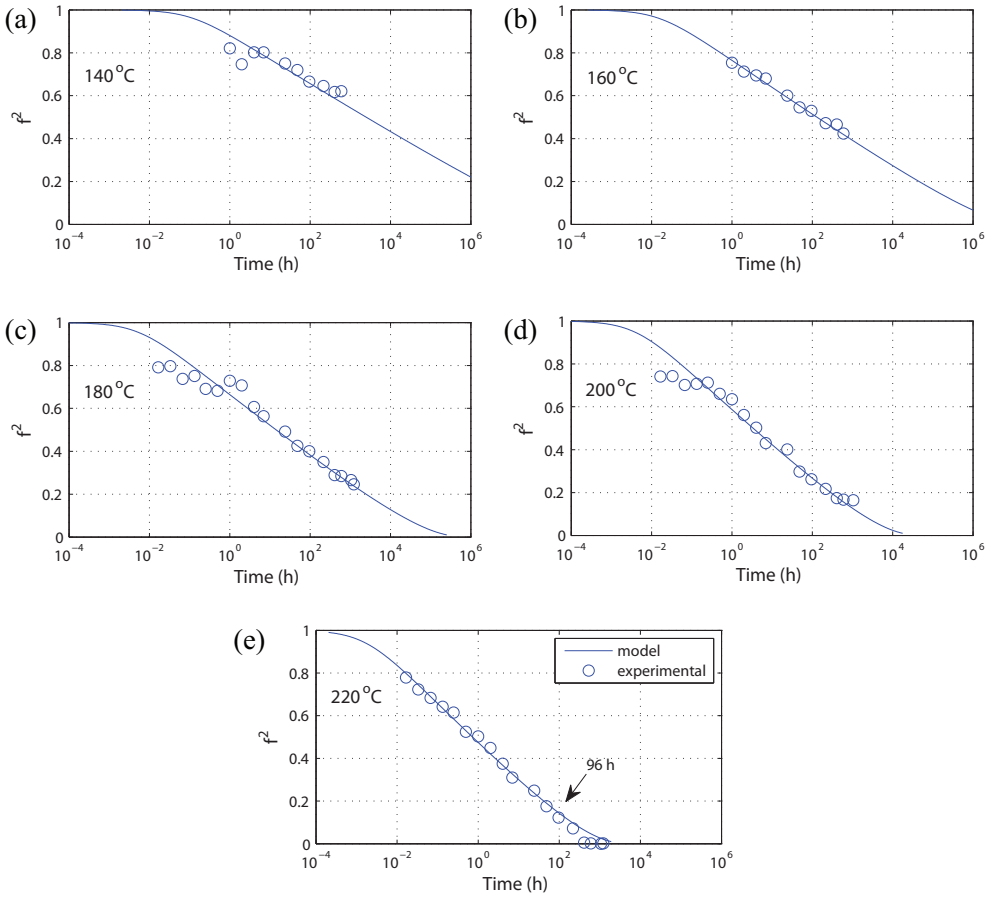

Figure 6.5: Isothermal kinetics of recovery at the thickness centre of AA1050 aluminium.

In order to estimate the activation energy, one has to assume the same recovery mechanisms at a specific value of f^2 independent of the annealing temperature. Taking the average value of $\beta P_0/R$ (6.6×10^3 K) for all temperatures, one obtains the adjusted best fit of recovery kinetics as shown in Figure 6.6. The corresponding values of t_0^{-1} are plotted against $1000/T$ in Figure 6.7, leading to the activation energy at the end of recovery Q_0 equal to 186±10 kJ/mol according to Equation (6.3). According to Equation (6.4), the apparent activation energy at the beginning of recovery can then be calculated as 131 kJ/mol. The model curves fit the experimental data quite well in Figure 6.6, giving confidence to the assumption (i.e. constant K_0 and β at different temperatures) and the activation energies determined.

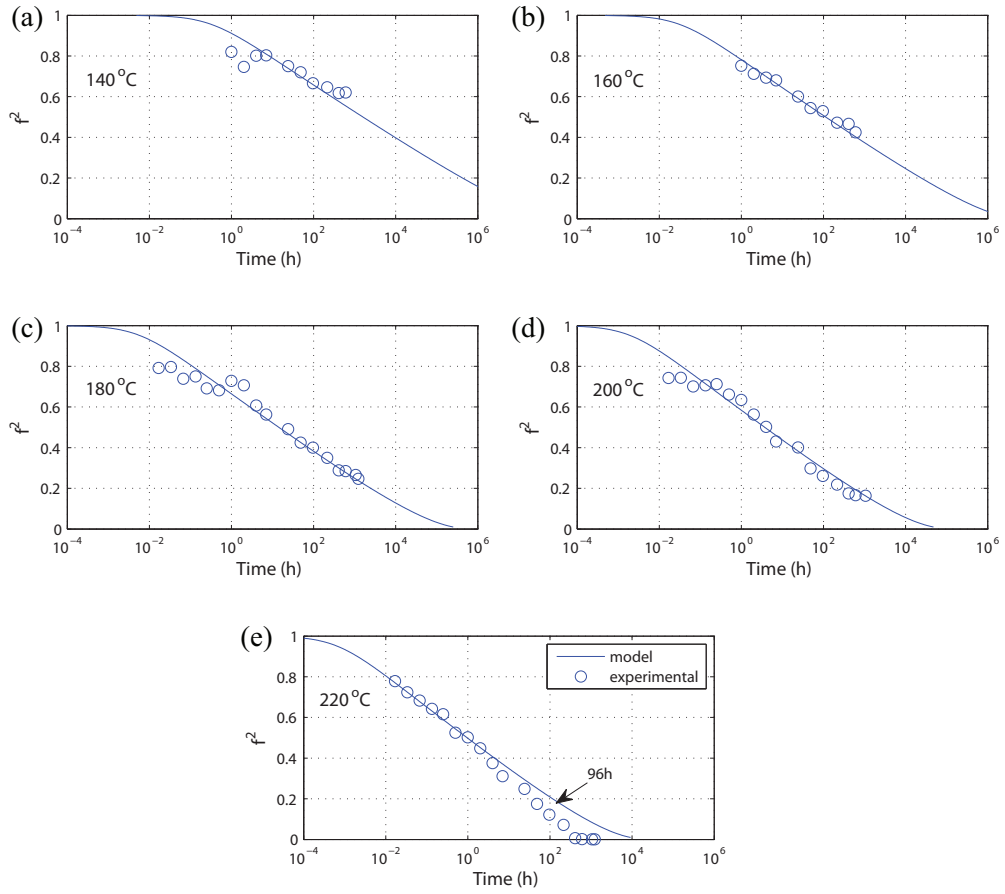

Figure 6.6: Isothermal kinetics of recovery at the thickness centre of AA1050 aluminium under the assumption of constant K_0 and β for all temperatures.

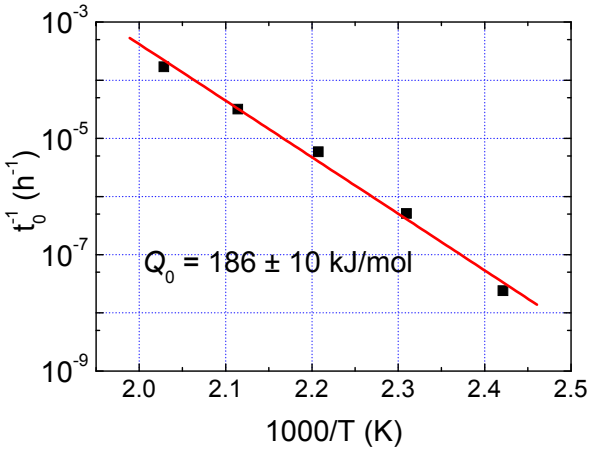

Figure 6.7: Temperature dependence of recovery kinetics at the thickness centre of cold rolled AA1050 aluminium under the assumption of constant K_0 and β for all temperatures.

It can be seen in both Figure 6.5 and Figure 6.6 that the model generally fits the experimental data better in the later part of recovery than in the beginning part. The large deviation in the beginning may result from concurrent hardening processes and the choice of H_d = 51.2 kgf/mm^2. If the long-term room temperature stored state is taken as the initial condition, i.e. H_d = 47.3 kgf/mm^2, then the beginning part cannot be fitted since the hardness is greater than the initial hardness due to hardening effects. With the choice of H_d = 47.3 kgf/mm^2, the value of $\beta P_0/R$ becomes smaller, but the general conclusion is unchanged. The decrease of $\beta P_0/R$ is reasonable since P_0 represents the deformation stored energy, which was partially consumed when H_d decreased to 47.3 kgf/mm^2. This change indicates that an early stage of recovery is not taken into account.

6.4.2 Subsurface region of cold rolled aluminium

The hardness of the strain 5.5 aluminium in the subsurface region is shown in Table 5.2, for both samples stored in the freezer and kept at room temperature. As in the case for the thickness centre, the freezer stored state is chosen as the deformed state, i.e. H_d = 50.4±0.4 kgf/mm^2. The hardness in the subsurface region of the fully recrystallized sample is also listed in Table 5.2, i.e. H_r = 20.9±0.4 kgf/mm^2. The hardness variation in the subsurface region during isothermal annealing is given in Figure 6.8, showing similar trends of hardening, recovery and recrystallization as in Figure 6.2 for the thickness centre. Similarly, samples annealed at 140°C and 160° for less than one hour are excluded from kinetics analysis in order to minimize the effect of hardening. It is shown in Figure A1 in Appendix that recrystallization nuclei grew from the thickness centre and reached the surface after annealing at 220°C for 408 hours, and therefore samples annealed at 220°C for 408 hours and longer are not included in the analysis of recovery kinetics.

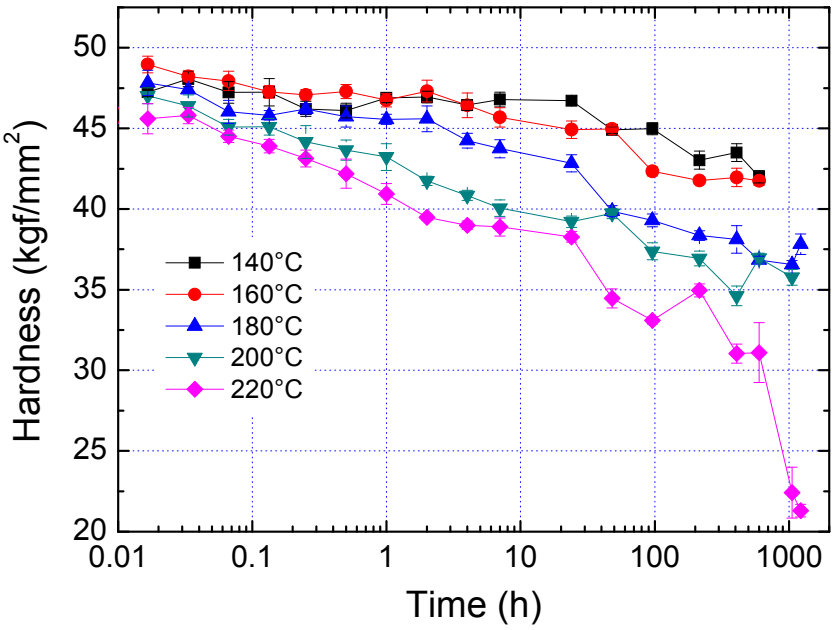

Figure 6.8: Hardness variation in the subsurface region of cold rolled aluminium upon thermal annealing. Error bars show the standard deviations.

According to the above proviso, the experimental recovery parameters $\beta P_0/R$ and t_0^{-1} can be determined, and the corresponding kinetic curves are drawn in Figure 6.9, showing a good fit with experimental data points. In order to estimate the activation energy, one has to fix the value of $\beta P_0/R$. Taking the average value of $\beta P_0/R$ to be 6.8×10^3 K and assigning it to all temperatures for the recovery in the subsurface region of strain 5.5 aluminium, one can get the corresponding values of t_0^{-1} at different temperatures as plotted in Figure 6.11. It follows that the activation energy at the end of recovery Q_0 equals 196±11 kJ/mol, in a good agreement with that found for the recovery at the thickness centre (186±10 kJ/mol). If both $\beta P_0/R$ and Q_0 are fixed at their average value for the two regions, then the pre-exponential constant K_0 can be also compared. Further analysis confirms that the value of K_0 is also quite close to each other, indicating the recovery kinetics is quite similar between the subsurface and the centre of the strain 5.5 aluminium although the recrystallization behaviour is significantly different (see Appendix).

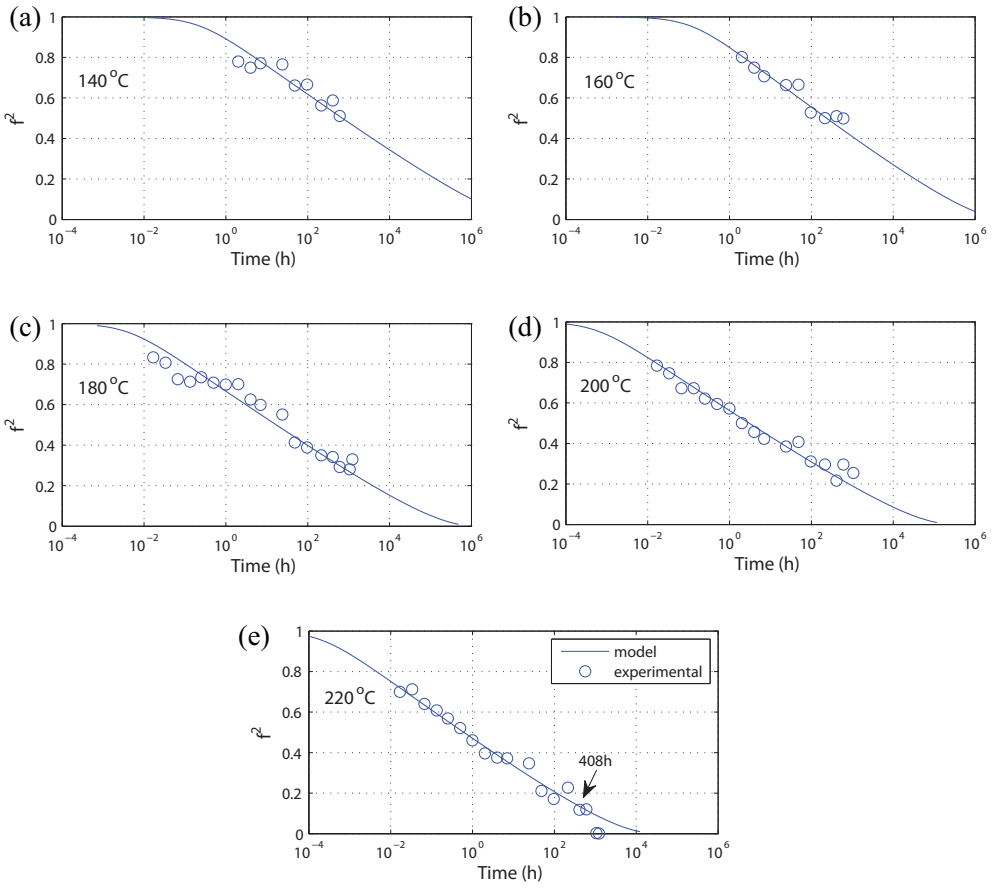

Figure 6.9: Isothermal kinetics of recovery in the subsurface region of AA1050 aluminium.

At this stage, one would also like to compare the present data with the recovery kinetics at lower strains analyzed by Vandermeer and Hansen (2008). However, some modifications have to be made before the comparison. In the previous study (Vandermeer and Hansen 2008), H_r = 27.3 kgf/mm^2 was used. However, as shown in Table A1 in Appendix, the fully recrystallized state has a much lower hardness. Therefore, the recovery kinetics of AA1050 aluminium cold rolled to true strains 2 and 4 is re-analyzed here using H_r = 21 kgf/mm^2. The consequent average value of $\beta P_0/R$ is shown in Table 6.3, and also shown is the value for the subsurface region of strain 5.5 aluminium. It can be seen that the value of $\beta P_0/R$ increases with increasing strain, indicating higher stored energy at higher strain. With the value of $\beta P_0/R$ fixed at each strain, the activation energy can be also estimated for the strain 2 and 4 aluminium as shown in Figure 6.11. A good

linear fitting is obtained for the strain 4 aluminium over the whole temperature range, leading to Q_0 = 192±5 kJ/mol, in a good agreement with the activation energy at a higher strain. The linear fitting for the strain 2 aluminium is less satisfactory, and the estimated activation energy, Q_0 = 141±17 kJ/mol, is also lower than for the other two strains. The large deviation at the lowest strain may be due to the low quality of the experimental hardness data. Nevertheless, the relative positions of the fitted lines in Figure 6.11 indicate that the recovery rate increases with increasing strain.

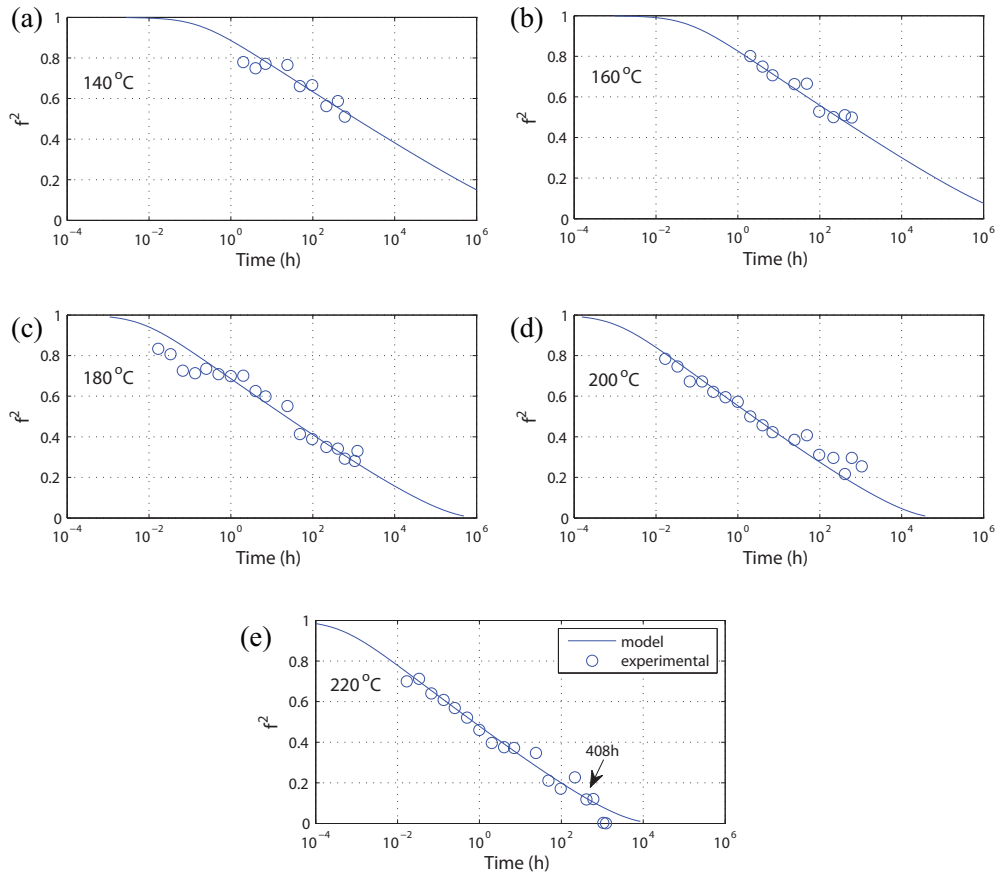

Figure 6.10: Isothermal kinetics of recovery in the subsurface region of AA1050 aluminium under the assumption of constant K_0 and β for all temperatures.

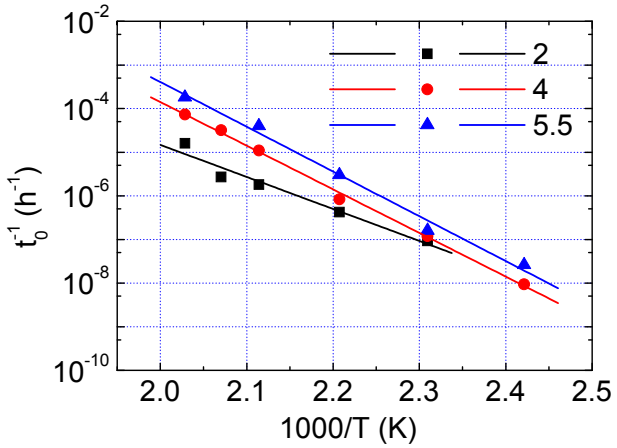

Figure 6.11: Temperature dependence of recovery kinetics in the subsurface region of cold rolled AA1050 aluminium at different strains. At each strain, the constants K_0 and β are fixed for all temperatures.

Table 6.3: The average value of $\beta P_0/R$ at different strains (all for the subsurface region).

Strain	$\beta P_0/R$ (K)
2	4.4×10^3
4	5.3×10^3
5.5	6.8×10^3

6.4.3 Aluminium deformed by ARB

The hardness of the AA1100 aluminium deformed by ARB was measured to be H_d = 86.5±1.6 kgf/mm^2 and H_r = 26.5±0.5 kgf/mm^2 for the deformed state and the fully recrystallized state, respectively. The hardness variation during isothermal annealing is shown in Figure 6.12, where a hardening effect can be also observed. As in the case of AA1050 aluminium, this may be due to dislocation source limited hardening or precipitation hardening. Precipitates were observed after annealing, and a precipitation-free zone was also found along the bonding layer (Figure 6.13), which may absorb oversaturated solutes in the matrix. In the beginning part of annealing, except

for annealing at 220°C, the hardness is greater than the initial hardness, and therefore this part is excluded from recovery kinetics analysis.

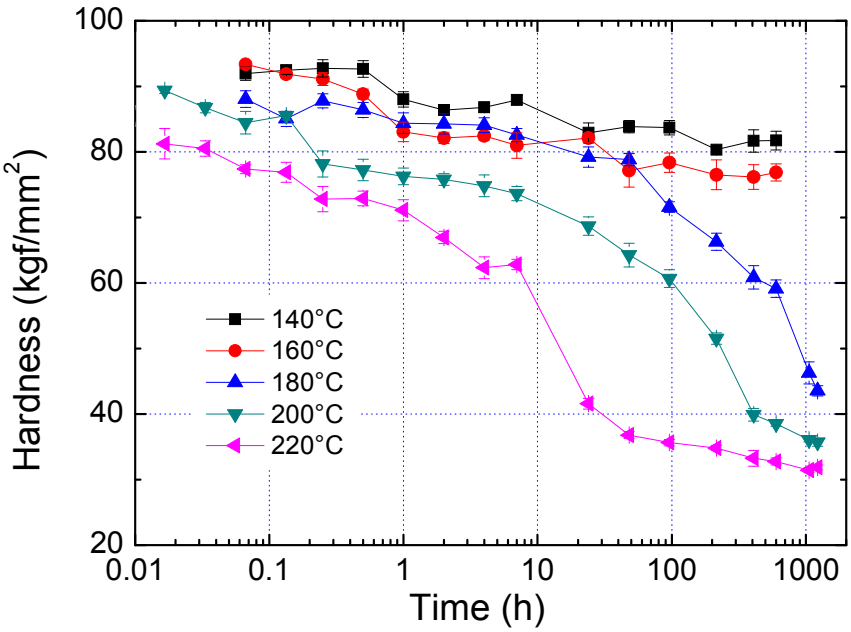

Figure 6.12: Hardness variation of AA1100 aluminium deformed by ARB for 6 cycles upon thermal annealing. Error bars show the standard deviations.

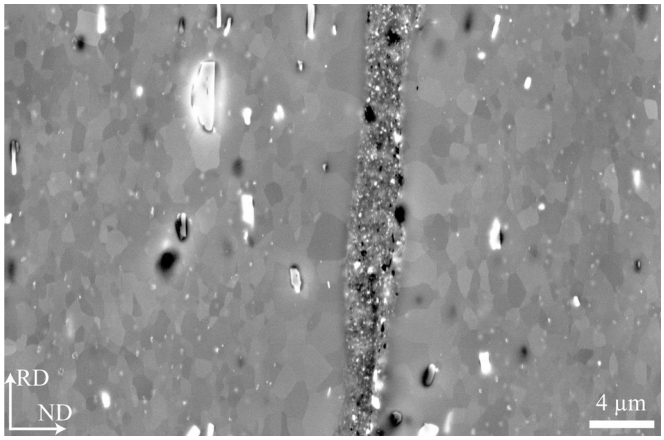

Figure 6.13: BSE image showing precipitation and a precipitation-free zone along the bonding layer in AA1100 aluminium deformed by ARB and annealed at 220°C for 7 hours.

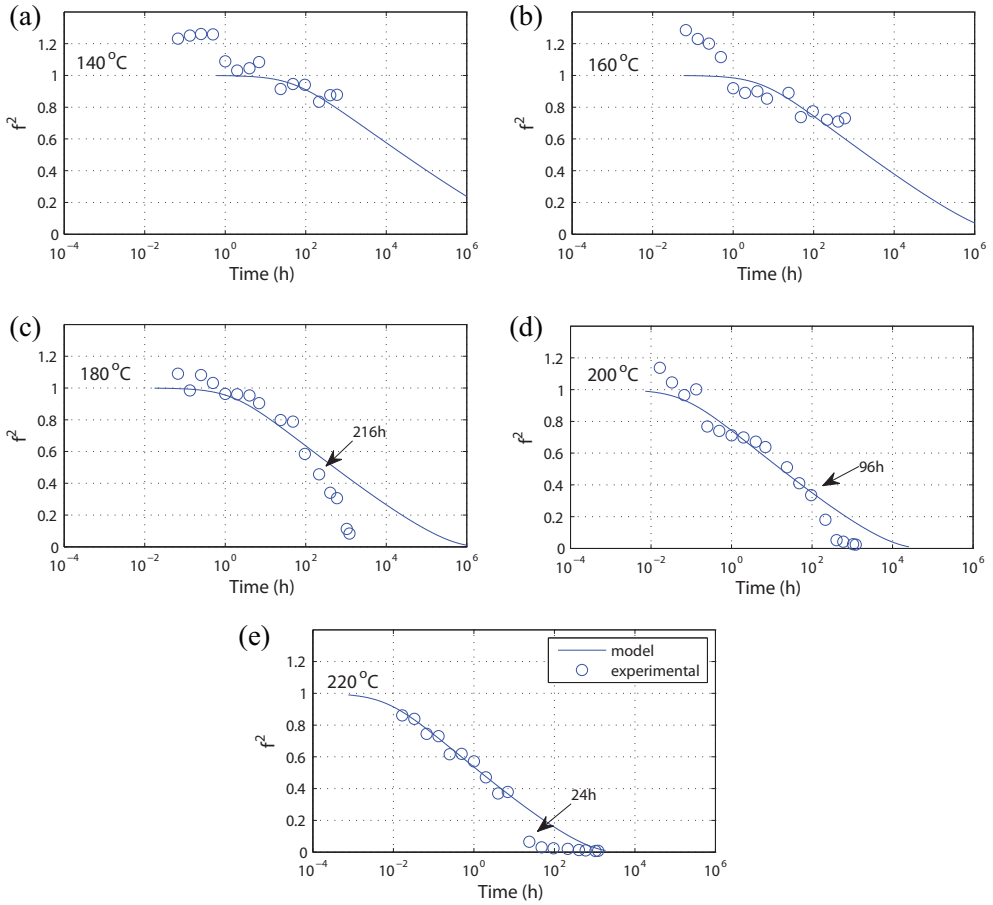

Figure 6.14: Isothermal kinetics of recovery of AA1100 aluminium deformed by ARB under the assumption of constant K_0 and β for all temperatures.

Microstructural investigations by EBSD showed that the deformed ARB samples were quite different from the cold rolled structure. Although the lamellar boundary spacing was similar (~0.23 μm), ARB samples were characterized by a weak texture instead of a strong rolling texture, and they contained a higher fraction of high angle boundaries, i.e. ~70% boundaries had misorientation angles above 15°. After annealing, the structure coarsened in a somewhat continuous manner due to the high fraction of high angle boundaries, and it also became more equiaxed. After annealing at 220, 200 and 180°C for 24, 96 and 216 hours, respectively, grains much larger than the average were observed, and therefore these and annealing for longer time intervals are not considered in the analysis of recovery kinetics. Taking the average value of $\beta P_0/R$ as 4.7×10^3 K from a preliminary fitting, one obtains the adjusted fitting as plotted in Figure 6.14. The corresponding activation

energy Q_0 estimated is 228±18 kJ/mol, slightly higher than that in the cold rolled AA1050 aluminium. The fitting in Figure 6.14 is less satisfactory than that for the strain 5.5 AA1050 aluminium (e.g. Figure 6.6), and the strong hardening effect may be responsible for the large deviation.

6.5 Discussion

6.5.1 Recovery model

The previous model (Vandermeer and Hansen 2008) to analyze recovery kinetics has been changed in the present study by determining the onset of recrystallization experimentally and excluding samples where recrystallization has taken place. Such an approach is more directly based on experiment as the hardness of recovered regions is measured instead of being calculated and no assumptions of the recrystallization kinetics, which is also complex (Doherty *et al.* 1986), are necessary. Moreover, in the present model before estimating the activation energy, the recovery mechanisms at a specific state (i.e. a specific value of f^2) are assumed to be independent of temperature, and thus the values of K_0 and β are fixed. Such an assumption and an adjusted fitting provide the possibility of estimating the activation energy, otherwise a linear fitting in a ($\ln t_0^{-1}$) vs $1/T$ plot is meaningless.

The key part of the recovery model is the rate equation adopted, i.e. Equation (2.4), which is a first-order reaction rate equation with its apparent activation energy depending on the extent of recovery. In a highly deformed structure, different recovery processes such as dislocation annihilation and reconfiguration (Friedel 1964), subgrain growth (Sandstrom 1977a,b), and triple junction motion may operate concurrently or consecutively, and therefore the overall recovery kinetics is complex. As pointed out by Bever (1957), different processes may have different kinetics, and therefore a single equation is at most an approximation. Furthermore, due to the presence of

different diffusion species (solutes and solvent) and different diffusion geometries (dislocation core, boundary, and lattice), the rate controlling mechanism is also complex even for a single recovery process. Therefore, care much be taken in the interpretation of the modelling results.

The apparent activation energy increases during recovery (see e.g. Michalak and Paxton 1961), and it was sometimes rationalized based on the heterogeneity of the deformation microstructure so that regions with higher stored energy recover easier. However, the stored energy is typically three orders of magnitude smaller than the activation energy, and thus the heterogeneity is not likely to affect the activation energy significantly. Instead, the increase of the apparent activation energy is more likely due to the variation in diffusion species and diffusion geometries. As recovery proceeds, the contribution of short circuit diffusion over lattice diffusion may decrease due to the decrease of dislocation density, triple junction density and boundary area per unit volume. Moreover, solute drag may become increasingly pronounced due to the increase in the ratio between solutes and boundaries. In the present model, the apparent activation energy is assumed to increase with the extent of recovery linearly as shown in Equation (6.4). Since several different recovery processes may operate during annealing and each process may involve several different atomistic mechanisms, the situation is extremely complex. However, as a first approximation, the linear assumption is not unreasonable since processes easy-to-activate will probably operate first especially at relatively low temperatures.

Different recovery processes may have different rate dependence. For example, for mutual annihilation of dislocations with opposite Burgers vectors, the reaction rate will be probably of second order (Li 1966; Sandstrom 1977a); whereas for subgrain growth, the reaction rate may be of third order in respect of the stored energy. Besides, each process will also probably have its own rate constants (Sandstrom 1977a,b). In the present model, a first-order reaction rate, together with a constant K_0, is assumed for the whole recovery range. Such an approximation is reasonable for the practical use. The reason is that the apparent activation energy has been

assumed to be variable, and hence the order of reaction rate becomes less important for the model. Due to the same reason, a zero-order assumption, i.e. Equation (2.3), is also found to be useful (Kuhlmann *et al.* 1949; Cottrell and Aytekin 1950) although it certainly cannot describe the very end stage.

6.5.2 Activation energy

As discussed above, the most important part of the present model is the assumption that the apparent activation energy increases as recovery proceeds, and this assumption is verified by the positive value of the experimental fitting parameter $\beta P_0/R$. To further examine this assumption, a standard estimation of the apparent activation energy over different extent of recovery (averaged value over certain range) for the thickness centre of strain 5.5 aluminium was carried out. By integrating Equation (2.2) and fixing the parameter P, one arrives at:

$$\ln t = c_4 + \frac{Q_0}{RT}, \tag{6.5}$$

where c_4 is a constant. Therefore the activation energy can be determined from a ($\ln t$) vs $1/T$ plot. The results are shown in Figure 6.15 using both f and f^2 for analyses. Both analyses showed that the apparent activation energy increases as recovery proceeds (f and f^2 decrease). Furthermore, the estimated range of activation energy agrees with the model results (131~186 kJ/mol) very well, giving more confidence on the present model.

The microstructure coarsens during recovery, and the coarsening inevitably involves the migration of medium and high angle boundaries (Ralph *et al.* 1994), i.e. diffusion of atoms across the boundary. In high purity aluminium, low activation energies (~70 kJ/mol) were found for this process (Haessner and Hofmann 1978; Haessner and Schmidt 1993). This activation energy is quite close to that measured for boundary diffusion (84 kJ/mol) (Frost and Ashby 1982). However in aluminium alloys, solutes segregate at boundaries, causing solute drag during boundary migration, i.e. solutes have to diffuse in the bulk following the migrating boundaries (Lucke and Detert

1957; Cahn 1962). Therefore lattice diffusion of solutes is usually found to be the rate controlling mechanism during subgrain growth and recrystallization (Furu *et al.* 1995; Huang and Humphreys 2000; Vandermeer and Juul Jensen 2001). In the present analysis, Q_0 = ~190 kJ/mol is also consistent with the diffusion of Fe in the bulk of aluminium (Du *et al.* 2003; Simonovic and Sluiter 2009) as in studies of similar aluminium (Furu *et al.* 1995; Vandermeer and Juul Jensen 2001).

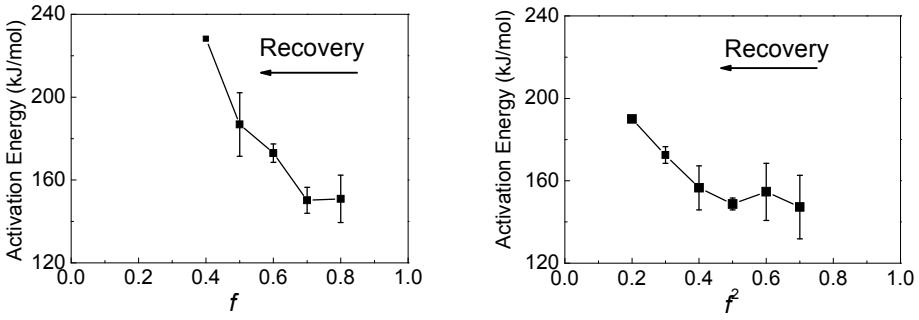

(a) (b)

Figure 6.15: Activation energy estimated from Equation (6.5) using (a) f and (b) f^2 for the recovery of AA1050 aluminium cold rolled to a strain of 5.5.

Triple junction motion is found to be an important recovery mechanism in a deformed lamellar structure. During migration of a triple junction in a lamellar structure, one boundary is left behind, in contrast to boundary migration, where nearly perfect crystals are left behind the migrating boundaries. The special geometry of triple junction motion in a finely-spaced lamellar structure may have a significant effect. Although the exact mechanism is unclear yet, the presence of three boundaries, instead of one, during triple junction motion is likely to lower the activation energy compared to boundary migration. The relatively low activation energy (~130 kJ/mol) found in the early part of recovery is also in agreement with this analysis.

A single recovery rate equation cannot include all the operating recovery processes, and consequently the estimated range of activation energy cannot account for all the underlying atomic mechanisms. The model results only

correspond to those major recovery processes and atomic mechanisms. Therefore it is not surprising that for the strain 5.5 aluminium the initial stage of recovery, which was analyzed in Chapter 5 and found to have a low activation energy (~80 kJ/mol), is missing in the current kinetic analysis since this initial stage is rather limited.

6.5.3 Microstructural coarsening

During recovery of a deformed metal, the microstructure coarsens and the hardness decreases. In the present model, the hardness is used to analyze the recovery kinetics. Alternatively, the boundary spacing, or the subgrain size, may be used for such an analysis. The evolution of the lamellar boundary spacing D, i.e. boundary spacing measured along the normal direction, during isothermal annealing at 200°C and 220°C is shown in Figure 6.16, together with the data for annealing at 300°C reported by Mishin *et al.* (2010). These boundary spacings were measured in the thickness centre before significant recrystallization took place. A standard analysis, using Equation (6.5), led to the results shown in Figure 6.17, in a good agreement with the analysis based on hardness data. The results also indicate that the same recovery mechanisms operate at higher temperatures, at least up to 300°C.

In a number of previous studies (e.g. Lian *et al.* 1995; Wang *et al.* 1996; Zahid *et al.* 2009), the microstructural coarsening in heavily deformed metals was analyzed in analogy to grain growth in a coarse material based on the following equation:

$$D^2 - D_0^2 = k_0 \exp(-\frac{Q_0}{RT})t\,, \tag{6.6}$$

where D is the boundary spacing (or subgrain size) after annealing, D_0 is the boundary spacing (or subgrain size) before annealing, and k_0 is the kinetic constant. However, very few experimental measurements followed this ideal growth behaviour (Humphreys and Hatherly 2004) and thus a more general form may be preferred (Huang and Humphreys 2000; Park *et al.* 2001):

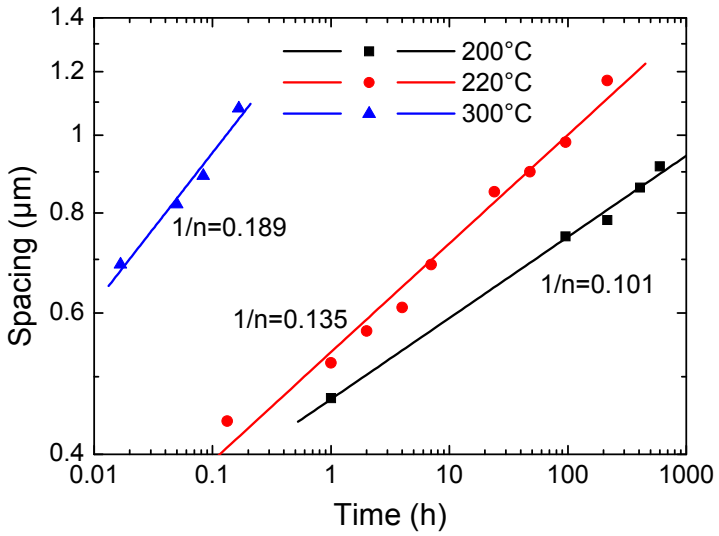

Figure 6.16: EBSD measurements of the lamellar boundary spacing during isothermal annealing of the AA1050 aluminium cold rolled to a strain of 5.5. Different slopes are indicated for different temperatures. Data for annealing at 300°C are from Mishin *et al.* (2010).

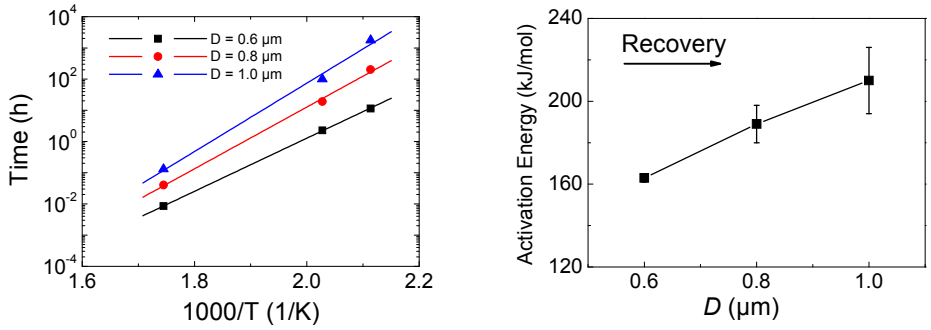

(a) (b)

Figure 6.17: (a) Temperature dependence and (b) variation of the activation energy during microstructural coarsening of the AA1050 aluminium cold rolled to a strain of 5.5.

$$D^n - D_0^n = k_0 \exp(-\frac{Q_0}{RT})t\,, \tag{6.7}$$

where n is the growth component. It can be seen in Figure 6.16 that the growth component increases (the slope in the log-log plot decreases) with decreasing isothermal annealing temperature, and it is much larger than 2 at

medium and low annealing temperatures (e.g. n=10 at 200°C), in agreement with the results found by Huang and Humphreys (2000).

A single growth component cannot describe the microstructural coarsening of a heavily deformed metal. It follows that although boundary spacings may be used to analyze the recovery kinetics, a single series of isochronal annealing (Figure 6.18) is insufficient to determine the microstructural coarsening in a heavily deformed material, where the size of subgrains is very fine and the apparent activation energy increases during annealing. As a test, the data in Figure 6.18 are analyzed based on Equations (6.6) and (6.7) taking n=10 as found at 200°C, disregarding different degrees of recovery took place at different temperatures during the isochronal annealing (i.e. disregarding different apparent activation energies at different temperatures). The results are shown in Figure 6.19, where good linear fittings can be obtained but the fittings are meaningless. Unfortunately, these artefacts were not recognized in a number of previous studies (e.g. Lian *et al.* 1995; Wang *et al.* 1995).

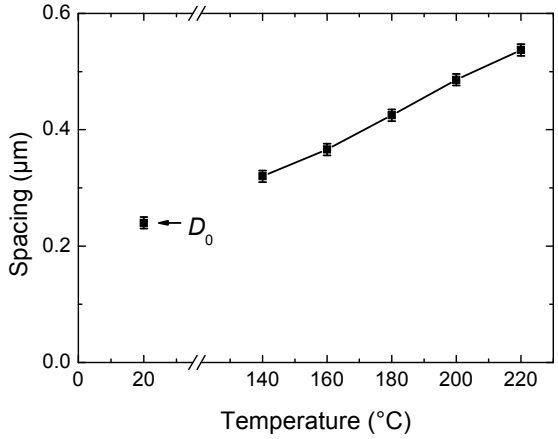

Figure 6.18: BSE measurements of the lamellar boundary spacing during isochronal annealing (1 h) of the AA1050 aluminium cold rolled to a strain of 5.5. The spacing before annealing, D_0, is also shown.

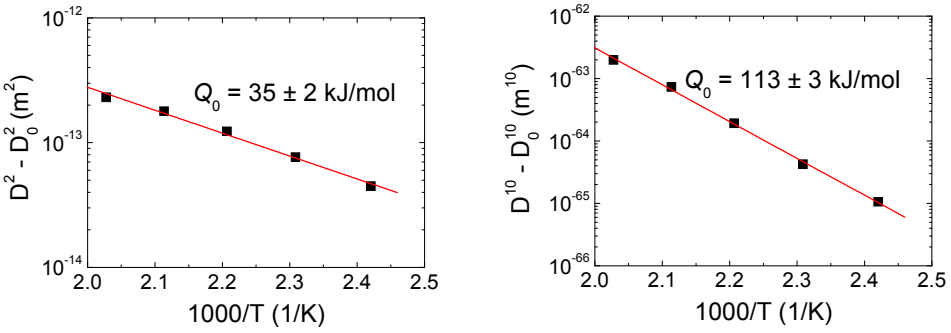

(a) (b)

Figure 6.19: A test of (a) Equation (6.6) and (b) Equation (6.7) in the case of n=10.

6.5.4 Effect of deformation structure

As the strain increases, the boundary spacing decreases and the fraction of high angle boundaries increases (Hughes and Hansen 2000; Liu *et al.* 2002). The high angle boundaries can act as sinks of dislocations (Sutton and Balluffi 1995), and therefore they may enhance the rate of dislocation annihilation during recovery. The high angle boundaries have high energies and high mobility (Humphreys and Hatherly 2004), and therefore they may enhance the microstructural coarsening during recovery. It was observed experimentally in aluminium alloy cold rolled to a true strain of 2 that bands containing boundaries of higher misorientation angles coarsened more rapidly than bands containing boundaries of lower misorientation angles (Xing *et al.* 2006). Such observations underpin the effect of high angle boundaries on the enhanced recovery rate at high strains. The finely-spaced high angle boundaries at high stains may also enhance the short circuit diffusion and reduce the apparent activation energy. However, this effect seems to be minor as indicated by the current results.

The different annealing behaviour between the thickness centre and the subsurface region in the strain 5.5 AA1050 aluminium can be also understood based on the fraction of high angle boundaries. It was found that a typical

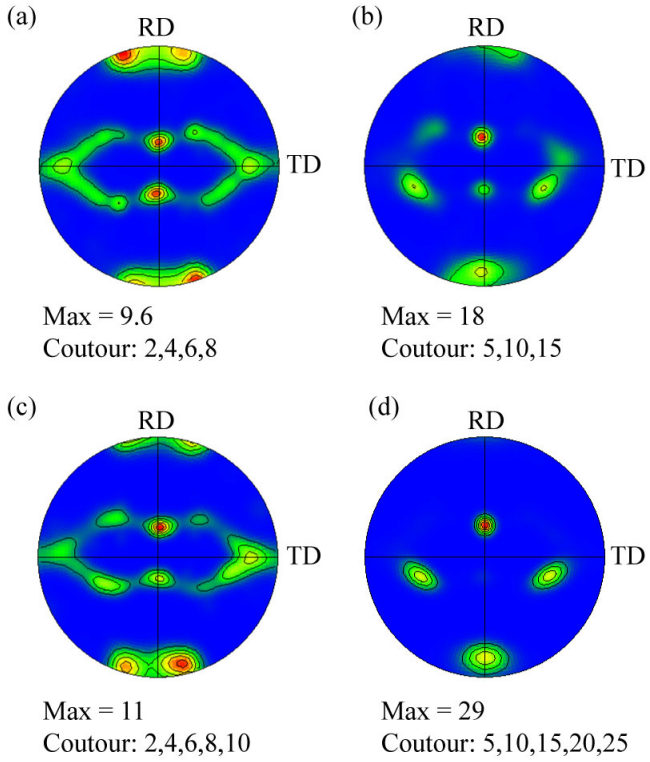

Figure 6.20: {111} pole figures for the AA1050 aluminium cold rolled to a true strain of 5.5 and annealed at 220°C for 216 hours. (a) Thickness centre of deformed state; (b) one side of subsurface of deformed state; (c) thickness centre of annealed state; and (d) one side of subsurface of annealed state.

rolling texture was dominant in the thickness centre whereas one variant of Copper texture was dominant in one side of the subsurface region (the other variant at the other side) in the deformed state (Figure 6.20a,b). During annealing before significant recrystallization, the texture in the thickness centre was largely maintained, whereas the strong Copper variant at each subsurface became even stronger (Figure 6.20c,d). As a consequence, the fraction of high angle boundaries in the thickness centre was unchanged during annealing, whereas the faction in the subsurface region decreased (Figure 6.21a). Such a decrease of the fraction of high angle boundaries in the subsurface region during annealing is probably responsible for the smaller lamellar boundary spacing measured at later stages of recovery (Figure 6.21b) and rarity of nucleation of recrystallization in the subsurface region compared to the thickness centre. Such an analysis is in general agreement with the recovery kinetics observed. As shown in Figure 6.5 for the thickness centre

and Figure 6.9 for the subsurface region, the recovery kinetics is quite similar and slightly faster kinetics is found in the thickness centre at high temperatures, where significant recovery has taken place, leading to a significant difference in the fraction of high angle boundaries between the thickness centre and the subsurface region.

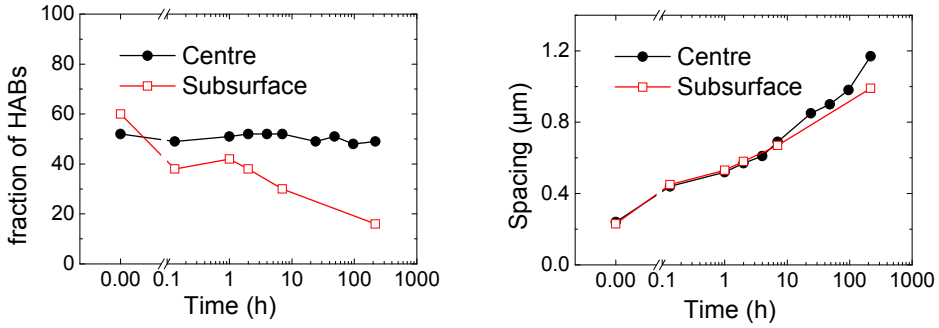

(a) (b)

Figure 6.21: (a) fraction of high angle boundaries (HABs) and (b) lamellar boundary spacing in the thickness centre and the subsurface region of the strain 5.5 aluminium during annealing at 220°C.

Due to a strong rolling texture, the development of high angle boundaries become less effective when rolled to high strains (Liu *et al.* 2002; Mishin *et al.* 2010). In contrast, deformation by ARB without lubrication leads to a relatively weak texture and a high fraction of high angle boundaries (~70%) as observed in the present study. Compared to the strain 5.5 cold rolled aluminium, the ARB samples have a similar lamellar boundary spacing but a higher fraction of high angle boundaries, although its thickness reduction only corresponds to a true strain of 4.2. It follows that the stored energy in the current ARB sample is higher than cold rolled aluminium despite its low nominal strain. Comparing Figure 6.14 with Figure 6.6, one can see that the recovery rate is similar in the two samples, one deformed by ARB for 6 cycles and the other cold rolled to a strain of 5.5. At relatively high temperatures (200°C and 220°C), where the effect of concurrent hardening may be reduced, a higher recovery rate can be observed in the ARB sample,

although its nominal strain is lower. The rapid recovery in the ARB sample is consistent with its high fraction of high angle boundaries, which have high energies and high mobility.

6.6 Summary

The recovery kinetics of cold rolled and ARB deformed commercial purity aluminium is examined in the temperature range 140~220°C, and the following conclusions can be drawn:

(1) A model is proposed, which is based on hardness measurements and incorporates microstructural observations. The model allows the correct estimation of the activation energy of recovery.

(2) The apparent activation energy increases during recovery of highly-strained metals, and it is ~190 kJ/mol at the end of recovery for commercial purity aluminium, pointing to an effect of solute drag during recovery as in recrystallization.

(3) Due to the increase of the apparent activation energy during recovery, it is demonstrated that the assumption of ideal grain growth behaviour is inappropriate for analyzing the structural coarsening (subgrain growth) of highly-strained metals.

(4) The recovery rate increases with increasing strain due to the increase of high angle boundaries as strain increases. Metals deformed by ARB recover more rapidly than those deformed by conventional rolling to similar strains since ARB introduces a higher fraction of high angle boundaries.

Chapter 7
Conclusions and outlook

The objective of this study is to explore and analyze the effect of heat treatments on the structure and properties of nanostructured metals processed by plastic deformation to high strains. These materials have characteristics such as a very fine microstructure, a high content of stored energy and a large strength. However, they are also characterized by a low thermal stability.

In this study, triple junctions in a deformed lamellar nanostructure are classified into three categories (Y-junctions, H-junctions, and r-junctions) based on the structural morphology, and a series of relationships is formulated between the density of triple junctions and the boundary spacing. Based on TEM and EBSD observations, thermally-activated Y-junction motion is identified as the key process during recovery of highly-strained aluminium, leading to removal of thin lamellae and coarsening of microstructure. A mechanism for recovery by Y-junction motion is proposed, which can underpin the general observation that a lamellar structure formed by plastic deformation coarsens into a more equiaxed structure during recovery annealing.

Y-junction motion operates in a wide temperature range, even at room temperature, in highly-strained aluminium. However, during annealing below 100°C, Y-junction motion is limited. At such low temperatures, annihilation of zigzagged dislocations is found to be the dominating recovery mechanism whereas other mechanisms, such as subgrain coalescence and boundary migration, are of minor importance. The recovery at low temperatures is

found to have a low activation energy, which may be associated with thermally-activated glide of jogged screw dislocations or pipe diffusion of solutes.

A model is proposed to analyze the recovery kinetics based on hardness measurements, and the model allows the activation energy of recovery to be estimated. During annealing of highly-strained commercial purity aluminium at 140°C and above, the apparent activation energy is found to increase as recovery proceeds, and it is ~190 kJ/mol at the end of recovery, pointing to an effect of solute drag during recovery as in recrystallization. Due to the increase of the apparent activation energy during recovery, it is demonstrated that the assumption of ideal grain growth behaviour is inappropriate for analyzing the structural coarsening (subgrain growth) of highly-strained metals.

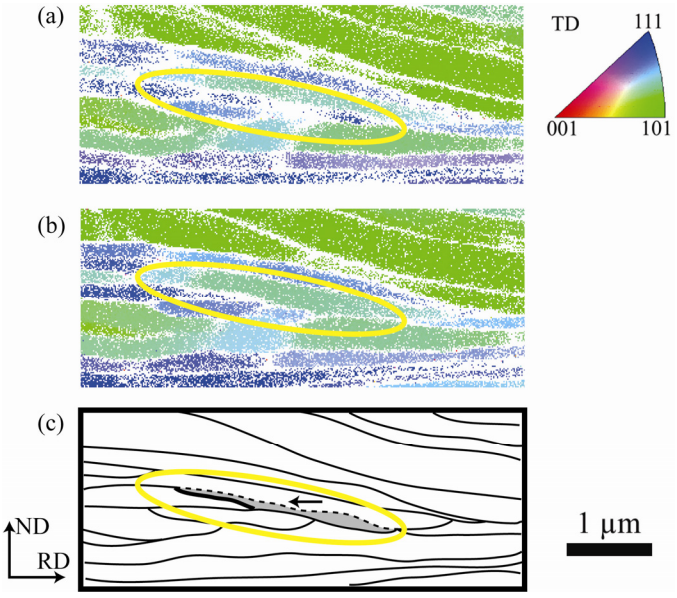

Figure 7.1: An example of Y-junction motion (in the marked area) in the longitudinal section (ND-RD plane) of aluminium during extra 5% deformation of heavily deformed AA1050 aluminium. (a) Orientation map of 99.6% cold-rolled aluminium. (b) Orientation map of the same area as in (a) after extra 5% cold rolling. The colours are coded according to the orientation of each pixel for both images. (c) Sketch of the Y-junction motion during extra 5% cold rolling, following the same markings as in Figure 4.7.

The study of Y-junction motion has been the central part of the work. This new recovery mechanism is found to be the key process during structural coarsening of highly-strained aluminium, and it will be interesting to see in the future whether this mechanism is universal and also operates in other metals deformed to high strains. The present study focuses on static recovery, and the Y-junction motion is found to be thermally activated. However, during dynamic recovery, the situation may change due to the external stress applied. Figure 7.1 shows the results of a preliminary study of the stress-driven Y-junction motion. A detailed study of Y-junction motion during plastic deformation will be of great importance since it may eventually answer the question of stage IV working hardening approaching saturation at very high strains.

Appendix

Recrystallization of AA1050 aluminium

The recrystallization behaviour of AA1050 aluminium of different strains was studied at relatively high temperatures. The hardness of annealed samples was measured in the rolling plane in the subsurface region, using a load of 200 g. For all samples after fully recrystallization, the hardness is close to 21 kgf/mm^2 irrespective of the annealing temperature and time (see Table A1). The microstructure of annealed samples was determined by EBSD in the longitudinal plane, and the equivalent circle diameter (ECD) after grain reconstruction in the commercial software Channel 5 was taken as the grain size. For the strains 2 and 4 aluminium, the microstructure is uniform through sample thickness, and the grain size increases with increasing annealing temperature and time. After prolonged annealing at 500°C, abnormal grain growth took place, leading to some huge grains (Table A1). For the strain 5.5 aluminium, there is a significant difference in the recrystallization behaviour between the thickness centre and the subsurface region when the annealing temperature is below 500°C, i.e. the grain size in the subsurface region is much larger than that in the thickness centre after recrystallization. This difference diminished when the annealing temperature was raised, leading to a relatively uniform microstructure through the sample thickness. If only the thickness centre is studied for the strain 5.5 aluminium, then the grain size increases with increasing annealing temperature, but almost independent of the annealing time and no abnormal grain growth is observed even at 600°C.

Table A1: Parameters of the AA1050 aluminium after recrystallization (ReX) and abnormal grain growth (AGG). When the microstructure is different between the thickness centre and the subsurface region, the grain size at the subsurface region is given in the parentheses.

Strain	Heat treatment	Uniformity	Grain size (μm)	Hardness (kgf/mm^2)
2	300°C 2h	86% ReX	18	23.5
2	500°C 2h	Init. of AGG	30	21.1
2	500°C 4h	AGG	>1000	21.0
2	300°C 2h+500°C 2h	√	33	21.0
4	300°C 2h	√	9	21.5
4	500°C 2h	√	28	21.3
4	500°C 4h	AGG	>1000	21.8
4	300°C 2h+500°C 2h	√	30	21.5
5.5	300°C 2h	×	13 (36)	21.6
5.5	400°C 2h	×	19 (32)	21.5
5.5	500°C 10min	√	21	/
5.5	500°C 2h	√	23	21.1
5.5	500°C 4h	√	23	20.9
5.5	600°C 2h	√	41	21.3
5.5	300°C 2h+500°C 2h	×	30 (45)	20.8

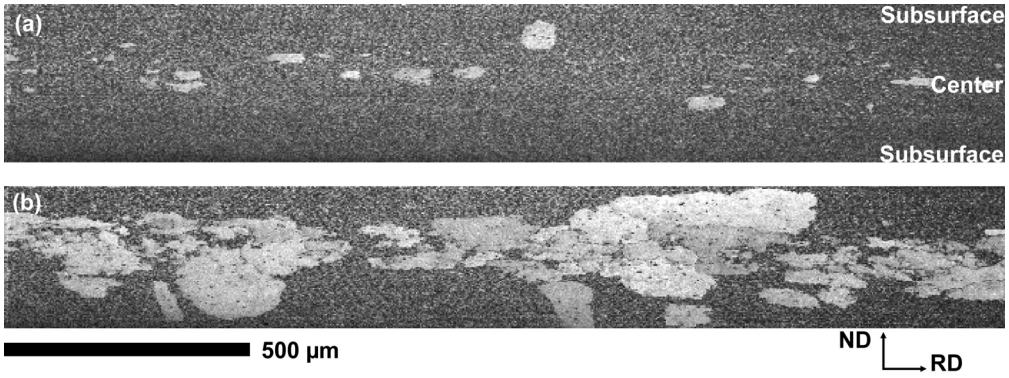

Figure A1: EBSD pattern quality map of the AA1050 aluminium cold rolled to a strain of 5.5 and subsequently annealed at 220°C for (a) 216 hours and (b) 408 hours. The recrystallized grains appear brighter than the recovered matrix.

The difference between the thickness centre and the subsurface region in the strain 5.5 aluminium is further magnified when the annealing temperature is lowered. It is shown in Figure A1 that during annealing of the strain 5.5 aluminium at 220°C, nuclei formed at the thickness centre and then some of these nuclei grew into the subsurface region. Such a nucleation and growth behaviour explains the different grain sizes found between the thickness centre and the subsurface region after fully recrystallization (Table A1).

References

Aina, S., Dupasquier, A., Folegati, P., De Diego, N., del Rio, J., Somoza, A. & Valli, M. 1997 Temperature dependence of positron trapping at grain boundaries. *J. Phys. – Condes. Matter* **9,** 6749-6759.

Baddeley, A. & Jensen, E. B. V. 2005 *Stereology for statisticians*. London, UK: Chapman and Hall/CRC.

Bay, B., Hansen, N., Hughes, D. A. & Kuhlmann-Wilsdorf, D. 1992 Evolution of fcc deformation structures in polyslip. *Acta Metall. Mater.* **40,** 205-219.

Beck, P. A. 1954 Annealing of cold worked metals. *Adv. Phys.* **3,** 245-324.

Beck, P. A. & Sperry, P. R. 1950 Strain induced grain boundary migration in high purity aluminum. *J. Appl. Phys.* **21,** 150-152.

Bever, M. 1957 On the thermodynamics and kinetics of recovery, In *Creep and Recovery* (ed. R. Maddin), pp. 14-51. Cleveland, OH: American Society for Metals.

Borelius, G., Berglund, S. & Sjoberg, S. 1952 Measurements on the evolution of heat during the recovery of cold-worked metals. *Arkiv for Fysik* **6,** 143-149.

Bowen, J. R. 2008 Strength and structure in commercial purity aluminium after large strain. *Mater. Sci. Eng. A.* **483-484,** 231-234.

Cahn, J. W. 1962 Impurity-drag effect in grain boundary motion. *Acta Metallurgica* **10,** 789-798.

Cao, W. Q., Godfrey, A., Hansen, N. & Liu, Q. 2009 Annealing behavior of nanostructured aluminum produced by cold rolling to ultrahigh strains. *Metall. Mater. Trans. A* **40,** 204-214.

Christiansen, G., Bowen, J. R. & Lindbo, J. 2002 Electrolytic preparation of metallic thin foils with large electron-transparent regions. *Mater. Charact.* **49,** 331-335.

Clarebrough, L., Hargreaves, M. & West, G. 1955 The release of energy during annealing of deformed metals. *Proc. R. Soc. Lond. A* **232,** 252-270.

Cotterill, R. M. J., Petersen, K., Trumpy, G. & Traff, J. 1972 Positron lifetimes and trapping probabilities observed separately for vacancies and dislocations in aluminum. *Journal of Physics F – Metal Physics* **2,** 459-467.

Cottrell, A. & Aytekin, V. 1950 The flow of zinc under constant stress. *Journal of the Institute of Metals* **77,** 389-422.

Czubayko, U., Sursaeva, V. G., Gottstein, G. & Shvindlerman, L. S. 1998 Influence of triple junctions on grain boundary motion. *Acta Mater.* **46,** 5863-5871.

Desorbo, W. & Turnbull, D. 1959 Kinetics of vacancy motion in high-purity aluminum. *Physical Review* **115,** 560-563.

Dillamore, I. L., Morris, P. L., Smith, C. J. E. & Hutchinson, W. B. 1972 Transition bands and recrystallization in metals. *Proc. R. Soc. A* **329,** 405-420.

Doherty, R. D. & Szpunar, J. 1984 Kinetics of sub-grain coalescence – a reconsideration of the theory. *Acta Metallurgica* **32,** 1789-1798.

Doherty, R. D., Rollett, A. D. & Srolovitz, D. 1986 Structural evolution during recrystallization. In *7th Risø Int. Symp. on Metallurgy and Materials Science* (eds N. Hansen *et al*.), pp. 53–67. Roskilde, Denmark: Risø National Laboratory.

Doherty, R. D., Hughes, D. A., Humphreys, F. J., Jonas, J. J., Juul Jensen, D., Kassner, M. E., King, W. E., McNelley, T. R., McQueen, H. J. & Rollett, A. D. 1997 Current issues in recrystallization: A review. *Mater. Sci. Eng. A* **238,** 219-274.

Driver, J. H. 1995. Effect of crystal orientation on recrystallization, In *16th Risø Int. Symp. on Materials Science* (eds N. Hansen *et al*.), pp. 25-36. Roskilde, Denmark: Risø National Laboratory.

Driver, J. H. 2004 Stability of nanostructured metals and alloys. *Scr. Mater.* **51,** 819-823.

Du, Y., Chang, Y., Huang, B., Gong, W., Jin, Z., Xu, H., Yuan, Z., Liu, Y., He, Y. & Xie, F. 2003 Diffusion coefficients of some solutes in fcc and liquid Al: critical evaluation and correlation. *Mater. Sci. Eng. A* **363,** 140-151.

Dupasquier, A., Kogel, G. & Somoza, A. 2004 Studies of light alloys by positron annihilation techniques. *Acta Mater.* **52,** 4707-4726.

Eldrup, M. & Singh, B. 1997 Studies of defects and defect agglomerates by positron annihilation spectroscopy. *J. Nucl. Mater.* **251,** 132-138.

Faivre, P. & Doherty, R. D. 1979 Nucleation of recrystallization in compressed aluminium: studies by electron microscopy and Kikuchi diffraction. *J. Mater. Sci.* **14,** 897-919.

Ferry, M. & Burhan, N. 2007 Structural and kinetic aspects of continuous grain coarsening in a fine-grained Al-0.3Sc alloy. *Acta Mater.* **55,** 3479-3491.

Fluss, M., Smedskjaer, L., Chason, M., Legnini, D. & Siegel, R. 1978 Measurements of vacancy formation enthalpy in aluminum using positron-annihilation spectroscopy. *Phys. Rev. B* **17,** 3444-3455.

Friedel, J. 1964 *Dislocations.* Oxford, UK: Pergamon.

Frost, H. & Ashby, M. 1982 *Deformation-mechanism maps.* New York, NY: Pergamon.

Furu, T., Orsund, R. & Nes, E. 1995 Subgrain growth in heavily deformed aluminium – experimental investigation and modeling treatment. *Acta Metall. Mater.* **43,** 2209-2232.

Galina, A. V., Fradkov, V. Y. & Schvindlerman, L. S. 1987 Influence of grain ternary joint mobility on boundary migration. *Fiz. Metallov Metalloved.* **63,** 1220-1222.

Gleiter, H. 1969 Migration of small angle boundaries. *Phil. Mag.* **20,** 821-830.

Godfrey, A. & Hughes, D. A. 2000 Scaling of the spacing of deformation induced dislocation boundaries. *Acta Mater.* **48,** 1897-1905.

Godfrey, A. & Liu, Q. 2009 Stored energy and structure in top-down processed nanostructured metals. *Scr. Mater.* **60,** 1050-1055.

Gottstein, G., Shvindlerman, L. S. & Zhao, B. 2010 Thermodynamics and kinetics of grain boundary triple junctions in metals: Recent developments. *Scr. Mater.* **62,** 914-917.

Haessner, F. & Hofmann, S. 1978 Migration of high angle grain boundaries. In *Recrystallization of Metallic Materials* (ed. F. Haessner), pp. 63-95. Stuttgart, Germany: Dr. Riederer-Verlag GmbH.

Haessner, F. & Schmidt, J. 1993 Investigation of the recrystallization of low-temperature deformed highly pure types of aluminum. *Acta Metall. Mater.* **41,** 1739-1749.

Hansen, N. 2001 New discoveries in deformed metals. *Metall. Mater. Trans. A* **32,** 2917-2935.

Hansen, N. 2004 Preface to the viewpoint set: 'metals and alloys with a structural scale from the micrometre to the atomic dimensions'. *Scr. Mater.* **51,** 751-753.

Hansen, N., Huang, X., Moller, M. G. & Godfrey, A. 2008 Thermal stability of aluminum cold rolled to large strain. *J. Mater. Sci.* **43,** 6254-6259.

Herring, C. 1951 Surface tension as a motivation for sintering. In *The physics of powder metallurgy* (ed. W. E. Kingston), pp. 143–179. New York, NY: Mcgraw-Hill.

Hirsch, P., Howie, A., Nicholson, R., Pashley, D. W. & Whelan, M. J. 1977 *Electron microscopy of thin crystals.* 2nd edn. Malabar, FL: Krieger.

Hu, H. 1962 Direct observations on annealing of a Si-Fe crystal in electron microscope. *Transactions of the Metallurgical Society of AIME* **224,** 75-83.

Huang, X. 2009 Preface to the viewpoint set: Nanostructured metals – advances in processing, characterization and application. *Scr. Mater.* **60,** 1031-1032.

Huang, X., Hansen, N. & Tsuji, N. 2006a Hardening by annealing and softening by deformation in nanostructured metals. *Science* **312,** 249-251.

Huang, X., Xing, Q., Juul Jensen, D. & Hansen, N. 2006b Large strain deformation and annealing of aluminium. *Materials Science Forum* **519-521,** 79-84.

Huang, Y. & Humphreys, F. J. 2000 Subgrain growth and low angle boundary mobility in aluminium crystals of orientation {110}{001}. *Acta Mater.* **48,** 2017-2030.

Hughes, D. A. & Hansen, N. 2000 Microstructure and strength of nickel at large strains. *Acta Mater.* **48,** 2985-3004.

Humphreys, F. J. 1997a A unified theory of recovery, recrystallization and grain growth, based on the stability and growth of cellular microstructures – I. the basic model. *Acta Mater.* **45,** 4231-4240.

Humphreys, F. J. 1997b A unified theory of recovery, recrystallization and grain growth, based on the stability and growth of cellular microstructures – II. the effect of second-phase particles. *Acta Mater.* **45,** 5031-5039.

Humphreys, F. J. 2001 Review – grain and subgrain characterisation by electron backscatter diffraction. *J. Mater. Sci.* **36,** 3833-3854.

Humphreys, F. J. 2004 Characterisation of fine-scale microstructures by electron backscatter diffraction (EBSD). *Scr. Mater.* **51,** 771-776.

Humphreys, F. J. & Hatherly, M. 2004. *Recrystallization and related annealing phenomena.* 2nd edn. Oxford, UK: Pergamon.

Humphreys, F. J., Prangnell, P. B., Bowen, J. R., Gholinia, A. & Harris, C. 1999 Developing stable fine-grain microstructures by large strain deformation. *Philos. Trans. R. Soc. Lond. Ser. A* **357,** 1663-1680.

Ivanov, V. A., Molodov, D. A., Shvindlerman, L. S. & Gottstein, G. 2004 Effect of "surface" triple junction on curved boundary motion in Al-bicrystals. *Acta Mater.* **52,** 969-975.

Jackman, J., Hood, G. & Schultz, R. 1987 Positron lifetime measurements of the vacancy properties of annealed and electron-irradiated aluminum. *Journal of Physics F – Metal Physics* **17,** 1817-1831.

Jazaeri, H. & Humphreys, F. J. 2004 The transition from discontinuous to continuous recrystallization in some aluminium alloys II – annealing behaviour. *Acta Mater.* **52,** 3251-3262.

Jazaeri, H., Humphreys, F. J. & Bate, P. S. 2006 Static and dynamic grain growth in single-phase aluminium. *Materials Science Forum* **519-521,** 153-160.

Jones, A. R., Ralph, B. & Hansen, N. 1979 Subgrain coalescence and the nucleation of recrystallization at grain-boundaries in aluminum. *Proc. R. Soc. A* **368,** 345-357.

King, A. H. 2010 Triple lines in materials science and engineering. *Scr. Mater.* **62,** 889-893.

Knudsen T. 2006 *Risø-I-2143(EN) GFF basic material AA1050*. Roskilde, Denmark: Risø National laboratory.

Knudsen, T., Cao, W. Q., Godfrey, A., Liu, Q. & Hansen, N. 2008 Stored energy in nickel cold rolled to large strains, measured by calorimetry and evaluated from the microstructure. *Metall. Mater. Trans. A* **39,** 430-440.

Kuhlmann, D. 1948 Zur theorie der nachwirkungserscheinungen. *Zeitschrift Fur Physik* **124,** 468-481.

Kuhlmann, D., Masing, G. & Raffelsieper, J. 1949 Zur theorie der erholung. *Z. Metallk.* **40,** 241-246.

Kuhlmann-Wilsdorf, D. 1989 Theory of plastic deformation: – properties of low energy dislocation structures. *Mater. Sci. Eng. A* **113,** 1-41.

Kuhlmann-Wilsdorf, D. & Hansen, N. 1991 Geometrically necessary, incidental and subgrain boundaries. *Scr. Metall. Mater.* **25,** 1557-1562.

Li, J. C. M. 1962 Possibility of subgrain rotation during recrystallization. *J. Appl. Phys.* **33,** 2958-2965.

Lian, J., Valiev, R. & Baudelet, B. 1995 On the enhanced grain-growth in ultrafine grained metals. *Acta Metall. Mater.* **43,** 4165-4170.

Liu, Q. 1994 A simple method for determining orientation and misorientation of the cubic crystal specimen. *J. Appl. Crystallogr.* **27,** 755-761.

Liu, Q. 1995 A simple and rapid method for determining orientations and misorientations of crystalline specimens in TEM. *Ultramicroscopy* **60,** 81-89.

Liu, Q., Juul Jensen, D. & Hansen, N. 1998 Effect of grain orientation on deformation structure in cold-rolled polycrystalline aluminium. *Acta Mater.* **46,** 5819-5838.

Liu, Q., Huang, X., Lloyd, D. J. & Hansen, N. 2002 Microstructure and strength of commercial purity aluminium (AA 1200) cold-rolled to large strains. *Acta Mater.* **50,** 3789-3802.

Lu, K. 2010 The future of metals. *Science* **328,** 319-320.

Lucke, K. & Detert, K. 1957 A quantitative theory of grain-boundary motion and recrystallization in metals in the presence of impurities. *Acta Metallurgica* **5,** 628-637.

Lucke, K. & Stuwe, H. 1971 Theory of impurity controlled grain boundary motion. *Acta Metallurgica* **19,** 1087-1099.

Lytton, J., Westmacott, K. H. & Potter, L. 1965 Relation between flow stress and dislocation structure during recovery of high-purity aluminum. *Transactions of the Metallurgical Society of AIME* **233,** 1757-1765.

Martin, J. W. & Doherty, R. D. 1976 *Stability of microstructure in metallic systems.* Cambridge, UK: Cambridge University Press.

Michalak, J. T. & Paxton, H. W. 1961 Some recovery characteristics of zone-melted iron. *Transactions of the Metallurgical Society of AIME* **221,** 850-857.

Mishin, O. V. & Godfrey, A. 2008 Microstructure of ECAE-processed copper after long-term room-temperature storage. *Metall. Mater. Trans. A* **39,** 2923-2930.

Mishin, O. V., Juul Jensen, D. & Hansen, N. 2010 Evolution of microstructure and texture during annealing of aluminum AA1050 cold rolled to high and ultrahigh strains. *Metall. Mater. Trans. A* **41,** 2936-2948.

Mullins, W. W. 1956 2-dimensional motion of idealized grain boundaries. *J. Appl. Phys.* **27,** 900-904.

Murr, L. E. 1975 *Interfacial phenomena in metals and alloys*. Reading, MA: Addison-Wesley.

Nes, E. 1995 Recovery revisited. *Acta Metall. Mater.* **43,** 2189-2207.

Olsen, J. V., Kirkegaard, P., Pedersen, N. J. & Eldrup, M. 2007 PALSfit: A new program for the evaluation of positron lifetime spectra. *Physica Status Solidi C* **4,** 4004-4006.

Oscarsson, A., Ekstrom, H. E. & Hutchinson, W. B., 1993 Transition from discontinuous to continuous recrystallization in strip-cast aluminium alloys, *Materials Science Forum,* **113-115**, 177-182.

Park, K., Kwon, H. & Shin, D. 2001 Apparent grain growth behavior of submicrometer grained Al-3 pct Mg during static annealing after fabrication by severe plastic straining. *Metall. Mater. Trans. A* **32,** 2670-2672.

Perryman, E. 1957 Recovery of Mechanical Properties. In *Creep and Recovery* (ed. R. Maddin), pp. 111-145. Cleveland, OH: American Society for Metals.

Prangnell, P. B., Hayes, J. S., Bowen, J. R., Apps, P. J. & Bate, P. S. 2004 Continuous recrystallisation of lamellar deformation structures produced by severe deformation. *Acta Mater.* **52,** 3193-3206.

Prinz, F., Argon, A. & Moffatt, W. 1982 Recovery of dislocation structures in plastically deformed copper and nickel single crystals. *Acta Metallurgica* **30,** 821-830.

Protasova, S. G., Gottstein, G., Molodov, D. A., Sursaeva, V. G. & Shvindlerman, L. S. 2001 Triple junction motion in aluminum tricrystals. *Acta Mater.* **49,** 2519-2525.

Ralph, B. 1990 Grain growth. *Materials Science and Technology* **6,** 1136-1144.

Ralph, B., Kurzydłowski, K. & Chojnacka, A. 1994 Studies of the changes in the geometry of grain boundaries and grains during recovery/continuous recrystallization in α-Fe. *J. Mater. Sci.* **29,** 3964-3968.

Randle, V., Hansen, N. & Juul Jensen, D. 1996 The deformation behaviour of grain boundary regions in polycrystalline aluminium. *Philos. Mag. A* **73,** 265-282.

Read, W. T. & Shockley, W. 1950 Dislocation models of crystal grain boundaries. *Physical Review* **78,** 275-289.

Sandstrom, R. 1977a Recovery of dislocations in subgrains and subgrain coalescence. *Acta Metallurgica* **25,** 897-904.

Sandstrom, R. 1977b Subgrain growth occurring by boundary migration. *Acta Metallurgica* **25,** 905-911.

Sandstrom, R., Lehtinen, B., Hedman, E., Groza, I. & Karlsson, S. 1978 Subgrain growth in Al and Al-1% Mn during annealing. *J. Mater. Sci.* **13,** 1229-1242.

Schmidt, J. & Haessner, F. 1990 Stage III-recovery of cold worked high-purity aluminum determined with a low-temperature calorimeter. *Z. Phys. B* **81,** 215-222.

Shekhar, S. & King, A. H. 2008 Strain fields and energies of grain boundary triple junctions. *Acta Mater.* **56,** 5728-5736.

Simonovic, D. & Sluiter, M. H. F. 2009 Impurity diffusion activation energies in Al from first principles. *Phys. Rev. B* **79,** 054304.

Smith C. J. E. & Dillamore I. L. 1970 Subgrain growth in high-purity iron. *Metal Science* **4,** 161-167.

Sutton, A. P. & Balluffi, R. W. 1995 *Interfaces in crystalline materials*. Oxford, UK: Clarendon Press.

Tsuji, N., Toyoda, T., Minamino, Y., Koizumi, Y., Yamane, T., Komatsu, M. & Kiritani, M. 2003 Microstructural change of ultrafine-grained aluminum during high-speed plastic deformation. *Mater. Sci. Eng. A* **350,** 108-116.

Ungar, T., Schafler, E., Hanak, P., Bernstorff, S. & Zehetbauer, M. 2007 Vacancy production during plastic deformation in copper determined by in situ X-ray diffraction. *Mater. Sci. Eng. A* **462,** 398-401.

Valiev, R. Z. & Langdon, T. G. 2006 Principles of equal-channel angular pressing as a processing tool for grain refinement. *Prog. Mater. Sci.* **51,** 881-981.

Vandermeer, R. A. & Hansen, N. 2008 Recovery kinetics of nanostructured aluminum: Model and experiment. *Acta Mater.* **56,** 5719-5727.

Vandermeer, R. A. & Juul Jensen, D. 2001 Microstructural path and temperature dependence of recrystallization in commercial aluminum. *Acta Mater.* **49,** 2083-2094.

Vandermeer, R. A. & Rath, B. 1990 Interface migration during recrystallization – the role of recovery and stored energy gradients. *Metallurgical Transactions A* **21,** 1143-1149.

von Neumann, J. 1952 Discussion remark concerning paper of C. S. Smith "grain shapes and other metallurgical applications of topology". In *Metal interfaces* (ed. C. Herring), pp. 108-110. Cleveland, OH: American Society for Metals.

Wang, J., Iwahashi, Y., Horita, Z., Furukawa, M., Nemoto, M., Valiev, R. & Langdon, T. 1996 An investigation of microstructural stability in an Al-Mg alloy with submicrometer grain size. *Acta Mater.* **44,** 2973-2982.

Wilkinson, A. & Hirsch, P. 1997 Electron diffraction based techniques in scanning electron microscopy of bulk materials. *Micron* **28,** 279-308.

Williams, D. B. & Carter, C. B. 2009 *The Transmission Electron Microscopy.* 3rd edn. New York, NY: Springer.

Xing, Q., Huang, X. & Hansen, N. 2006 Recovery of heavily cold-rolled aluminum: Effect of local texture. *Metall. Mater. Trans. A* **37,** 1311-1322.

Zahid, G. H., Huang, Y. & Prangnell, P. B. 2009 Microstructure and texture evolution during annealing a cryogenic-SPD processed Al-alloy with a nanoscale lamellar HAGB grain structure. *Acta Mater.* **57,** 3509-3521.

Zhang, H. W., Huang, X. & Hansen, N. 2008 Evolution of microstructural parameters and flow stresses toward limits in nickel deformed to ultra-high strains. *Acta Mater.* **56,** 5451-5465.

Zhao, B., Verhasselt, J. C., Shvindlerman, L. S. & Gottstein, G. 2010 Measurement of grain boundary triple line energy in copper. *Acta Mater.* **58,** 5646-5653.

Risø DTU is the National Laboratory for Sustainable Energy. Our research focuses on development of energy technologies and systems with minimal effect on climate, and contributes to innovation, education and policy. Risø has large experimental facilities and interdisciplinary research environments, and includes the national centre for nuclear technologies.

Risø DTU
National Laboratory for Sustainable Energy
Technical University of Denmark

Frederiksborgvej 399
PO Box 49
DK-4000 Roskilde
Denmark
Phone +45 4677 4677
Fax +45 4677 5688

www.risoe.dtu.dk